Fidelity Benchmarking of Industrial Silicon/Silicon-Germanium Qubits

Zur Erlangung des akademischen Grades eines

Doktors der Naturwissenschaften (Dr. rer. nat.)

von der KIT-Fakultät für Physik des
Karlsruher Instituts für Technologie (KIT)

genehmigte
Dissertation

von

M. Sc. Thomas Koch

Tag der mündlichen Prüfung: 13. Dezember 2024
1. Referent: Prof. Dr. Wolfgang Wernsdorfer
2. Referent: Prof. Dr. Kristiaan De Greve

Abstract

The realisation of a universal quantum computer will require the operation of thousands to millions of qubits. The possibility of using existing industrial semiconductor fabrication techniques and infrastructure for upscaling and reproducibility makes silicon based spin qubits one of the most promising platforms to achieve this goal. The implementation of the up to now largest semiconductor-based quantum processor was realised in a silicon/silicon-germanium (Si/SiGe) heterostructure known for its low charge noise, long qubit coherence times and fast driving speeds, but the high structural complexity creates challenges for industrial implementations.

In this work, a cryogenic setup was optimised for the characterisation of semiconductor-based spin qubits. In collaboration with the Interuniversity Microelectronics Centre (imec), the cryogenic setup was then used to demonstrate the operation of electric dipole spin resonance (EDSR) qubits, hosted in a natural Si/SiGe heterostructure, fully fabricated by an industrial CMOS 300 mm wafer process line, from heterostructure growth to the cobalt micromagnet monolithic integration. Measurements of charge noise affecting the formed qubit quantum dots, yield values below $2\,\mu\text{eV}/\sqrt{\text{Hz}}$ and a measured valley splitting energy of (87.9 ± 0.5) μeV allows for a wide frequency window for spin qubit operation.

Coherent spin manipulations result in Rabi frequencies up to 5 MHz at qubit resonance frequencies of 18.5 GHz. At this qubit working point, spin relaxation times of over 1 s and spin coherence times T_2^* and T_2^H of 1 μs and 50 μs are achieved respectively, for a natural silicon quantum well. Qubit lifetimes were measured for four different samples, coming from two different wafers and yield consistent results. Single qubit gate fidelities were extracted by randomised benchmarking experiments and result in a single qubit gate fidelity of 99.2 %, above the surface code error correction threshold. These results demonstrate the successful operation of state-of-the-art Si/SiGe spin qubit devices fabricated using advanced industrial 300 mm wafer process technologies.

Zusammenfassung

Die Realisierung eines universellen Quantencomputers wird den Betrieb von Tausenden bis Millionen von Qubits erfordern. Die Möglichkeit, vorhandene industrielle Halbleiterfertigungstechniken und -infrastrukturen für Skalierbarkeit und Reproduzierbarkeit zu nutzen, macht siliziumbasierte Spin-Qubits zu einer der vielversprechendsten Plattformen, um dieses Ziel zu erreichen. Die Implementierung des bisher größten halbleiterbasierten Quantenprozessors wurde in einer Silizium/Silizium-Germanium (Si/SiGe) Heterostruktur realisiert, die für ihr geringes Ladungsrauschen, lange Kohärenzzeiten der Qubits und hohe Ansteuerungsgeschwindigkeiten bekannt ist. Die hohe strukturelle Komplexität stellt jedoch Herausforderungen für industrielle Implementierung dar.

In dieser Arbeit wurde ein kryogener Versuchsaufbau zur Charakterisierung von halbleiterbasierten Spin-Qubits optimiert. In Zusammenarbeit mit dem Interuniversity Microelectronics Centre (imec) wurde der kryogene Versuchsaufbau anschließend verwendet, um den Betrieb von Elektrischen Dipol Spin Resonanz (EDSR) Qubits zu demonstrieren, die in einer natürlichen Si/SiGe-Heterostruktur integriert sind und vollständig in einem industriellen CMOS-300 mm-Waferprozess gefertigt wurden, von der Heterostruktur-Wachstumsphase bis zur monolithischen Integration des Kobalt Mikromagneten. Messungen des Ladungsrauschens, das die gebildeten Quantenpunkte der Qubits beeinflusst, ergaben Werte unter $2\,\mu eV/\sqrt{Hz}$, und eine gemessene Valley-Aufspaltung von $(87.9 \pm 0.5)\,\mu eV$ ermöglicht ein breites Frequenzfenster für den Betrieb von Spin-Qubits.

Kohärente Spin-Manipulationen führen zu Rabi-Frequenzen von bis zu 5 MHz bei Qubit-Resonanzfrequenzen von 18.5 GHz. An diesem Qubit-Betriebspunkt werden Spin-Relaxationszeiten von über 1 s und Spin-Kohärenzzeiten T_2^* und T_2^H von jeweils 1 µs und 50 µs erreicht, für einen Quantentopf in natürlichem Silizium. Die Lebensdauern der Qubits wurden für vier verschiedene Proben, die von zwei unterschiedlichen Wafern stammen, gemessen und

zeigen konsistente Ergebnisse. Die Ein-Qubit-Gatter-Fidelität wurde durch Randomisierte Benchmarking-Experimente extrahiert und ergibt eine Ein-Qubit-Gatter-Fidelität von 99.2 %, oberhalb der Fehlerschwelle des Surface Codes. Diese Ergebnisse demonstrieren den erfolgreichen Betrieb modernster Si/SiGe-Spin-Qubit-Bauelemente, die mit fortschrittlicher industrieller 300 mm-Wafer-Prozesstechnologie hergestellt wurden.

Contents

List of Figures

List of Tables

1. Introduction

The power of a quantum bit, or "qubit", compared to a classical bit can be clearly seen when performing a calculation $f(x)$. A classical computer must compute $f(0)$ and $f(1)$ sequentially, whereas the superposition of the quantum state allows simultaneous evaluation [1]:

$$f(|\psi\rangle) = \alpha f(|0\rangle) + \beta f(|1\rangle). \tag{1.1}$$

The computing power of a quantum computer can be increased significantly by increasing the number of qubits. In general, N qubits can compute on 2^N states simultaneously. This means that while a classical computer needs to double the number of classical bits to double its computing power, a quantum computer doubles its computing power by adding a single qubit. This gives an exponential speedup, and it is commonly said that a quantum computer with only 50 qubits can theoretically perform calculations that are intractable by the most powerful classical computers available today [2]. This is known as quantum advantage.

However, the exact speedup will depend on the class of the problem and the efficiency of the quantum algorithms, and a universally practical quantum computer will require thousands to millions of interconnected qubits [3–7], presenting an immense, long-term challenge for the quantum computing community to overcome.

The concept of quantum computing was introduced at the first Conference on the Physics of Computation, held at the Massachusetts Institute of Technology (MIT) in 1981, where the physicist Paul Benioff discussed the potential implementation of a quantum mechanical Turing machine [8] and Richard Feynman talked about the need for a computer based on quantum mechanical principles to effectively simulate natural phenomena [9].

Since then, quantum information processing has become an exciting new field within information technology with the potential to transform numerous

industries and scientific fields [10–13]. In particular, the development of universal quantum computing holds the promise of exponentially accelerating certain algorithms compared to classical computing techniques [14–16], with the claim of solving certain mathematical problems with already existing quantum hardware even faster than with the most powerful classical computers [17–19].

1.1. DiVincenzo criteria

The development of a practical and functional quantum computer requires a complex orchestration of physical, computational and engineering considerations, postulated by the DiVincenzo criteria. Any possible qubit system must meet these requirements proposed by David DiVincenzo in 2000 [20]:

1. "A scalable physical system with well characterised qubits":

   A well-characterised qubit requires precise knowledge of its physical properties, including its internal Hamiltonian, interactions with other states and qubits, and coupling with external fields used to manipulate its state. To achieve relevant quantum computational power, the system must also be scalable, which sounds simple but is ultimately the biggest challenge on the road to a universal quantum computer.

2. "The ability to initialise the state of the qubits to a simple fiducial state":

   The primary reason for initialising a qubit in a specific state is the computational requirement that registers must be set to a known value before the calculation begins. In addition, high initialisation fidelity is required, as initialisation affects everything from algorithm execution and error correction to system scalability and overall computational fidelity.

3. "Long relevant decoherence times, much longer than the gate operation time":

   Decoherence time is the period over which a quantum state loses its phase information due to interaction with its environment, leading the state to transform into a mixture of classical states. This process is crucial in understanding the transition from quantum to classical

behaviour and poses a significant challenge for quantum computing, as it can degrade the quantum information. Further, the manipulation speed of the qubit determines the time needed to execute qubit gates. An increased manipulation speed increases the computational speed, but should not reduce the coherence and lifetime of the qubit itself.

4. "A universal set of quantum gates":

   A quantum computer must be able to execute a universal set of quantum gates, allowing it to perform any arbitrary quantum operation. A universal gate set typically includes single-qubit rotations and one of the two-qubit gates XOR or CNOT. High fidelity in implementing these gates is essential for executing complex algorithms and error correction. The overall "clock time" of a quantum computer depends on the duration of these quantum gates and the need to prevent overlap between consecutive operations.

5. "A qubit-specific measurement capability"

   The result of the calculation must be read out, which requires the ability to measure the state of individual qubits, ideally without changing the state of the rest of the quantum computer. If the measurement of a qubit does not change its state, this is referred to as a "non-demolition" readout. While quantum computers can operate without non-demolition readout, quantum non-demolition measurements are particularly crucial for implementing quantum error correction . Further, while a high readout efficiency is desirable, a low efficiency can be compensated for by additional repetitions of the calculation.

In theory, any quantum mechanical system that meets these five criteria could be used for quantum computation, and over the years, several different physical implementations were demonstrated involving superconducting qubits [21–23], neutral atoms [24–26], trapped ions [27–29], color centres in diamond [30–32], magnetic molecules [33–35] or semiconductor-based qubits [36–38].

So while the five DiVincenzo criteria for quantum computing could be fulfilled by physical qubit implementations in various different platforms, the concept of 'scalability' adds another layer of difficulty, as it involves not only these fundamental requirements but also technological considerations.

1.2. Scaling up with semiconductor spin qubits

By the end of 2023, both IBM and the startup Atom Computing have developed quantum processors employing over 1000 qubits, IBM using superconducting qubits [39], and Atom Computing employing neutral atom-based qubits [40]. While this marks a significant milestone, it is still far away from universal practicability, and a lot more progress will have to be made to further increase the qubit number and reduce error rates.

A simple but very important difference between the various approaches to implement quantum processors become apparent when considering the physical size of the qubit. A recent proposal for a microwave-trapped ion quantum computer hosting 2 billion qubits puts the required area to an astonishing size of more than 100 m x 100 m [41, 42]. The same number of superconducting qubits is estimated to require an area of 5 m x 5 m [3, 43]. Qubits defined by the spin states of semiconductor quantum dots, on the other hand, could fit in an area of less than 5 mm x 5 mm. [44–46]

In addition to their small footprint, semiconductor-based qubits further have demonstrated single and two qubit gate fidelities exceeding the error correction threshold [47–49]. Furthermore, high-fidelity operations at elevated temperatures [50–53], with qubit operations possible at temperatures up to 4 K[54], significantly increase the available cooling power and ease the integration with classical control electronics. Additionally, multi-qubit processors have been implemented across various heterostructures [55–57].

Further, industrial CMOS fabrication technologies have advanced to the point where they can produce classical processors containing up to trillions of MOSFETs (metal-oxide-semiconductor field-effect transistors) [58]. Utilising these fabrication techniques in the production of semiconducting qubits has the potential to enhance reproducibility and uniformity, as well as simplify the optimisation and fine-tuning of qubit parameters. These are all crucial steps towards the realisation of a universal quantum computer. Recent demonstrations of semiconductor qubits fabricated with CMOS-compatible technology show promising progress, with quantum dot yields exceeding 99 % [59–62].

The goal of this thesis is to demonstrate the feasibility and quality of spin qubits hosted in a silicon/silicon-germanium heterostructure, fully fabricated by an advanced industrial CMOS 300 mm wafer process line. This thesis starts with a brief review of the current state-of-the-art regarding implementations

of semiconductor spin qubit architectures and presents possible ideas in order to overcome the challenges of upscaling toward the achievement of universal quantum computing.

Next, the fabrication processes used to produce the samples in this work are described, along with the development of the experimental setup necessary for addressing and manipulating the qubits. The experimental results begin with an explanation of quantum dot formation and charge state control, followed by valley splitting measurements needed to identify the possible working region for performing spin manipulation measurements. The final chapter describes the measurement procedures which were used to characterise qubit manipulation speed, spin coherence times and single qubit gate fidelities.

2. Achieving universal quantum computing with silicon spin qubits

This chapter provides a brief review of recent advancements in the field of semiconductor-based quantum computing, with a focus on a potential implementation of an universal quantum computer, in which the quantum information is encoded in spins of electrons or holes confined in quantum dots. It begins by introducing a possible architecture that combines the strengths of classical semiconductor transistor technology with novel quantum processors and couplers, in order to achieve the required addressability and connectivity for large-scale quantum computing.

The chapter further explores progress in translating academic quantum processor concepts to industrial large-scale clean rooms and 300 mm wafer process lines. Then follows a short introduction to the most commonly used heterostructures for quantum computing, with the focus on the silicon/silicon-germanium heterostructure, which is worked with in this thesis. The chapter concludes with an explanation of the DiVincenzo qubit, as utilised in this thesis.

2.1. Large scale quantum computing architecture

As mentioned in the introduction, excellent scalability is often argued for semiconductor-based qubits, based on the success of classical semiconductor integrated circuits. However, the wiring and interconnection requirements for quantum circuits differ significantly from those in classical circuits, as each qubit requires individual routing of direct current, pulsed, and, in some cases, microwave control signals from external sources.

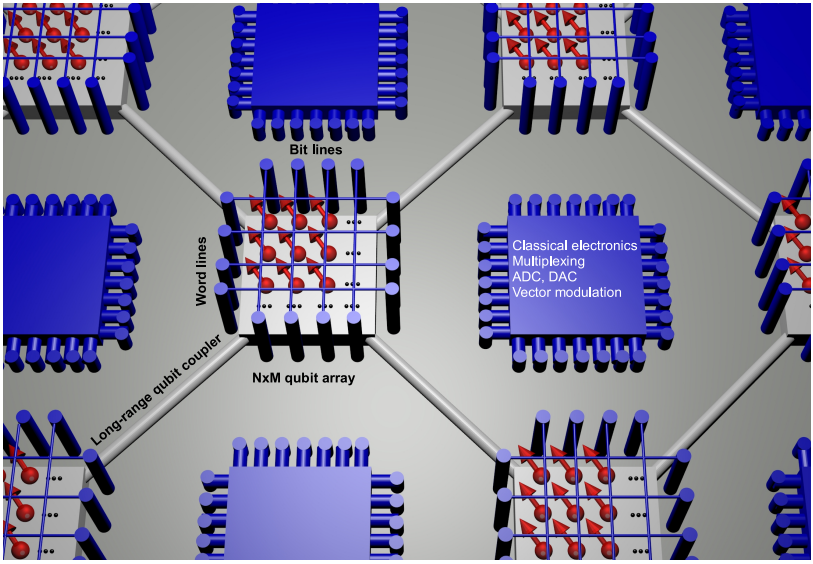

Figure 2.1.: A potential architecture for a universal semiconductor-based quantum computer. The local electronics would incorporate ADC and DAC converters, along with vector modulation, reducing the number of control lines that need to interface with external systems. Long-distance qubit couplers provide space for local electronics to manage small, dense NxM qubit arrays. Charge-storage capacitors for biasing quantum dots, in analogy to DRAM. Individual qubit communication can be achieved through a matrix of word lines and bit lines, in analogy to classical DRAM. Taken from [64].

An architecture which aims to combine the strengths of classical control electronic with quantum processors in order to overcome wiring boundaries for large scale quantum circuits is presented in Figure 2.1. At the core of the architecture is a 2D NxM qubit array, which is connected and controlled by a matrix structure of control lines, similar to the implementation in classical dynamic random-access memory (DRAM). Two-dimensional qubit arrays enable both high-density qubit packing, which is advantageous for large-scale applications, and simplified implementation of error correction methods such as the surface code. Such error correction is possible as long as the probability of error per operation remains below the accuracy threshold, which is approximately 1 % for the surface code, a method that can be operated on two-dimensional qubit arrays with nearest-neighbor couplings [3, 63].

Depending on the limitations given by the dense NxM qubit array processor, additional methods are needed to couple individual processor units over larger distances. Methods such as coupling electron spins to superconducting microwave cavities [65–68] and electron shuttling gate architectures with time-varying gate voltages [69–72] have already been demonstrated and are introduced in more detail in Section 2.1.2.

The long-range couplers would also create space for implementing local electronics, such as multiplexers, to further reduce the fan-out of required connection lines to the exterior of the cryostat. Further, it would be possible to locally integrate analog-to-digital and digital-to-analog converters for enhanced low-noise voltage control and signal readout, as well as low-power vector modulators for precise qubit manipulation. While integrating the classical electronics on the same wafer as the qubit processors would be ideal, the limited cooling power available at temperatures below 100 mK may be a restricting factor. An alternative approach is to place the classical electronics on a separate chip, thermalised at the 1 K or 4 K stage, where orders of magnitude higher cooling power is available. This setup would require an additional interconnection between the two chips, but it is achievable. Following the same argument, developing high-fidelity spin qubit processors that can operate at 1 K or 4 K would be a milestone, as it would drastically ease the cooling power limitations of large-scale quantum computers, and promising results have already been demonstrated in this regard [50, 53, 54].

2.1.1. Qubit interface to classical electronics

In order to efficiently wire and connect all individual qubits in a large scale quantum processor, a possible adaptation of the matrix based connections of existing DRAM technology can be implemented. Figure 2.2**a** shows a schematic of a charge-storage capacitors in order to bias quantum dots, similar to DRAM for classical electronics. Rather than connecting every gate continuously to a voltage source, an individual gate is connected to a capacitor that stores the desired voltage. The voltages can be set efficiently via a cross-bar addressing scheme consisting of a matrix of word lines (W) and bit lines (B). A voltage to the qubit gate $Q_{i,j}$ will be applied by biasing line B_j and setting W_i to high, so the classical transistor switch is on. The charge is stored on the storage capacitor $C_{i,j}$ when setting line W_i low again.

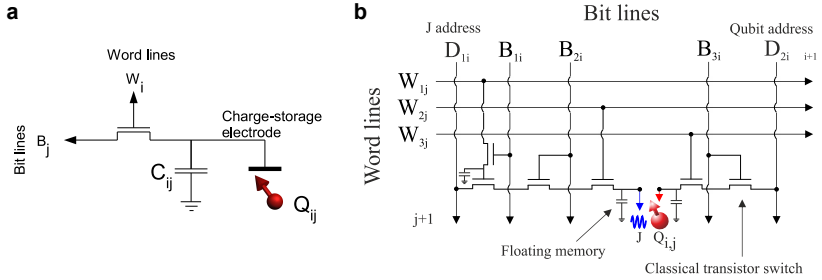

Figure 2.2.: a Schematic of charge-storage capacitors in order to bias quantum dots, similar to DRAM for classical electronics. Communication with individual qubits is realised by pairs of word (W) and bit lines (B). A voltage can be applied to the qubit gate $Q_{i,j}$ via B_j by setting W_i high, and stored on capacitance $C_{i,j}$ by subsequently setting W_i low. Adapted from [64]. **b** A matrix composed of word lines and bit lines, extended by additional data lines $D_{i,j}$, which can be used for manipulation pulses or qubit readout. Adapted from [74].

Depending on the exact qubit processor architecture, this addressing scheme can be expanded in complexity, by additional data lines $D_{i,j}$ used for qubit manipulation pulses or qubit readout, as illustrated in Figure 2.2**b**

In classical DRAM, charge-storage electrodes require periodic refreshing to compensate for leakage or fluctuations in capacitive coupling with nearby structures. For example, typical DRAM refresh intervals are around 64 ms, with each refresh cycle taking approximately 30 ns. Although the voltage tolerances in quantum dots are more demanding, leakage is significantly reduced at temperatures of a few Kelvin or lower, suggesting that a similar approach might be practical. Experimental measurements have shown voltage drifts of around 8 mV/h in charge-storage electrodes integrated with quantum devices [73], and this drift can potentially be minimized further.

2.1.2. Long range quantum processor couplers

Several methods have been investigated to couple spin qubits over larger distances, including spin coupling through an intermediate quantum dot [75, 76], capacitive coupling [77], electron shuttling [69, 71, 78], and coupling electron spins via superconducting microwave cavities [65, 79, 80]. While the first two methods are still limited to sub-micron distances and more interesting for dense qubit arrays with the possibility to go beyond nearest-neighbour

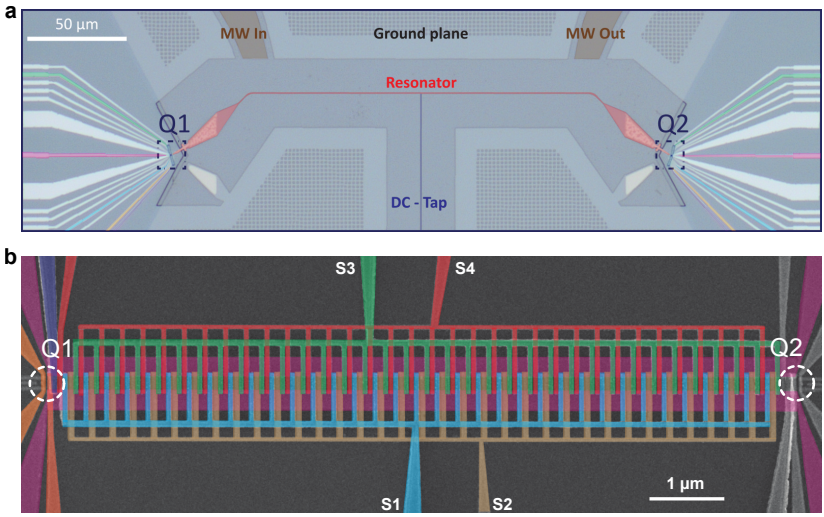

Figure 2.3.: a Coloured SEM image of the gate architecture which enables the formation of two quantum dots, which are coupled over a distance of 250 µm by a superconducting NbTiN resonator. The quantum dots are formed in the regions indicated by the blue boxes and labeled Q1 and Q2. Adapted from [65]. **b** Coloured SEM image of a 10 µm long electron shuttle device, called quantum bus (QuBus). The quantum dots are formed/loaded at the positions indicated by the white circles and labeled Q1 and Q2. Phase-shifted sine voltage signals are applied at the four "clavier" gates to transport the electron along the shuttle pathway. Adapted from [78].

coupling, electron shuttling and superconducting microwave cavity coupling have demonstrated qubit coupling across distances from tens to hundreds of microns.

Figure 2.3**a** displays a coloured SEM image of a device architecture enabling the formation of quantum dots coupled over a distance of 250 µm via a superconducting NbTiN resonator. Each end of the resonator is used as a barrier gate of a qubit, and the spin-spin interaction between the distant quantum dots is mediated by virtual photons in the resonator. This setup allows coherent two-qubit gates to be performed over the entire 250 µm length of the resonator [65]. Although long-range coupling through photons achieves long coupling distances at high speeds, incorporating additional superconducting resonators as part of the quantum dot control gates introduces additional layers of complexity that must be considered for scalable architectures.

Figure 2.3**b** shows a coloured SEM image of the electron shuttling architecture for long-range coupling of distant electron quantum dots. Electrons can be loaded into the shuttling channel from the quantum dots formed at the locations marked by white circles. The electrons are shuttled by applying sinusoidal voltages to the four "clavier" gates, S1-S4. The sinusoidal signals are phase-shifted with respect to each other, creating a wave-like voltage modulation that forms potential wells that allow the electron to move along the channel. In this device, a charge shuttling fidelity of 99.7 ± 0.3 is achieved for transporting an electron from one side to the other and back.

This shuttling architecture is particularly advantageous because it uses the same overlapping gate structure as many other quantum dot architectures, ensuring minimal increase in complexity for integration with existing quantum processors.

In addition to charge shuttling, coherent spin shuttling has also been demonstrated [81, 82], as well as an active two-qubit gate scheme involving shuttling [83].

2.1.3. Qubit processor units and industrial scaling

As mentioned above, the core of the universal quantum computing architecture will the qubit processor. To date, the demonstration of the larges semiconductor-based quantum processor is a six qubit processor in a 1D chain of quantum dots [55]. A coloured SEM picture is shown in Figure 2.4**a**. Six individual qubit quantum dots are formed below the blue gates labeled P1-P6, called plunger gates, which are used to control the quantum dot energy. The green gates B0-B6 are barrier gates and used to control the tunnel coupling to adjacent quantum dots, which enables two qubit gates to nearest neighbours. Further, coherent spin shuttling was demonstrated in a device of the same architecture. The electron can be shuttled from one side to the other, similar to the device shown in Figure 2.3**b**. While the total distance of the shuttle is smaller in the six qubit device, the possibility to shuttle an electron back and forth over a cumulative distance of 10 µm in less than 200 ns and with a fidelity of 99 % to preserve the spin coherence of the electron [84].

Another possible implementation of a quantum processor architecture is shown in Figure 2.4**b** where four quantum dots are arranged in a 2x2 grid and also nearest neighbour coupled. Universal one and two qubit operations

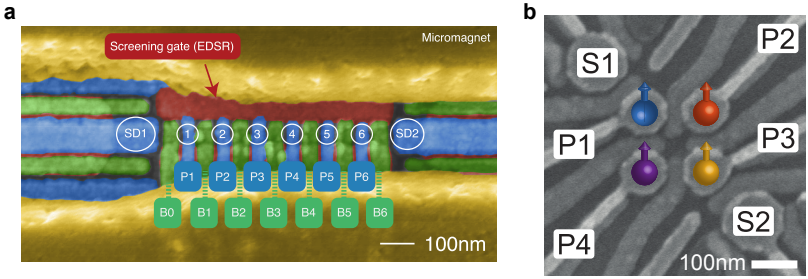

Figure 2.4.: a False coloured scanning electron microscopy (SEM) image of a six qubit processor based on a silicon/silicon-germanium heterostructure. The quantum dots hosting the qubits are formed below the six electrostatic gates in blue, labeled P1-P6. Taken from [55]. **b** SEM picture of a four qubit processor in a 2x2 array structure, based on a germanium/silcon-germanium heterostructure. Taken from [56].

were demonstrated in this device [56]. Such a 2D architecture would benefit from even better scalability and the option of a possible surface code error correction scheme, and efforts to scale it up to a 4x4 grid are in progress [85]. Other multi qubit processor architectures involve singlet-triplet qubits, for which the universal control of four qubits was demonstrated [86], or electron spins coupled to nuclear spins of donor atoms , where the coherent coupling of an electron spin to three individual nuclear spins were demonstrated [57].

But while there are an unlimited amount of ideas on how scale up to larger quantum processors [37, 66–68, 74, 75, 77, 87–107], the tools to fabricate high quality devices by academia are drastically more limited compared to the resources, industrial classical semiconductor manufacturer posses, where the transistor count of a classical processor now already exceeds the trillion range [58]. Industrial state of the art 300 mm wafer process lines are able to achieve unrivaled control precision over thin film deposition, doping, and etching processes, essential for building multilayered structures required in modern semiconductor devices. If this infrastructure could be applied to achieve similar precision in the fabrication of semiconductor-based spin qubits, it would mark a significant milestone. Laboratory-based devices often experience low yield and significant inter-device variability. Consequently, most spin qubit results are achieved through an extensive screening process, where numerous devices are tested to find one with optimal electrostatic behaviour.

Qubits fabricated using industrial semiconductor manufacturing technologies have recently been demonstrated [59–62, 108, 109]. This has also led to the development of large-scale characterisation tools to assess device yield and variation in identically designed devices, with reported yields of functional quantum dots exceeding 99 % [62]. This is where the present work becomes highly relevant.

Demonstrating functional qubits within a silicon/silicon-germanium heterostructure, fully fabricated using an industrial 300 mm wafer process line, would represent another crucial milestone towards the realisation of a large-scale, universal quantum computer.

2.2. Silicon/Silicon-Germanium heterostructure

A silicon/silicon-germanium (Si/SiGe) heterostructure is a layered structure composed of alternating layers of silicon (Si) and silicon-germanium (SiGe) alloy. A schematic illustration is shown in Figure 2.5**a**. From bottom to top, a thick SiGe buffer layer is grown, usually top of a Si substrate. It often starts with a gradually increasing Ge concentration in the SiGe layer, in order to minimise strain, followed by more SiGe of constant concentration. On the unstrained SiGe layer, a thin Si layer of 5-15 nm is grown. Because of the latice missmatch between the Si and SiGe, strain is induced in the Si layer, which importance is discussed later in this section. In this silicon layer, the two dimensional electron gas (2DEG) is induced later and is called quantum well. On top of the silicon quantum well, another SiGe spacer layer is grown with a usual thickness between 20-50 nm. A final thin Si layer (1-2 nm) is grown on top of the SiGe spacer before the oxide is deposited, and the thin Si layer protects the SiGe spacer from oxidation. Metal gates on top of the heterostructure are then used to accumulate and confine electrons in the quantum well.

The principle on how the 2DEG is formed in the quantum well is illustrated in Figure 2.5**b** and **c**. The conduction band gap of pure silicon is lower than for Ge, and the conduction band energy of SiGe can be tuned by the Ge content inside the alloy. For no applied gate voltage, the conduction band of whole heterostructure is above the fermi energy E_F the conduction band is unoccupied. Further, because of the thickness of the two silicon layers, the

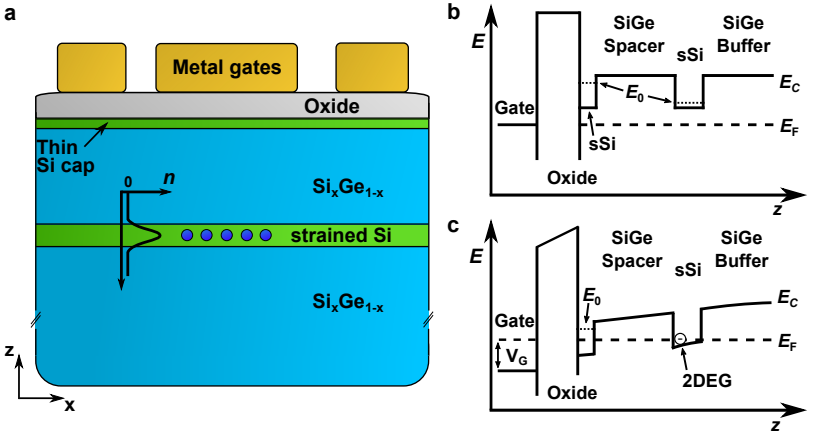

Figure 2.5.: a Example of a SiGe heterostructure. A Si, strained between two SiGe layers, is used as the quantum well, in which a two dimensional electron gas (2DEG) can be accumulated by gates deposited on top of the heterostructure. A thin Si cap protects the SiGe layer from oxidation, and an oxide layer insulates the metal gates from the heterostructure. **b** Conduction band energy E_C in z-direction of the heterostructure. The conduction band edge of the SiGe layers is higher in energy than for pure Si. **c** Conduction band energy E_C for a possitive applied gate voltage V_G. The positive gate voltage pulls down the conduction band of the heterostructure. As soon as the ground state energy E_0 of the conduction band of the strained Si layer is pulled below the fermi energy E_F, a 2DEG starts to accumulate. Because of the very thin nature of the Si cap, the ground state energy for this layer is higher compared to the Si quantum well and no electrons accumulate in the Si cap. Inspired by [110].

ground state energy E_0 in the thin layer, is higher, compared to the ground state energy in the thicker Si layer.

When applying a positive gate voltage V_G as illustrated in **c**, the conduction band of the heterostructure is pulled to lower energies. As soon as the ground state energy of the Si quantum well is pulled below the fermi energy E_F, the conduction band can be occupied in this layer, and a 2DEG is accumulated.

The goal of this heterostructure is to decouple the accumulated electrons, which are later used to form quantum dots and qubits, from the semicondcutor-oxide interface. This interface is kown to posess a high defect density [111], which can act as fluctuating two level systems and induce charge noise or act as scattering sites for electrons [112–115]. This is especially crucial, because it was shown that charge noise is a limiting factor regarding two qubit gate

fidelities [116], and investigation and reduction of charge noise is an ongoing research topic and of general interest [110, 117–119].

2.2.1. Silicon valleys

While gallium-arsenide/alluminum-gallium-arsenide was for a long time the preferred heterostructure for quantum dot devices and investigation of spin qubits [120–123], because of its clean interfaces leading to high electron mobilities, and the less challenging gate litography because of larger quantum dot sizes. GaAs heterostructures suffer from magnetic noise by fluctuating nuclear spins in the vicinity of the quantum dots/qubits, which led to low spin coherence times. And because GaAs has no isotope without a nuclear spin, over time, the choice of material shifted more and more to Si based architectures.

Silicon has the three stable isotopes ^{28}Si, ^{29}Si, ^{30}Si with the respective natural abundance of 92.23 %, 4.69 %, 3.09 %, where only ^{29}Si posesses nuclear spin [124]. So by isotopical enrichment of ^{28}Si, the spin noise can be reduced which resulted in long spin coherence times in silicon.

But while the reduced magnetic noise is a great advantage, using Si introduces a different challenge compared to GaAs. Compared to the direct band gap in GaAs, Si posesses an indirect band gap of 1.12 eV at room temperature [125], increasing to 1.17 eV at 4 K [126]. In bulk silicon, there are six degenerate conduction band minima in the Brillouin zone (valleys) as depicted in Figure 2.6**a** and **b**.

This degeneracy is problematic for spin-qubit operation because the Pauli exclusion principle, which normally forbids two electrons with the same spin to occupy the orbital ground state, gets circumvented and the two-qubit gate fails. Therefore, the previously mentioned strain of the Si quantum well becomes important. The large in-plane strain lifts the energies of the inplane (x and y) valleys. The remaining two-fold degeneracy of the z valleys is broken by electronic z confinement induced by electric fields and by the quantum well [128]. The breaking of the twofold valley degeneracy is very sensitive to atomic-scale details of the interface and can therefore vary for different locations in the device [82, 129], and has to be determined in order to know the alowed working regime of the qubits. Figure 2.6**c** shows a summary of the valleysplitting, from bulk silicon to the confinement in strained silicon.

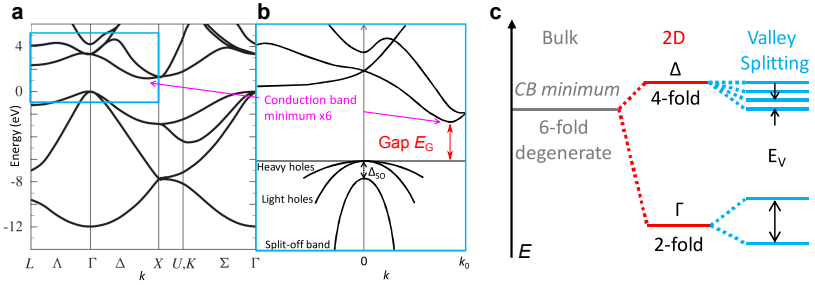

Figure 2.6.: a Band structure diagram of bulk silicon. **b** A zoomed-in view of the indirect conduction band gap. The minimum close to the end of the Brilloin zone is six-fold degenerate. **c** Valleysplitting of a strained silicon quantum well. The bulk six-fold degeneracy gets lifted by the strain into four higher energy valleys ($\pm x$ and $\pm y$ valleys) and two low energy valleys ($\pm z$ valleys). The final degeneracy gets lifted due additional confinement by the quantum well and by gate voltages. Adapted from [127].

Because of the many advantages a Si/SiGe heterostructure brings, many of the impressive results regarding spin qubit devices where achieved in Si/SiGe heterostructures. The six qubit processor [55], high fidelity coherent spin shuttling [84], a working device with 12 individual qubits [109], a tunable 2x2 quantum dot array [130] and the record for two qubit gate fidelities of semicondcutor based qubit devices [36, 131], by using Loss-DiVincenzo qubit architectures in Si/SiGe. The promise of combining all the advantages of the Si/SiGe heterostructure with the unmatched precision of industrial 300 mm CMOS process lines holds great promise in the process of developping a large sclae quantum computer.

2.3. Loss-DiVincenzo qubit

In 1998, Daniel Loss and David P. DiVincenzo proposed a quantum computing architecture utilizing the spin states of single electrons confined in quantum dots as qubits [87]. In order to illustrate the working principle of the qubit, the qubit state is represented as a vector on a sphere of radius one, the Bloch sphere. The Bloch sphere is a geometric representation of the pure state space of a two-level quantum system. It is named after physicist Felix Bloch [132, 133], in honor of his foundational work in nuclear magnetic resonance,

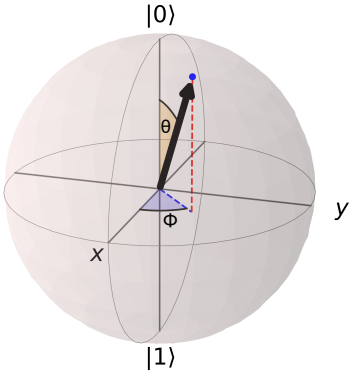

Figure 2.7.: Representation of a qubit state in spherical coordinates on the Bloch sphere

which inspired representations of two-level quantum systems. A qubit state vector

$$|\Psi\rangle = \alpha\,|0\rangle + \beta\,|1\rangle\,, \tag{2.1}$$

can be represented on the Bloch sphere by:

$$|\Psi\rangle = \cos(\theta/2)\,|0\rangle + e^{i\phi}\sin(\theta/2)\,|1\rangle\,, \tag{2.2}$$

with θ being the polar angle measured from the z-axis of the Bloch sphere, and ϕ being the azimuthal angle measured from the x-axis in the xy-plane of the Bloch sphere. The two poles of the sphere represent the basis states $|0\rangle$ (north pole) and $|1\rangle$ (south pole), and points on the equator represent equal superpositions like $1/\sqrt{2}(|0\rangle + |1\rangle)$. The time evolution of the qubit can be described as the trajectory of the state vector on the Bloch sphere.

The Loss-DiVincenzo (LD) qubit encodes quantum information in the spin state of a single electron, where the spin-$\frac{1}{2}$ of the electron serves as a natural realisation of a qubit. A static magnetic field lifts the degeneracy between the electron's spin-up and spin-down states, while a transverse AC magnetic field drives coherent rotations between these spin states. Figure 2.8 illustrates the physical implementation of a LD spin qubit, its representation on the Bloch sphere, and the two level energy splitting of the two qubit states.

The encoding for an LD qubit involves a direct mapping $\boldsymbol{S}_i = -\boldsymbol{\sigma}_i/2$, between spin operators and encoded Pauli operators. In the regime of tight electronic

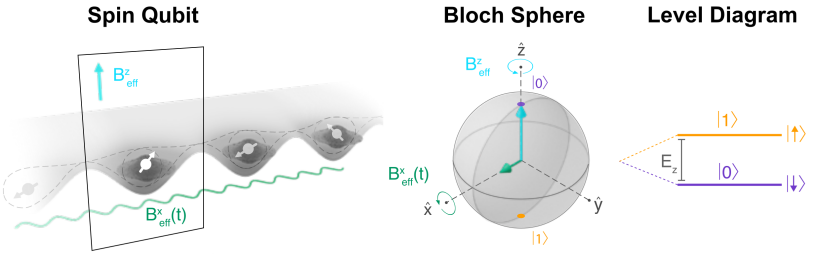

Figure 2.8.: Single electrons confined next to each other in quantum wells (left), Bloch sphere representation (centre), and qubit energy level diagram (right). The qubit energy splitting is tuned by a constant external magnetic field, which lets the spin precess around the z-axis with the same frequency as the energy splitting. An oscillating magnetic field in resonance to the qubit frequency, perpendicular to the constant field, can drive the qubit, which rotates the qubit vector on the bloch sphere around the x or y-axis. Adapted from [36].

confinement, with one electron per quantum dot, the electron spin dynamics are governed by the Heisenberg exchange Hamiltonian and the single-electron Zeeman Hamiltonian, resulting in a total Hamiltonian of the form [36]:

$$H(t) = \frac{1}{4}\sum_{i,j} J_{i,j}(t)\boldsymbol{\sigma}_i \cdot \boldsymbol{\sigma}_j + \frac{1}{2}\sum_i g_i \mu_B \boldsymbol{B}_i \cdot \boldsymbol{\sigma}_i, \tag{2.3}$$

with the time dependent exchange coupling $J(t)$, the effective magnetic field $\boldsymbol{B}$, and the Landé g-factor for the electron at the position i.

The exchange interaction arises from the requirement that the total wavefunction of two electrons—which includes both spatial and spin components—must be antisymmetric, as dictated by the Pauli exclusion principle [134, 135]. When electrons overlap spatially, the energy of the spin-singlet state is reduced relative to the spin-triplet states by an amount called the exchange coupling J. This effect occurs because electrons in the singlet state can move to and from the same location (maintaining a totally antisymmetric wave function), while this motion is forbidden for the spin-symmetric (and hence spatially antisymmetric) triplets.

This exchange effect between spins i and j is captured by the Heisenberg exchange Hamiltonian $H = J_{i,j}\boldsymbol{S}_i \cdot \boldsymbol{S}_j$, where $\boldsymbol{S}_i$ denotes the quantum operator for the spin of the electron at site i. From a quantum control perspective, one advantage of spin qubits is that $J_{i,j}$ can typically be tuned over many

orders of magnitude by adjusting gate voltages [136]. This tunability allows for time-dependent two-qubit control, enabling the realisation of two-qubit gates between nearest-neighbor spins [137, 138]. The exact experimental implementation of the universal qubit control will be described in more detail in Section 6.4.

While there are a lot more different qubit encoding schemes based on semiconductor quantum dots [36], the LD qubit type implemented in a Si/SiGe heterostructures holds the the record for the highest two qubit gate fidelities [131] and form the largest semicoductor qubit processors [55, 109] to date.

3. Spin qubit devices and experimental setup

This chapter begins with an introduction to the spin qubit devices used in this thesis, followed by a detailed description of the experimental setup. It describes the ^{3}He/^{4}He dilution refrigerator used to achieve the required operating temperatures, the sample printed circuit board (PCB) for the electrical addressing of all gates, the cabling and filtering of the electrical lines, and the measurement electronics used for device control and data acquisition. The chapter concludes with a brief explanation of the IQ mixing used for coherent spin manipulations.

3.1. 300 mm industrial wafer fabrication at imec

The spin qubit devices characterised in this work were fabricated by our collaborators from the Interuniversity Microelectronics Centre (imec). The heart of imec's headquarters in Leuven, Belgium, possesses a state-of-the-art 7200 m^2 cleanroom, equipped with advanced 300mm wafer processing tools. Unlike university cleanrooms, where wafers are processed less frequently, imec operates 24/7 with dedicated cleanroom staff handling 300 mm silicon wafers. Although the cleanroom is rated as class 1000, wafers are transported between fabrication steps in Front Opening Unified Pods (FOUPs), which provide a class 1 environment. All equipment is designed with loading bays compatible with FOUPs, ensuring wafers remain secure in a controlled setting at all times. Adopting industry-standard, high-quality materials and minimizing human interaction is a promising approach to address the variability in spin qubit devices, a key bottleneck for scaling quantum computing architectures [44, 64].

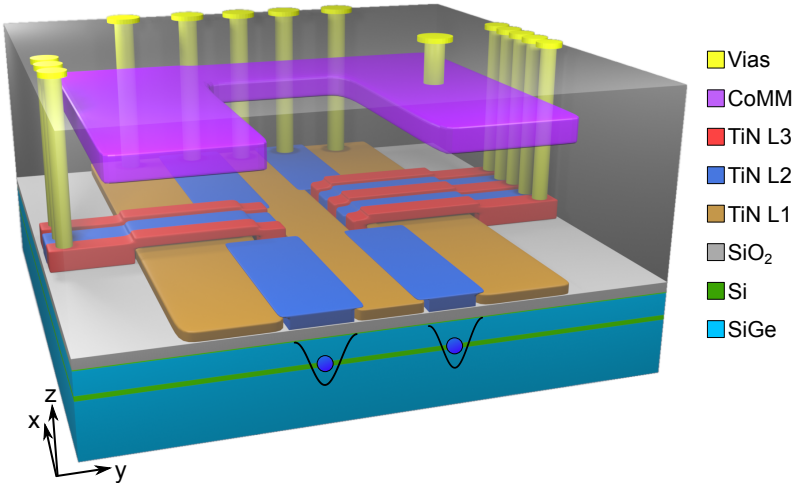

Figure 3.1.: A 3D model of the device. 3-layer TiN gate architecture (orange, blue, red) on the SiGe heterostructure (cyan and green). SiO_2 (grey) insulates the different layers from each other. The electron gas is formed in the buried Si layer. The CoMM (violet) is encapsulated by a SiO_2 passivation layer, and all structures are connected by vias (yellow). In reality, the vias are connected farther from the qubit region, where the gates fan out and become wider. Additionally, the width, length, and height of the CoMM are reduced for better visibility, with only the 300 nm gap of the CoMM shown to scale. Adapted from [139]

The natural Si/SiGe heterostructures used in this thesis are grown on a 300 mm silicon wafer. A 3D visualisation of the device is shown in Figure 3.1. From bottom to top, the heterostructure comprises a 8 µm strained relaxed buffer (SRB) finished by an unstrained 1 µm $Si_{0.75}Ge_{0.25}$ layer of constant concentration. This is followed by chemical vapor deposition (CVD) of a tensile-strained natural Si quantum well of 9 nm and a $Si_{0.75}Ge_{0.25}$ buffer layer of 40 nm thickness. To avoid oxidation of the SiGe buffer, a 2 nm thick silicon cap is grown on top of the heterostructure. Ohmic contacts to the natural Si quantum well are formed by phosphorus implants. Three overlapping gate layers made of titanium nitride (TiN) and insulated by silicon oxide (SiO_2) (From bottom to top: 8 nm SiO_2, 30 nm TiN, 5 nm SiO_2, 20 nm TiN, 5 nm SiO_2, 20 nm TiN) are used for the formation and manipulation of the quantum dots. A cobalt micromagnet (CoMM) module of 250 nm thickness is made in line using a damascene process. A SiO_2 passivation layer is deposited on top of the stack. Vias are etched in this passivation layer to connect the ohmics, gate layers

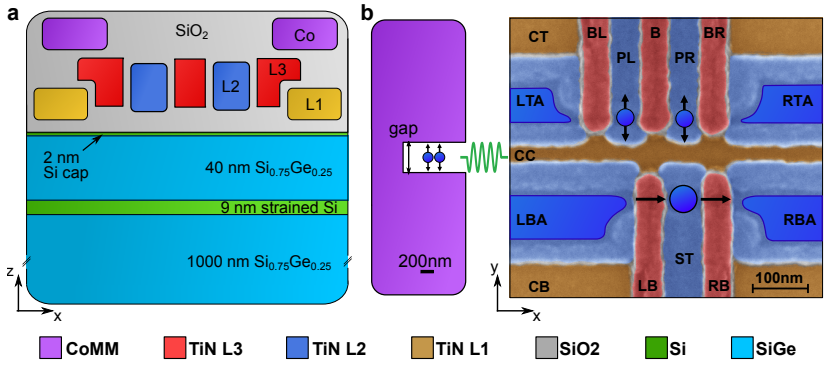

Figure 3.2.: a Schematic of the Si/SiGe heterostructure, the three gate layers, and the CoMM layer. The thicknesses are to scale except for the lowest SiGe buffer layer and the CoMM layer. The quantum dots are formed in the 9 nm strained Si layer. **b** False coloured SEM of the three layer TiN gate architecture for quantum dot and qubit control. The dark blue regions indicate the areas where a mobile 2D electron gas is formed, and the blue dots indicate the position of the formed quantum dots. The black arrows indicate the measured tunnelling current through the sensor dot below the ST gate, and the oscillation direction of the two qubit quantum dots below gate PL and PR. The spatial oscillations are induced by pulsing the central screening gate CC with microwaves. The quantum dots are formed approximately 120 nm below the center of a CoMM gap, creating a local inhomogeneous magnetic field necessary for EDSR manipulation.

and the CoMM. A cut of the heterostructure is shown in Figure 3.2**a** in which all layers are to scale in respect to their layer thicknesses, except the lowest $Si_{0.75}Ge_{0.25}$ buffer layer and the upmost CoMM thickness are reduced in height for better visibility. The 2 nm Si cap is suspected to be even thinner, as part or possibly the entire layer may have been converted to SiO_2 during the growth of the oxide layer.

The gate layout of the device is shown in the false coloured scanning electron microscopy (SEM) picture in Figure 3.2**b**. The architecture is designed to enable the formation of two quantum dots in the single electron regime, later used as qubits, and an adjacent single electron transistor (SET) for readout. Mobile 2D electron gases can be formed below the four accumulation gates LTA, RTA, LBA, RBA, which have a slight overlap with the ohmic implant region further away from the qubit region. The qubit dots are centered below the gap of a C-shaped CoMM, which creates an inhomogeneous external magnetic field at the qubit positions used to manipulate the qubit spin state. Applying a microwave signal to the central screening gate (CC) causes the

Table 3.1.: Device ID of all measured devices

Wafer	Subdie	CoMM gap size
D11	Die12 SD10B	650 nm
D09	Die13 SD10B	650 nm
D09	Die09 SD11B	400 nm
D09	Die05 SD15B	300 nm

position of the qubit dot to oscillate, effectively subjecting the qubit to an alternating magnetic field at the frequency of the applied signal. This principle is called electric dipole spin resonance (EDSR) [140, 141] and is explained in more detail in Section 6.1.

Figure 3.3 shows a scanning electron microscopy (SEM) image of the CoMM and its dimensions. The CoMM on the devices is about 1.5 µm wide and 4 µm long and features different gap sizes which change the resulting inhomogenious magnetic field at the position of the later formed qubit quantum dots. Qubit quantum dots are formed ≈ 120 nm below the CoMM, and the magnetic field strength and gradient for different CoMM geometries and gap sizes were simulated and optimised in [142]. The four spin qubit devices presented in this work, and are listed in Table 3.1. They all possess the same gate architecture but feature different CoMM gap sizes. Also two devices with identical architecture but from different fabricated 300 mm wafers were measured. The coherent spin manipulation measurements presented in Chapter 6 are all performed on the sample with the ID "D09 Die05 SD15B", which features a CoMM gap size of 300 nm. Measurements on the other samples are shown in the Appendix A.1.

3.2. Dilution refrigerator

The samples were cooled down in a home built ^{3}He/^{4}He dilution refrigerator, a Qinu Version XL. The speciality of Qinu cryostats is their speed in which the cryostats cool down and warm up. The time needed to reach temperatures below 100 mK is approximately 7 h, and additional 2 h to reach its base temperature at about 30 mK. The cooling power at 100 mK reaches about

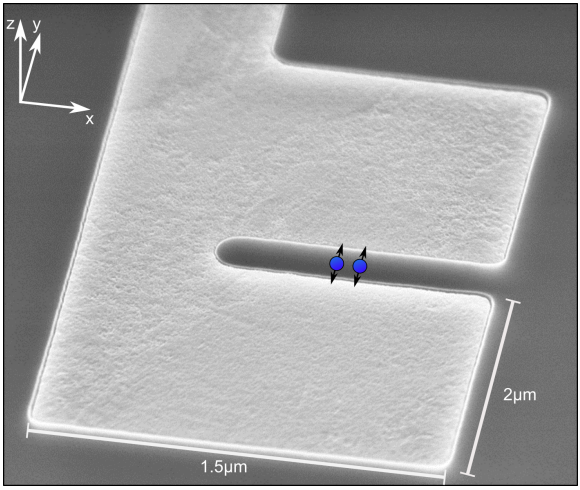

Figure 3.3.: Scanning electron microscopy image of a CoMM with a gap size of 300 nm. The image was taken from an angled viewpoint, so the lengths in the y-direction appear smaller than in the x-direction. The Co layer has a thickness of 250 nm, is encapsulated in SiO_2 and connected to a via in order to be able to ground the micromagnet. The blue dots and black arrows indicate the position and oscillation direction of the quantum dots, which are located in the quantum well approximately 120 nm below the CoMM. Taken from [139]

300 µW. Unlike most conventional cryostats, Qinu cryostats have an upside-down design, where the coldest part, the mK-plate, is located at the top of the assembly rather than at the bottom, as is common in other commercially available systems. A full warm up of the cryostat takes approximately 2 h by introducing ^{4}He exchange gas into the cryo vacuum and heating of the outermost shield. For a detailed description of the working principle and technical details of the Qinu cryostats, see [143].

The specific Qinu version XL used in this work, named "Obelix," is illustrated in Figure 3.4 and has several unique features. The XL version has a larger experimental space and significantly more mass compared to the L version, so an extra line was added to allow the 4 K stage to be directly precooled using liquid N_2 during the cooldown. N_2 becomes liquid at $\approx$ 77 K and can therefore be used to quickly cool down the whole system to about 100 K, at which the cooling with liquid ^{4}He is continued. N_2 becomes solid at $\approx$ 63 K, so after reaching these temperatures and below, the N_2 line leading to the 4 K pot is blocked by solid N_2, and the N_2 line to the 100K stage in parallel

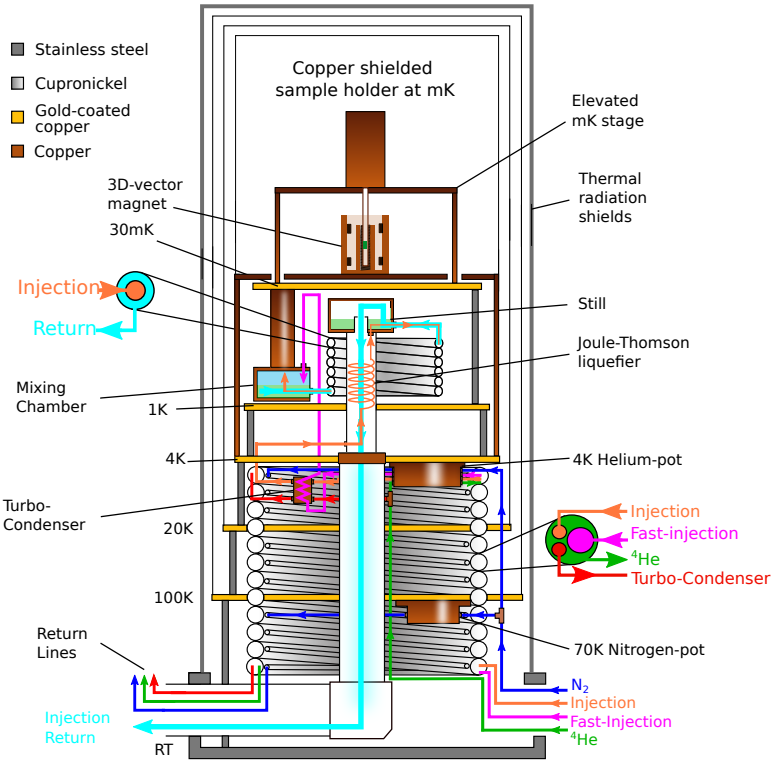

Figure 3.4.: Schematic illustration of the cryostat used in this thesis, named Obelix. Special for Obelix is the elevated second mK stage with a fast-exchangeable sample holder, an extended 4 K copper radiation shield that allows the use of a 3D vector magnet combined with the high cooling power of the 4 K stage, and the possibility to precool the 4 K stage with N_2 during cooldown. Adapted from [144]

can be used further. This drastically reduces the liquid ^{4}He consumption for a cooldown from $\approx$ 20 l, to $\approx$ 6 l, and the ^{4}He consumption per day for operation at mK, to about 13 l/day instead of 19 l/day.

The other unique features include the extended 4 K copper radiation shield, to which the 3D vector magnet can be attached, and the elevated mK stage, which is paired with a fast-exchangeable sample holder. The extended 4 K copper shield allows to bring the 3D vector magnet in nearest vicinity of

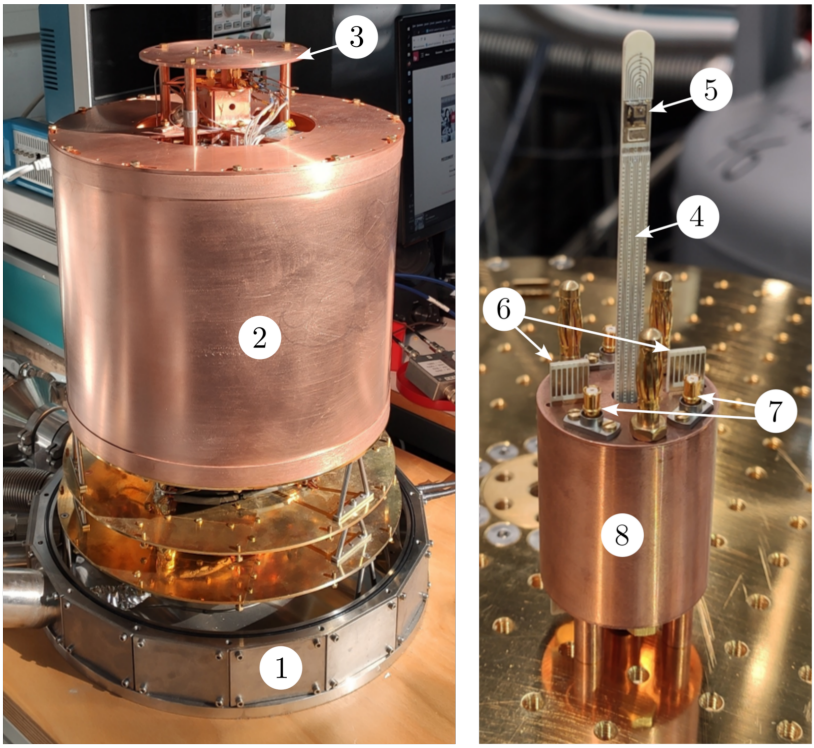

Figure 3.5.: Pictures of Obelix and the Quickswap sample holder. 1: Customizable vacuum access windows. 2: Extended 4 K shield. 3: Elevated mK stage. A detailed view is shown in Figure 3.6. 4: Cold finger of the Quickswap sample holder. 5: Sample space with glued sample. 6: Split-PCI-connection for up to 24 DC lines. 7: SMP-connectors for up to 3 RF lines. 8: Radiation shield hosting the second filtering stage. Adapted from [145].

the measured sample, while profiting from the high cooling power at the 4 K stage. The higher cooling power of the 4 K stage facilitates thermalisation of the superconducting coil compared to thermalisation at the mK stage, resulting in faster total cooldown times. Additionally, the higher cooling power allows faster magnetic field ramping speeds, as it can compensate for the self-heating of the coils caused by eddy currents.

The elevated mK stage was developed to use in combination with the fast exchangeable sample holder, named "Quickswap" system. As the name im-

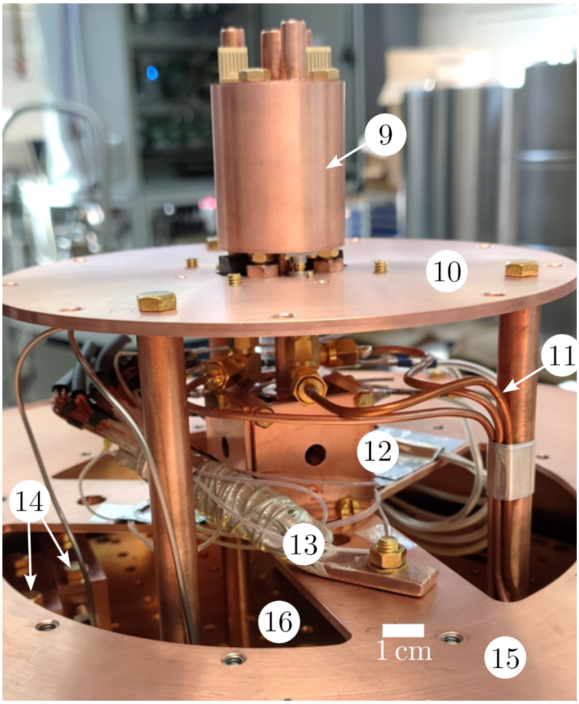

Figure 3.6.: Close-up of elevated mK stage. 9 The Quickswap sample holder inserted upside-down into the elevated mK stage. 10 Elevated mK stage. 11 Three coaxial copper cables connecting to to the three SMP connectors on the sample holder via SMA to SMP feedthrough adapters. 12 Superconducting 3D vector magnet. 13 Thermal anchor for the high current lines supplying the magnet. 14 DC line filter boxes. 15 The extended 4 K copper radiation shield. 16 The lower mK stage. Adapted from [145].

plies, it enables the exchange of a PCB with a mounted sample in just a few minutes. The connection to the cryostat wiring is achieved by plugging in the SMP and split-PCI connectors, while mechanical stability is provided by three 4 mm banana plugs, which fit into corresponding holes on the elevated mK stage. This setup allows the sample to be prepared in advance while the cryostat is still in operation. Swapping the sample holder with a new sample then requires minimal time, thereby reducing the cryostat's overall downtime.

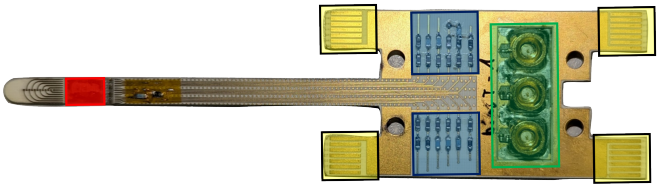

Figure 3.7.: Photograph of the sample PCB with coloured highlights. The SMP connectors used to connect the RF lines on the PCB to external RF lines are highlighted in green. The PCI connectors, used to connect the DC lines to their counterparts inside the cryostat, are highlighted in yellow. The second RC filtering stage of the DC lines is highlighted in blue. The position where the sample chip is glued and wire-bonded to the adjacent ends of the RF and DC lines is highlighted in red. Adapted from [144].

3.3. Sample PCB

A detailed view of the sample PCB that enables the Quickswap system is shown in Figure 3.7, and was designed by Tino Cubaynes. The PCB features in total 24 DC lines and 3 RF lines. The PCB has allocated pads which allow the integration of onboard RC filters for the DC lines. The DC lines are connected to two sets of split PCI connectors, one set on the bottom and one set on the top of the main PCB. This allows the possibility to provide a galvanic ground connection for the DC lines at all times, in order to prevent damage from electrostatic discharge effects. The RF lines are connected by SMP connectors, and guided to the sample space by three individual coplanar waveguides, designed for frequencies up to 20 GHz. The sample space is located close to the end of the long cold finger, used to insert the sample in the centre of a 3D vector magnet. The sample is glued onto a 12 x 6 mm gold-coated copper plate, which can serve as a back gate or ground plate. The sample is then wire-bonded to the RF and DC lines that are positioned around the sample space. Optional resistive bias-tees are added by soldering a capacitor between the inner conductors of an RF line and a resistor in line of the respective DC line. The lines are then connected by wire bonds at the point closest to the sample. The image shown in Figure 3.7 displays mounted bias-tees for the lower two RF lines. The bias-tees are composed of 15 nF SMD capacitors and 10 MΩ Metal Electrode Leadless Faces (MELF) resistors.

The sample PCB shows parasitic capacitive coupling between the RF lines and the nearest DC lines for frequencies above 16 GHz, where the relevant factor

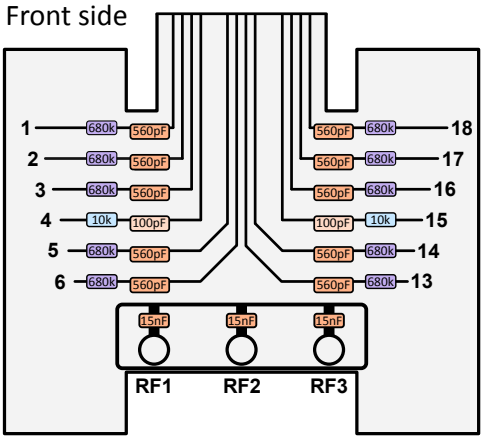

Figure 3.8.: Schematic of the PCB shown in Figure 3.7, where the front side DC lines and RF connectors are labeled. Also included are the resistors and capacitors for the second DC filter stage, which are discussed in more detail in Section 3.4.

is the distance between the DC line and the soldered SMP connector port of the RF line. More specifically, RF line 3 shows the strongest coupling to DC line 13, while RF line 1 shows the strongest coupling to DC line 6. Figure 3.8 shows a schematic in which all front side DC lines and RF connectors are labeled. This cross-talk was measured across three different PCBs and is crucial to consider when selecting the DC and RF lines for connecting to the sample. If not properly accounted for, this cross-talk can introduce significant noise into the system when coupled to the wrong gate. However, if used correctly, it can be turned into an advantage.

The initial qubit measurements were performed with an RF line directly wirebonded to the manipulation gate, but the observable manipulation speeds were limited due to sample heating, which resulted in a loss of SNR. In contrast, when using RF line 3 without a direct wirebond connection to the sample, and connecting DC line 13 to the qubit manipulation gate, orders of magnitude higher qubit manipulation are achieved before any heating effect was observed. This line configuration was tested across three different PCBs and four different qubit samples, consistently demonstrating the same behaviour.

The reason for this orders-of-magnitude improvement in performance remains unclear. The hypothesis is that heat dissipated at the last attenuator, thermalised at the mK stage, is directly conducted to the sample when the RF line has a direct thermal connection to it. In contrast, when RF line 3 is capacitively coupled to DC line 13, but not connected to the sample directly by a wirebond, the electromagnetic signal is transmitted without direct heat transfer via electrons between the lines. Due to its legendary performance, this RF 3 to DC line 13 cross-talk has been named the "Ghost line" and should be taken into account for future use cases and PCB designs.

3.4. Cabling and measurement electronics

The dilution cryostat is equipped with 48 DC lines and 6 RF lines. The DC lines consist of superconducting NbTi filaments embedded in a constantan matrix, with a total wire thickness of 100 µm. The DC lines are bundled in groups of 12, encased in Apiezon grease, and housed in a CuNi capillary with an outer diameter of 1.7 mm. The CuNi capillary is later galvanically connected to ground, providing both electromagnetic shielding and mechanical stability. The Apiezon grease enhances thermal conductivity to the CuNi capillary.

Each RF line consists of three CuNi coaxial cables, one from room temperature to the 4 K stage, from the 4 K to the 1 K stage, from the 1 K stage to the 30 mK stage, and a final copper coaxial cable connecting the first 30 mK stage with the elevated one. The total attenuation of the three RF transmission lines, from the outer SMA connector of the cryo access window, up to the elevated mK stage and the SMP feedthrough adapters, is shown in Figure 3.9 for frequencies up to 20 GHz. Additional RF attenuators of 3, 6 and 10 dB are built in at the 4 K, 1 K and 30 mK stage respectively.

The DC lines are filtered by two RC low pass filter stages at mK with cutoff frequencies of 250 Hz for the static gate voltages, and 60 kHz for DC lines used for current measurements through the charge sensor and qubit plunger voltage pulses. Additionally, every line was filtered by a LFCN-80+ for mid range frequency filtering between 225 MHz and 4500 MHz. A schematic of the filter configuration and the used passive components is shown in Figure 3.10. The LFCN-80+ and the first RC filter are soldered on a dedicated filter PCB and placed inside a filter box, thermalised at the 30 mK stage. The second RC filter is soldered on the sample PCB directly as shown in Figure 3.7 or

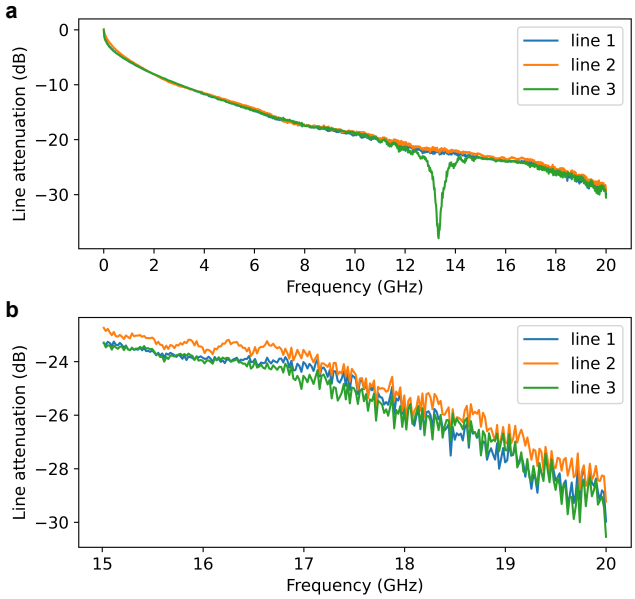

Figure 3.9.: Measured line attenuation of the three built in RF lines from the external SMA connector at the outer cryostat window, up to the SMP connector at the elevated mK-stage, at room temperature. **a** shows the full frequency window from 10 kHz to 20 GHz, while **b** shows a close-up of the frequency window from 15 to 20 GHz more relevant for later qubit operations.

Figure 3.8. All electrostatic control gates of the samples are connected to DC lines equipped with the 250 Hz filters. Only the source and drain contacts and the two qubit plunger gates are connected to the "fast" DC lines with the 60 kHz filters, to be able measure shorter signals and to be able to perform faster pulses on the plunger gates. The central screening gate, also used for EDSR drive is connected to DC line 13 and driven with RF line 3, as explained in the previous section.

Figure 3.11 presents a schematic illustrating how the measurement electronics are interconnected and connected to the cryostat. All DC lines in the cryostat are connected via an external breakout box, with the voltages controlled by an Adwin Pro II system from Jaeger Messtechnik. The source drain currents are converted to a voltage at room temperature by an SP983c Basel Precision Instruments I-V converter, and the voltage is digitized by an analogue input

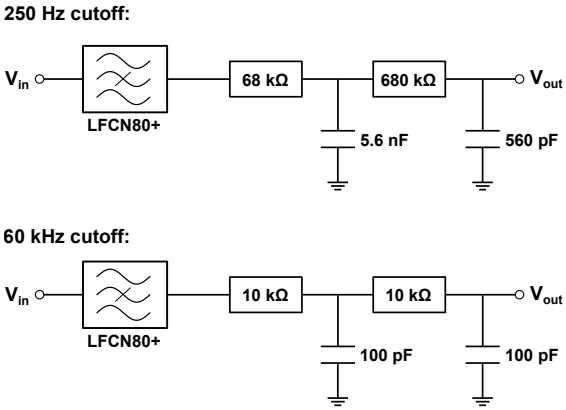

Figure 3.10.: DC filter configuration. The LFCN80+ and the first set of RC filters are located and thermalised in a copper filter box at the 30 mK stage, and the second set of RC filters are soldered directly on the used sample PCB.

module of the Adwin Pro II. The qubit plunger voltage pulses are realised by an HDAWG from Zurich Instruments. The microwave manipulation is done by controlling the in-phase (I) and quadrature (Q) channels of an SMW200A Rohde & Schwarz vector signal generator by two HDAWG outputs. Optionally, a Mini-Circuits Power Splitter ZMSCQ-2-90 can be used to control both the I and Q channels of the vector signal generator with a single HDAWG output, generating a single-sideband mixer output signal.

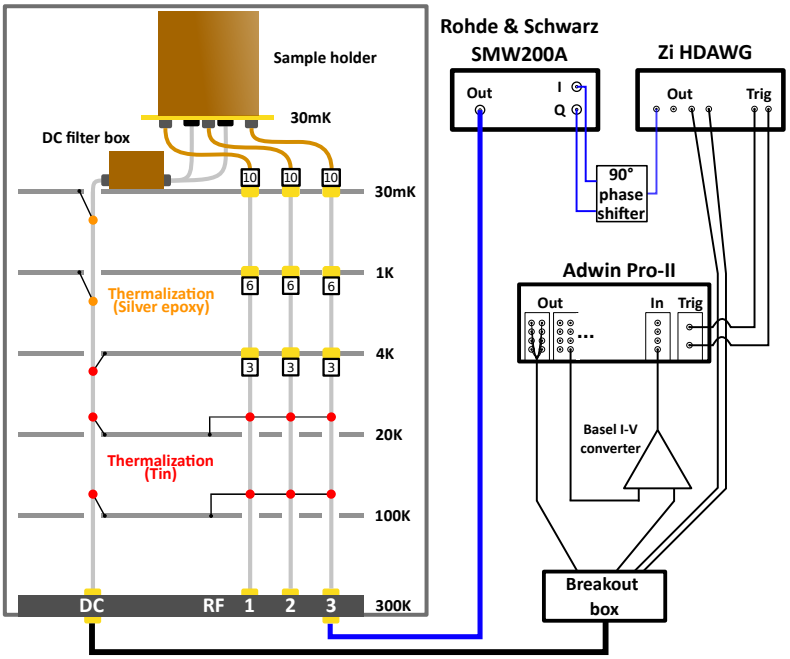

Figure 3.11.: Schematic of the combined measurement setup. On the left, the cryostat with built-in DC and RF lines. The small black-framed boxes represent attenuators, the number inside indicating the attenuation in dB. The orange/red circles represent thermalisation of the cables with silver epoxy/tin. Silver epoxy is used for temperatures below 3.72 K, where tin becomes superconducting and drastically less thermally conductive. Only 1 DC capillary and 3 RF lines are shown for clarity, but the cryostat is equipped with 4 such DC capillaries and 6 RF lines. On the right are the measurement electronics and their interconnections.

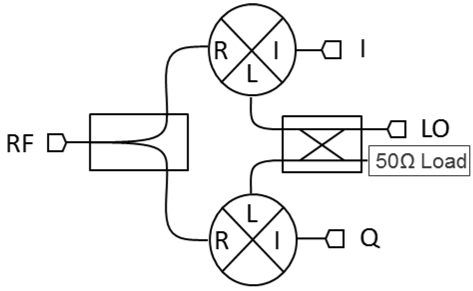

Figure 3.12.: Schematic of an IQ mixer, which consists of four components. From right to left: A hybrid quadrature coupler, two identical RF mixers, and an in-phase combiner. Taken from [146]

3.5. IQ mixing

IQ mixers, where "I" stands for in-phase and "Q" for quadrature, are four-port devices constructed from two identical mixers. A schematic representation is shown in Figure 3.12 and works as follows. A hybrid quadrature coupler is used to split the Local Oscillator (LO) signal into two signals that are 90 degrees phase shifted, which are then fed into two separate mixers. These mixers process the RF and LO signals (from the quadrature coupler) and perform the mixing. After the mixing, the in-phase combiner merges the signals from both mixers. For an example LO signal of $\cos(\omega_{\mathrm{LO}})$, the mathematical expression for the output signal of the IQ mixer is:

$$V_{RF}(t) = I(t) \cdot \cos(\omega_{\mathrm{LO}} t) - Q(t) \cdot \sin(\omega_{\mathrm{LO}} t). \tag{3.1}$$

Now assuming $I(t) = cos(\omega_{\mathrm{AWG}})$ and $Q(t) = 0$, and using the trigonometric identity $\cos(x) \cdot \cos(y) = \frac{1}{2}\left[\cos(x-y) + \cos(x+y)\right]$,

$$V_{RF}(t) = I(t) \cdot \cos(\omega_{\mathrm{LO}}) \tag{3.2}$$

$$= \frac{1}{2}\left[\cos(\omega_{\mathrm{LO}} + \omega_{\mathrm{AWG}}) + \cos(\omega_{\mathrm{LO}} - \omega_{\mathrm{AWG}})\right], \tag{3.3}$$

where the resulting signal has two equal sidebands at frequencies $\omega_{\mathrm{LO}} \pm \omega_{\mathrm{AWG}}$, similar to the behaviour of a single RF mixer.

However, for $I(t) = \cos(\omega_{\mathrm{AWG}})$ and $Q(t) = \sin(\omega_{\mathrm{AWG}})$, the output becomes:

$$V_{RF}(t) = \cos(\omega_{\mathrm{LO}} - \omega_{\mathrm{AWG}}). \tag{3.4}$$

In this case, one of the sidebands is canceled due to the two 90-degree phase shifts, which combine to create a 180-degree phase difference. The positive and negative versions of the signal cancel each other out, effectively suppressing one sideband and creating single-sideband (SSB) mixer behaviour.

In summary, an IQ mixer enables modulation of the amplitude, phase, and frequency of a high-frequency local oscillator signal, while control can be achieved using an arbitrary waveform generator (AWG) operating at MHz frequencies. This method provides maximum flexibility in shaping microwave pulses necessary for the universal qubit control pulses described in Section 6.4. For more information on IQ mixers, see [147].

4. Tuning of the Si/SiGe quantum dot device

This chapter describes how the quantum dots in the device are tuned to their operating points, which is the prerequisite for all subsequent qubit characterisation measurements. Starting from the first accumulation of the 2DEG to the formation of the sensor and qubit quantum dots, to gate lever arm estimation and charge sensing of the qubit double dot down to the single electron regime. Parts of this chapter are adapted from T. Koch et al. [139].

4.1. 2DEG accumulation in the Si/SiGe quantum well

The first step is accumulating a free electron gas in the desired regions while minimizing parasitic charged areas or unwanted electron tunnelling from the quantum well to the cap [110, 145]. This task can be particularly challenging in a Si/SiGe heterostructure, especially without prior knowledge of the average accumulation voltage. The accumulation voltage V_{acc} is defined as the voltage at which the electron density in the quantum well exceeds the critical electron density and a conductive channel is formed. However, applying too high voltages at the wrong gates can create unwanted charged regions that are often irreversible. If the gate voltages are lowered after the critical electron density has been exceeded once, some charges may remain trapped in the conduction band, since it is modulated by defects in the vicinity. These trapped charges can only be removed with additional thermal energy by heating the entire sample.

The gate architecture of the sample consists of three different gate layers. The purpose of the first gate layer differs fundamentally from that of the second and third gate layers. The first gate layer consists of screening gates that serve to divide the electron gas into two well-separated channels. It is

important to keep the screening gates well below the accumulation voltage ($\approx$ 100 mV below V_{acc}) in order to minimise the electron density under these gates. However, this requires knowledge of the rough accumulation voltage.

To measure V_{acc}, all voltages on all gates must be increased in parallel to form a large conductive area and reduce the effects of individual gate voltages or single defects on the measured current. The increased gate voltage will lower the conduction band of the quantum well until the electron ground state reaches the Fermi energy, at which electrons start to populate the conduction band energies. The electron density increases linearly with higher gate voltage [148, 149] and as soon as the critical electron density is reached, a sheet of mobile electrons have formed and a current becomes measurable. The first voltage at which a non-zero conductance/current is measured is defined as V_{acc}.

After V_{acc} is determined, the 2DEG has to be confined to the intended regions. For this, the CB and CT gate are lowered $\approx$ 100 mV below V_{acc}, and the CC gate is lowered $\approx$ 300 mV below V_{acc} to prevent leakage between the lower and upper current branches. Ideally the electron density below these gates is completely depleted, but usually some charges stay trapped in the modulated conduction band. These trapped charges can cause an unstable, less predictable behaviour of the charge environment and require additional thermal energy to be removed, as mentioned above. If a thermal cycle is performed, the measured accumulation voltage can be used as orientation for the fresh cool down. Now, there are two possible scenarios:

1. no thermal cycle was performed/necessary:

   The CB and CT gates are 100 mV below V_{acc}, the CC gate is 100 mV below V_{acc}, and all other gates are at V_{acc}. Usually, the previously measurable current is now depleted again because the screening gates block the source and drain current path and the current has to be accumulated again with the remaining gates. For this, the gate voltage at all gates except the screening gates are ramped up until a current becomes measurable again.

2. a thermal cycle was performed/necessary:

   All gates are back at zero and are first ramped up until 300 mV below V_{acc}. From here, all gates except the CC gate are ramped further until 100 mV below V_{acc}. In the next step, all gates except the screening gates are ramped up until a current becomes measurable.

The source drain current of the upper and lower channels are observed in parallel. As soon as one channel becomes conductive, the voltages responsible for this accumulation are kept constant, and only the gates for the other channel are further increased until accumulation. As an example: All gates except the screening gates are ramped up until a first current becomes measurable. Most of the time, the lower current path accumulates first due to the slightly larger gate pitch between the CB and CC gates compared to the CT and CC gates. A source-drain current in the lower channel is measured and the voltage increase is halted as soon as a the current reaches 1 nA. Now all gate voltages responsible for the lower channel accumulation (LBA, LB, ST, RB, RBA) are kept constant and only the gates for the upper channel (LTA, BL, PL, B, PR, BR, RTA) are increased further. If increasing the voltage of the upper channel gates also raises the current measured through the lower channel, the current can be reduced again by lowering the SET barrier gates. This will start to pinch the current in the SET region, preparing for the formation of the desired quantum dot for charge sensing. Further, it is important to keep source-drain currents below 10 nA to reduce the risk of damaging the sample due to strong local heating effects.

The dark blue regions in Figure 4.1**a** visualise where the 2DEG should now be accumulated and two independent current channels should be measurable. Figure 4.1 **b** shows an exemplary measurement of the source-drain current of the lower channel as the voltages at all gates, except the screening gates, are increased.

4.2. Formation of the quantum dots

Once both current channels have been accumulated, the next step is to form a quantum dot beneath the ST gate, which will later serve as a charge sensor. To achieve this, the barrier voltages of LB and RB are individually lowered to measure their respective "pinch-off" voltages, where each barrier gate suppresses the conducting channel. In an ideal device, these pinch-off voltages would be identical. However, due to local disorder and slightly misaligned gates, they can become asymmetric. Once both pinch-off voltages are approximately identified, a 2D gate map is performed, where the source-drain current is observed while varying the voltages at both barrier gates. Figure 4.2**b** shows an example of such a gate map. Starting from the upper right in the region of

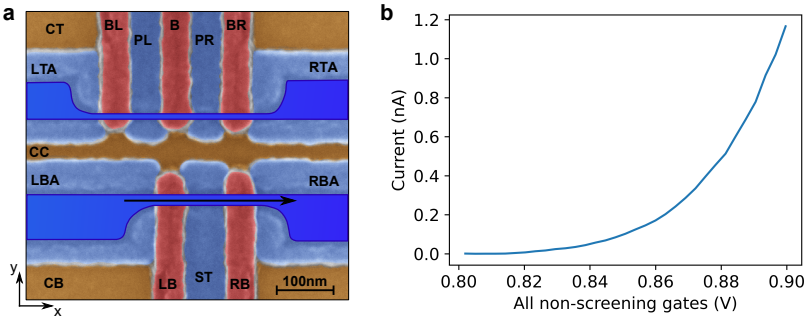

Figure 4.1.: a False coloured SEM picture of the device gate architecture. The dark blue regions indicate the regions where a 2DEG is accumulated. **b** Usual measured signature of the source-drain current when the gate voltages reach a regime in which the critical electron density of the quantum well is surpassed. All voltages except the three screening gates are increased. The upper and lower current channels are measured in parallel. The applied source-drain voltage is 1 mV, the CC gate is kept at 0.3 V, while CB and CT are kept at 0.49 V.

highest current, the current initially decreases as the barrier gate voltages are lowered. Reducing the barrier gate voltages raises the tunnel barrier height, slows down the electron tunnelling rate, and consequently lowers the measured current. As the barrier voltages are reduced further, the measured current begins to rise again. The voltage change at the barrier gates not only alters the tunnel barrier height but also affects the quantum dot energy level. When the quantum dot energy level is adjusted between the Fermi energies of the source and drain reservoirs, an electron can tunnel from source to drain through the quantum dot, leading to the increase in current visible for lower barrier voltages. So the reappearing current to lower gate voltages is a clear indication that a quantum dot has been formed. If the current does not reappear at lower gate voltages, the voltage at the ST gate is increased until the current is reaccumulated, and the barrier-barrier gate map is repeated. The quantum dot is formed as soon as Coulomb oscillations become visible, either as an oscillating current in the barrier gate map or directly measured by changing the ST gate voltage. The latter is shown in Figure 4.2**c** where the current is measured while increasing the ST gate voltage. Starting from zero current, the current increases and oscillates periodically as the quantum dot energy level is tuned between the source and drain Fermi energies of the reservoirs. The rising average current is due to cross-capacitive coupling

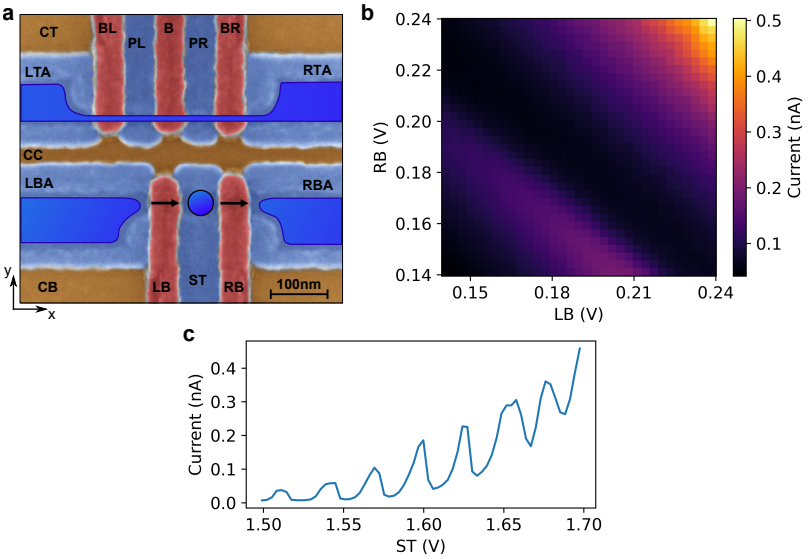

Figure 4.2.: a False coloured SEM picture of the device gate architecture. The dark blue regions indicate the regions where a 2DEG is accumulated. A quantum dot is formed below the ST gate and the black arrows indicate a source-drain tunnel current through the dot. **b** Measured tunnel current through the SET for different barrier voltages LB and RB. The visible Coulomb oscillations of the tunnel current in the gate map are caused by the cross-capacitive coupling of the barrier gates to the quantum dot energy level. The maximum SET current rises with higher barrier voltages due to an increase in the electron tunnelling rate. **c** Measured SET current for varying voltages at the plunger gate ST. Coulomb oscillations become visible.

from the plunger gate ST on the tunnel barrier heights, where an increased gate voltage lowers the tuned barrier height.

Analogously, the quantum dots are formed in the upper channel. If for example a quantum dot is to be formed below the PR gate, the cut-off voltages of the neighbouring barrier gates B and BR are measured, and a 2D barrier gate map is performed. If the gate map does not show any Coulomb oscillations, the voltage at the plunger gate PR is increased, and the previous steps are repeated until Coulomb oscillations become measurable.

4.3. Coulomb diamonds

As soon as a quantum dot is formed, it is important to characterise the lever arm of the plunger gate voltage on the quantum dot energy level. One way to determine this lever arm is to measure the tunnelling current through the quantum dot in dependence of the applied gate source-drain voltage and plunger gate voltage. This measurement is shown in Figure 4.3**a** for the formed quantum dot below the ST gate. Three distinct regions are visible. The red area indicates no tunnelling current, while yellow and black represent positive and negative current flow, respectively. The red regions form a diamond shape and indicate areas where Coulomb blockade is active, hence the term "Coulomb diamonds". The shape of the diamonds can be described using the constant interaction model (for a detailed discussion, see [150–153]). By determining the width and height of the diamond, the shift in quantum dot energy due to the plunger gate voltage can be mapped using the equation:

$$\alpha = \frac{0.5 \cdot \Delta V_{\mathrm{SD}}}{\Delta V_{\mathrm{ST}}}, \tag{4.1}$$

where ΔV_{SD} represents the total height of the diamond in voltage, and ΔV_{ST} represents the total plunger gate voltage required to span the width of the diamond. The width and height of the diamonds are determined by extrapolating the slopes of the diamonds at low source-drain bias voltages and identifying the voltages at the crossing points. This is illustrated in Figure 4.3**b**, where the blue lines extend the diamond edges to higher source-drain voltages, and the red points mark all the crossing points used to determine the diamond heights and widths. The extracted heights are listed in Table 4.1 and result in an averaged lever arm of $\overline{\alpha} = (0.086 \pm 0.014)$ eV/V.

Table 4.1.: SET lever arm estimation

	left diamond	**right diamond**
ΔV_{SD}	(5.0 ± 0.5) mV	(4.6 ± 0.5) mV
ΔV_{ST}	(28.3 ± 1.0) mV	(27.8 ± 1.0) mV
lever arm α	(0.089 ± 0.001) eV/V	(0.083 ± 0.001) eV/V

The same measurement is performed for the quantum dot formed under the PR gate and the tunnelling current in dependence of the source-drain voltage and PR gate voltage is shown in Figure 4.4. However, for this dot, the

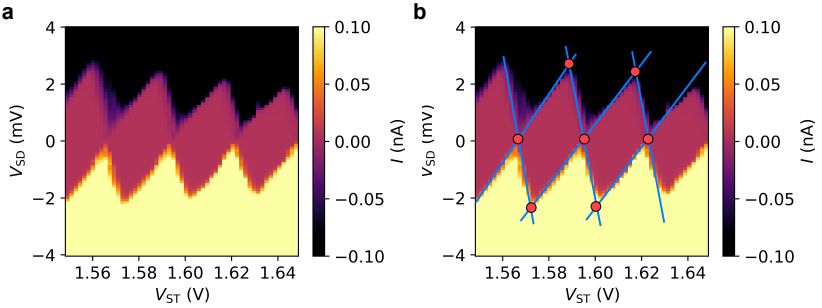

Figure 4.3.: a Measured tunnel current through the SET, formed under the ST gate, as a function of the source-drain voltage and the ST gate voltage. The colour bar is limited to absolute currents up to 0.1 nA to better distinguish the Coulomb blocked regions from those where current can flow. **b** The same data as in **a**, with added blue lines to extend the diamond edges to higher source-drain voltages, and red points to mark all the crossing points used to determine the plunger gate lever arm.

tunnelling barriers are strongly influenced by the PR gate voltage, altering the width and height of the Coulomb diamond. This is further illustrated by the extended diamond edges and crossing points depicted in Figure 4.4**b**. This makes it not possible to extract a reliable PR gate lever arm using this method. Therefore, another method is used which employs charge sensing.

4.4. Charge sensing

Due to its high susceptibility to the electrostatic environment, a quantum dot can be utilised as a tool for sensing neighbouring quantum dots and their electron occupancy. This enables the monitoring of quantum dots using much smaller tunnelling rates to the reservoirs, making it less challenging than probing the quantum dot through direct transport, which would require the ability to measure currents in the femtoampere range. Another significant advantage of using a charge sensor is its flexibility. The tunnelling current through a quantum dot performs Coulomb oscillations, which can often be tuned in width and height by altering the applied source-drain voltage or the tunnelling barrier heights. A dot with lower tunnelling barriers, operated at source-drain voltages above 1 mV, can have very wide and high Coulomb oscillations without any zero current windows. This allows for a large voltage

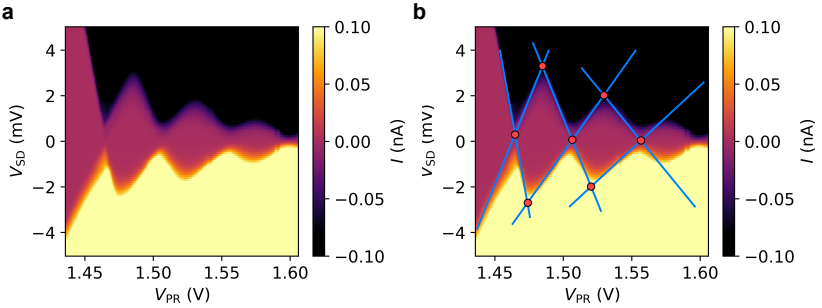

Figure 4.4.: **a** Measured tunnel current through the right qubit dot, formed under the PR gate, as a function of the source-drain voltage and the PR gate voltage. The colour bar is limited to absolute currents up to 0.1 nA to better distinguish the Coulomb blocked regions from those where current can flow. **b** The same data as in **a**, with added blue lines to extend the diamond edges to higher source-drain voltages, and red points to mark all the crossing points. The diamond shape changes drastically for different PR gate voltages due to strong cross-capacitive coupling on the tunnelling barriers, which makes it not possible to extract a reliable PR gate lever arm.

window for the working points, where the charge sensor remains sensitive to changes in the electrostatic environment, which is useful for extensive gate scans. Operating the charge sensor at low source-drain biases ($\approx 100\,\mu V$) and with higher tunnelling barriers often results in narrow and sharp oscillations. This is very useful for optimising the SNR when measuring the movement of single electrons. Figure 4.5**a** illustrates a typical measurement of a Coulomb oscillation in the SET with a source-drain bias of $400\,\mu V$. This measurement helps to find a suitable working point for charge sensing of the neighbouring qubit quantum dots. Here, a working point with a relatively high slope at the centre of the left flank is used, indicated by the red dot, to provide good sensitivity to external changes in the electrostatic environment. However, if the changes are too large, the working point will shift to a region with no tunnelling current and complete Coulomb blockade, where the SETs sensitivity drops to zero. The tunnelling current through the SET is now observed while sweeping the plunger gate voltage of the right qubit dot, as shown in Figure 4.5**b**. A sharp, discrete jump is observed at a plunger gate voltage of approximately 1.061 V, indicating a change in electron occupation in the close vicinity. The magnitude and sign of the jump amplitude can provide further information about the distance and whether an electron has moved closer to or away from the SET. However, both factors are directly

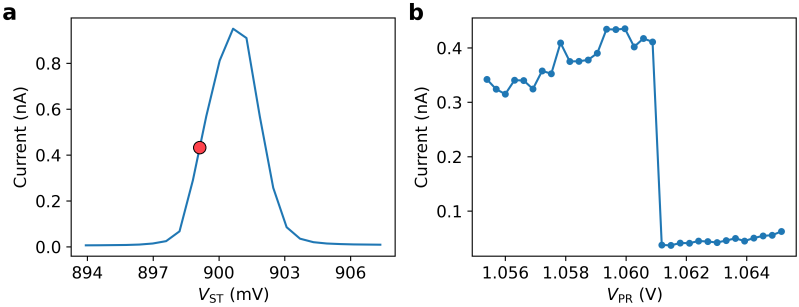

Figure 4.5.: a Measured Coulomb oscillation of the tunnelling current through the SET at an applied source-drain bias of 400 µV. The red dot indicates the working point used for the charge sensing measurement in **b**. **b** Measured SET tunnelling current while varying the voltage at the right qubit plunger gate PR. The tunnelling current performs a discrete jumps at a plunger gate voltage of approximately 1.061 V, indicating a change in electron occupancy of the quantum dot.

dependent on the chosen SET working point. An additional electron near the SET always lowers the electrostatic potential due to its negative charge. Consequently, the working point, such as the one chosen in Figure 4.5**a**, will shift to the left. This shift decreases the measured tunnelling current when using working points on the left flank and increases the tunnelling current when using working points on the right flank. Furthermore, the magnitude of the working point shift provides information about the distance to the location where the change in electron occupation occurred. This allows for distinguishing between changes in electron occupation in the right qubit quantum dot and the left qubit quantum dot, as the right qubit quantum dot is designed to be closer to the SET than the left qubit quantum dot.

For an electron jump to occur, the observed quantum dot must be coupled to an electron reservoir. In the case of the right qubit quantum dot, the reservoir is formed below the RTA gate and is connected to the upper drain voltage by an ohmic connection, which defines the chemical potential of the electron reservoir. The position of the measured electron jump in Figure 4.5**b** therefore also depends on the voltage applied to the reservoir. Tracking the position of the charge jump as the reservoir voltage changes provides another method to extract the lever arm of the plunger gate voltage on the quantum dot energy shift. Such a measurement of the SET tunnelling current, depending on the right qubit plunger gate voltage and the connected bias voltage, is

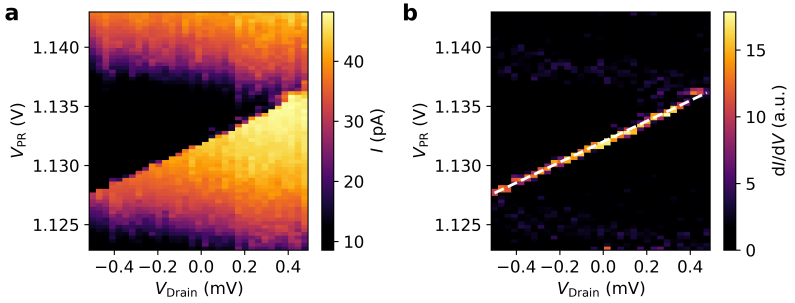

Figure 4.6.: **a** Measured SET tunnelling current in dependence of the qubit plunger gate voltage and the applied reservoir voltage. The gate map is in a plunger gate region showing the 0⟶1 electron transition of the qubit quantum dot. The visible sharp jump in the current indicates the voltage needed for the transition and shifts linearly with the applied reservoir bias voltage. **b** Numerical deviation of the tunnelling current map shown in **a**. The sharp jump now appears as a peak, which is linearly fitted and used to extract a plunger gate lever arm of (0.115 ± 0.002) eV/V.

demonstrated in Figure 4.6**a**. The plunger gate voltage at which the electron jump occurs shifts linearly with changing reservoir bias voltages. Figure 4.6**b** shows the numerical deviation for the same measurement, where the jump in the tunnelling current now appears as a sharp peak. These peak positions are used to extract the electron transition voltage over the reservoir bias. The slope of the linear fit of the peak positions yields a plunger gate lever arm of (0.115 ± 0.002) eV/V on the quantum dot energy.

There are three main advantages to using this method of lever arm extraction compared to the previously described method involving Coulomb diamonds. Firstly, when measuring Coulomb diamonds, the quantum dot source-drain is connected to DC lines to apply the voltage. When current is sent through the dot, the applied source-drain voltage at the quantum dot will depend on the inline resistance of the DC lines relative to the quantum dot resistance. When using charge sensing to extract the lever arm, no current flows through the sensed quantum dot, and the full voltage is applied to its reservoir. Secondly, when extracting the lever arm through Coulomb diamond measurements, it is necessary to separate the regions where Coulomb blockade is active from those where current is flowing. This is done by selecting a relatively arbitrary current threshold for the SET. For example, in Figure 4.3, a threshold current of 0.1 nA was chosen. Choosing a different threshold current can alter the

shape of the diamond and result in a different lever arm value. Additionally, the transition width from Coulomb blockade to non-blockade is highly electron temperature dependent, and elevated temperatures further reduce the precision of the extracted lever arm. Thirdly, when measuring Coulomb diamonds, the signal near zero source-drain bias is the weakest. Therefore, to accurately resolve the full diamond shape, it may be necessary to measure at relatively high bias voltages and sweep the plunger gate voltage over larger ranges. This can lead to other unwanted effects, such as altering the tunnelling barriers, changing the quantum dot size, or even causing heating due to high currents. Compared to the measurement shown in Figure 4.6, which uses a voltage window five times smaller and yields a lever arm with higher precision than the Coulomb Diamond method.

4.5. Electron temperature estimation

Charge sensing of the electron transition width of a neighbouring quantum dot also allows an estimate of the electron temperature of the coupled reservoir. Figure 4.7**a** schematically visualises the measurement principle. The Fermi level of the electron reservoir coupled to the quantum dot is thermally broadened, opening a window for electrons to tunnel in or out of the dot by thermal excitation. Depending on the exact position of the quantum dot energy in this window, the average electron occupancy of the quantum dot changes. This is measured capacitively by observing the tunnelling current through the adjacent charge sensor, which reflects the average electron occupation of the observed quantum dot, on the measured tunnelling current through the SET. The experimental implementation is shown Figure 4.7**b**, measuring the tunnelling current of the SET, while changing the voltage at the plunger gate PR of the right qubit dot in a small window of $< 2\,\mathrm{mV}$ around the $0 \rightarrow 1$ electron transition. The transition follows the Fermi-Dirac probability, and is fitted with

$$I_{\mathrm{SET}} = \frac{I_{\mathrm{A}}}{\exp\left(\frac{\alpha \cdot (V - V_0)}{k_B T_{\mathrm{e}}}\right) + 1} + I_{\mathrm{C}}, \tag{4.2}$$

where I_{A} and I_{C} are fitting parameters dependent on the SET working point, V_0 the centre of the transition, α the gate lever arm on the quantum dot energy extracted in Section 4.4, and the electron temperature $\mathrm{T_e}$.

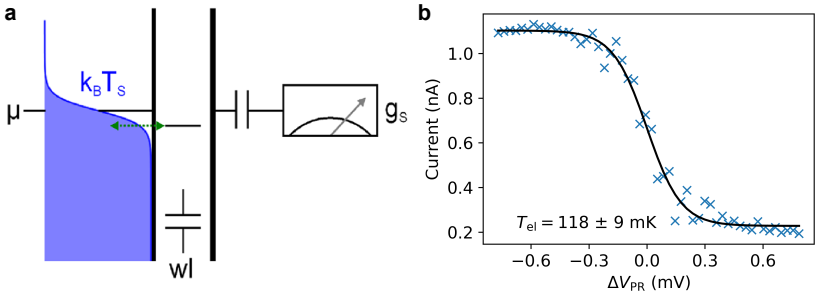

Figure 4.7.: a Schematic of the electron temperature measurement by charge sensing. The dot level is swept through the Fermi level at the chemical potential μ using the plunger gate voltage (shown here as wl). The average electron occupation, which reflects the Fermi–Dirac distribution (i.e. temperature T_S) of the electron reservoir, is probed by the current/conductance through a charge sensor that is capacitively coupled to the dot. Illustration taken from [154]. **b** Experimental implementation of the scheme in **a**, measured on the right qubit dot positioned under the gate PR, tracking the 0⟶1 electron transition. Each value of the tunnelling current is an average over 2 s, reflecting the average electron occupation of the observed dot. The transition is then fitted by a Fermi-Dirac distribution, resulting in an electron temperature of (118 ± 9) mK.

When performing this measurement, it is important to operate in a regime where the electron tunnelling rate to the reservoir, Γ, is small ($h\Gamma \ll k_BT$). This ensures that the transition broadening caused by the tunnelling rate is negligible and dominated by temperature broadening. For temperatures ≈ 100 mK, tunnelling rates below 1 MHz fulfill this condition well. This is another advantage of charge sensing compared to direct transport through a quantum dot, where tunnelling rates below 1 MHz correspond to tunnelling currents below 1 pA, making it very difficult to resolve the current at all. For further details see [154].

4.6. Charge noise measurements

Fluctuations in the electrostatic environment of quantum dots are referred to as charge noise. It has been shown that charge noise can significantly affect the coherence and fidelity of quantum operations, often becoming the limiting constraint on qubit coherence [47, 116, 118, 155–157]. Therefore, the magnitude of charge noise affecting the electrons in quantum dots is a crucial

parameter to characterise, and the semiconducting spin qubit community is continuously striving to minimise or eliminate sources of charge noise.

One way to measure charge noise is by performing current spectroscopy on the tunnelling current through a quantum dot. The entire procedure is illustrated in Figure 4.8 as an example for the right qubit dot. It has been demonstrated that charge noise can vary across different charge working points of the quantum dot [158, 159]. Therefore, the charge noise is measured for four different quantum dot working points, as shown in Figure 4.8**a**, and averaged. The first step is to measure the slope of the working point which allows a mapping of the current values to a plunger voltage measured in the later performed current spectroscopy. This is shown in Figure 4.8**b**, which shows a zoom-in on the working point in the centre of left flank of the Coulomb oscillation. In the next step, a long time trace is taken, where the tunnelling current measured for 5 min with a sampling rate of 10 kHz, shown in Figure 4.8**c**. The sampling rate is important because the upper frequency limit of the spectrum is set by the Nyquist frequency $f_{\mathrm{Ny}} = f_{\mathrm{s}}/2$, which is equal to half the sampling frequency f_{s} [160, 161]. For frequencies above the Nyquist limit, aliasing occurs. This causes higher frequency components of the signal to be indistinguishably mapped to lower frequencies, resulting in distortion and an inaccurate representation of the original signal. The lower boundary of the frequency spectrum is set by the measurement time T where only signals with a frequency of $1/T$ can be evaluated.

The timetrace is converted to a power spectral density using the Welch method [162]. Welch's method computes the power spectral density by dividing the timetrace into overlapping segments and averaging them. Additionally, a window function is applied to the individual segments. The use of the window function averages noise in the estimated power spectrum in exchange for a reduced frequency resolution because of overlapping time windows. A Hann function is used as the window function for the shown spectrum in Figure 4.8**d**. The resulting power spectral density is then normalized with the slope of the Coulomb oscillation at the used working point and converted to eV by multiplying with the plunger gate lever arm. The final power spectral density is then fitted with a a/f^b function and the value for 1 Hz is extracted. The 1 Hz charge noise values for each working point shown in Figure 4.8**a**, numbered from left to right, are listed in Table 4.2. The table also includes the charge noise values obtained using the same method for the quantum dot beneath the ST gate, which serves as the charge sensor.

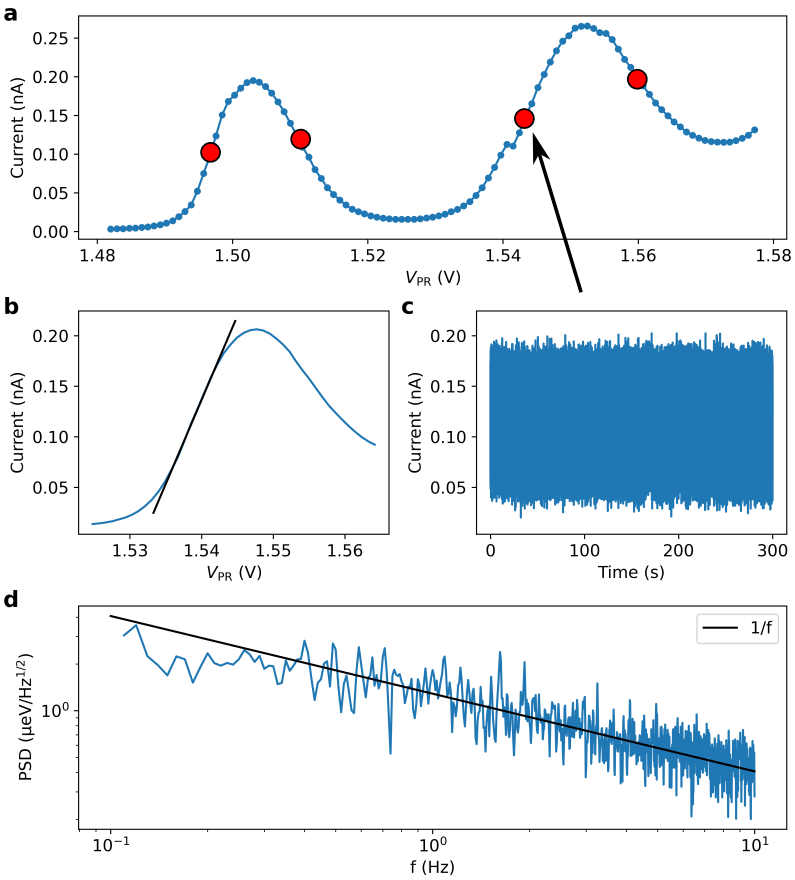

Figure 4.8.: **a** Coulomb oscillations of the right qubit dot, formed below gate PR. The red dots indicate the four positions used to extract charge noise values. The black arrow indicates the working point referenced in all subsequent measurements. **b** Zoom in on the working point and linear fit to the region around it. The fit corresponds to a slope of (16.6 ± 0.2) nA/V and is used to map the current noise to a voltage noise. **c** A 5 min time trace of the tunnelling current at the indicated working point, measured with a sampling rate of 10 kHz. **d** The calculated power spectral density from the time trace. For the indicated working point, a 1 Hz value of (1.43 ± 0.05) μeV/$\sqrt{\text{Hz}}$ is extracted, and the mean 1 Hz value of all four working points is (1.36 ± 0.07) μeV/$\sqrt{\text{Hz}}$.

Table 4.2.: 1 Hz charge noise values

Working point	right qubit dot ($\mu eV/\sqrt{Hz}$)	charge sensor ($\mu eV/\sqrt{Hz}$)
1	1.31 ± 0.06	1.80 ± 0.05
2	1.56 ± 0.08	1.72 ± 0.05
3	1.43 ± 0.05	2.86 ± 0.07
4	1.14 ± 0.07	0.82 ± 0.06
average	1.36 ± 0.07	2.30 ± 0.06

This noise characteristic is primarily attributed to the presence of fluctuating two-level systems (TLS) within the Si/SiO_2 interface [163–166]. These are defects or impurities that can switch between two states, causing fluctuations in the local electric field. The collective behavior of many such TLS, each switching at different frequencies, results in a noise spectrum that follows a $1/f$ distribution [113, 167, 168].

4.7. Tuning the double dot

When forming the double quantum dot in the upper channel of the device, it is generally easier to start with larger quantum dots and then tune them down to the single electron regime, rather than searching directly for the first electron occupation of the quantum dots. Starting from a conducting channel without any tunnelling barriers, the first step is to form individual quantum dots below each qubit plunger gate and measure the quantum dot in transport, as explained in Section 4.2. This will provide the respective voltages needed to form individual dots. Combining the voltages used for both individually formed quantum dots results in a lower overall electrostatic potential. This typically results in no measurable tunnelling current for direct transport measurements, as the reduced potential decreases the individual tunnelling rates, thereby reducing the tunnelling current. However, this provides a good starting point for employing charge sensing.

In transport measurements of quantum dots, it is challenging to determine the exact charge state of the dot. This difficulty arises because changing the plunger gate voltage not only changes the electron occupation, but also affects

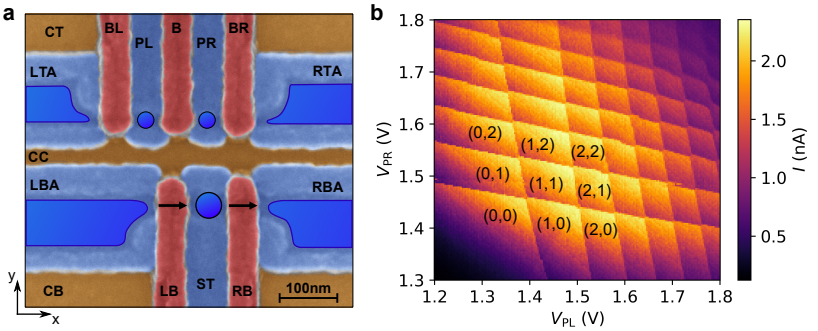

Figure 4.9.: **a** False coloured SEM picture of the device gate architecture. The dark blue regions indicate the regions where a 2DEG is accumulated. Two quantum dots are formed under the plunger gates PL and PR later used as qubit quantum dots and one larger dot below the ST gate. The large dot is measured in transport and used as an SET to perform charge sensing of the two qubit quantum dots. **b** Charge stability diagram of the two coupled qubit quantum dots, measured via charge sensing by the SET. Both qubit plunger gates are swept and every visible line corresponds to a change of electron number in the respective dots, starting with a (0,0) occupation in the lower left.

the tunnelling barriers, which in turn impacts the SNR of the measurement. Achieving a good SNR in direct transport measurements typically requires tunnelling rates in the GHz range (currents above 10 pA). Therefore, when looking for the regime where the quantum dot is fully depleted and lowering the plunger gate voltage, the barrier gates must also be compensated. Additionally, as the dot becomes smaller, the cross-capacitive coupling between the plunger gate and the barrier gate becomes stronger, further increasing the complexity of the measurement.

Using charge sensing to identify the charge occupation eases the issue of significantly changing SNR. This is because the sensors working point is much less affected by the qubit plunger gates and can be more easily compensated. Additionally, the charge sensor can be tuned to a regime that allows for larger changes in the external electrostatic environment while still remaining sensitive to electron jumps, as mentioned in Section 4.4.

Now while measuring the tunnelling current through the SET, a 2D gate voltage map is performed, sweeping the two qubit plunger gates PL and PR. The signature to look for are now sharp jumps in the measured current at relatively constant voltage spacing, each time indicating a change of electron

occupation in the respective dot. An exemplary measurement is shown in Figure 4.9**b** and is called a charge stability diagram. Over a large range of plunger voltages, sharp lines corresponding to a change of electron occupation are measured. The amplitude of the jump in tunnelling current and the slope of the line in the 2D map, are two indicators to distinguish between a change of electron occupation in the left or right qubit quantum dot. The left qubit quantum dot is slightly further from the SET, resulting in the amplitude of the jump being $\approx 30\,\%$ smaller compared to the right qubit quantum dot. The slope of the transition in the gate map is determined by the cross-capacitive coupling of the plunger gates on both qubit quantum dots. Therefore, a change in the voltage at the plunger gate PR will not only affect the right qubit quantum dot below it, but also the left one with a reduced magnitude. For further details on the exact shape of charge stability diagrams of double quantum dots see [150, 169].

To obtain information about the exact electron occupation of each dot, it is important to find the region where both qubit quantum dots are completely empty, the (0,0) charge state region. This is done by reducing the plunger gate voltage of both dots until no further jumps in the tunneling current occur, visible in the lower left region in Figure 4.9**b**. This gives now the orientation needed to have the full control of the charge state of both qubits.

5. Spin relaxation time and valley splitting energy

This chapter introduces the measurement method used to read out the spin state of the electron which is used in all coherent spin manipulation measurements in Chapter 6, and also used in this chapter to extract the spin relaxation time T_1 of the qubit. Further, two methods of extracting the valley splitting at the position of the qubit dots are introduced and performed, where the second method also probes the magnetic field dependence of the spin relaxation time. The valley splitting, particularly in Si/SiGe heterostructures, can be relatively low, and valley splittings close to the qubit Zeeman energy can cause hybridisation of quantum states. This hybridisation can significantly reduce spin relaxation times or interfering with the control of a distinct two-level quantum system [36, 127, 170]. This chapter is adapted in part from T. Koch et al. [139].

5.1. Second electron transition in magnetic field

One way to get a first estimation of the valley splitting is by investigating the 1→2 charge transition of a quantum dot. Figure 5.1**a** shows the Zeeman diagram of the two lowest valley states split by a finite energy E_{ST}, and the red line highlights ground state relevant for the second electron in the quantum dot. For increasing magnetic fields, the degenerate spin-up and spin-down states of each valley split up by the Zeeman energy. This results in the four distinct states $|\downarrow,-\rangle$, $|\uparrow,-\rangle$, $|\downarrow,+\rangle$, $|\uparrow,+\rangle$, where the arrow indicates the spin state and the ± denotes the valley state. For further increasing magnetic field, the splitting of $|\uparrow,-\rangle$ and $|\downarrow,+\rangle$ reduces until an external field value of B_{ST}, where the Zeeman energy equals the valley splitting energy E_{ST}. At this point the $|\uparrow,-\rangle$ state and $|\downarrow,+\rangle$ state hybridise and form an avoided level crossing. For higher magnetic fields, the $|\downarrow,+\rangle$ state becomes energetically

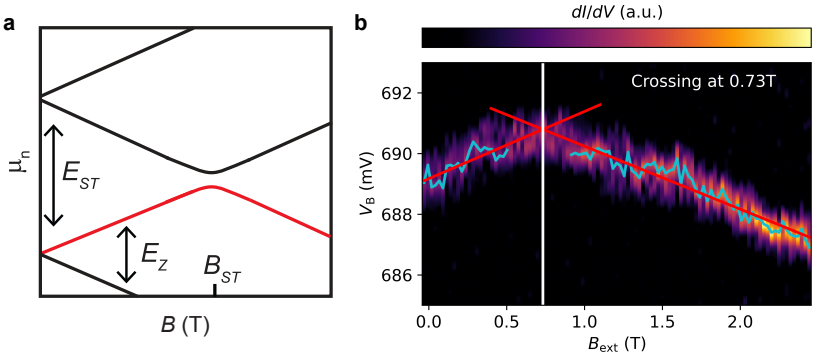

Figure 5.1.: **a** Zeeman diagram of the two lowest valley energy states $|\uparrow\downarrow,-\rangle$, $|\uparrow\downarrow,+\rangle$. The spin-up and spin-down energy states of both valley states split as the magnetic field increases. An avoided anticrossing occurs at an external field B_{ST}, where the Zeeman energy equals the valley splitting energy E_{ST}, and the $|\uparrow,-\rangle$ and $|\downarrow,+\rangle$ hybridise. When tracking the energy of the second electron in the quantum dot as a function of the magnetic field, highlighted by the red line, the slope changes its sign at B_{ST}, because the electron transitions from the $|\uparrow,-\rangle$ state to the $|\downarrow,+\rangle$ state. Adapted from [171]. **b** Numeric derivation of the charge sensor tunnelling current while scanning the voltage across the 1⟶2 charge transition of the right qubit quantum dot for external magnetic fields up to 2.5 T. The position of the 1⟶2 transition appears as a peak in the numeric derivation. The slope changes its sign over magnetic field. By linear fitting the positions from 0 to 0.5 T and 1 to 2.5 T separately and a crossing point at an external field of (0.73 ± 0.08) T is extracted, which converts to a valley splitting energy of (85 ± 9) µeV.

favourable, which the second electron will occupy, resulting in a change in slope compared to the previous state. So by tracking the voltage needed to for the second electron to occupy the quantum dot for different magnetic fields and identifying the external field B_{ST} and the change of slope, an estimate for the valley splitting can be extracted.

Figure 5.1**b** shows the numerical derivative of the sensor tunnelling current while sweeping the barrier gate B around 1⟶2 charge transition of the right qubit quantum dot, for external magnetic fields up to 2.5 T. The tunnelling current jumps sharply each time the electron occupation changes, which is shown as a peak in the numerical derivative. By tracking the peak over magnetic field, the Zeeman diagram shown in Figure 5.1**a** can be measured. In this measurement, the barrier gate B is used instead of the plunger PR, to intentionally reduce the lever arm on the quantum dot energy. The barrier gate B has an ≈ 3.4 times smaller lever arm on the dot energy, because being further away laterally and also vertically because the gate belongs to the third

gate layer in comparison to the plunger belonging to the second layer. And because quantum dot is coupled to the reservoir via the barrier gate BR, the effect of gate B is also minimal on the relevant tunneling barrier.

The measurement is performed by ramping to the maximum external field value of 2.5 T and ramping down, in order to make sure the Co micromagnet is fully saturated and does not influence the measurement by additional contributions during its magnetisation (more details regarding the micromagnet will be discussed in Section 6.3). The peak position of the 1→2 shows a similar behaviour shown in by the red line in Figure 5.1**a**. B_{ST} is extracted by fitting the peak positions from 0 to 0.5 T and 1 to 2.5 T separately, where the slope is not affected by the hybridisation of the $|\uparrow,-\rangle$ and $|\downarrow,+\rangle$ states. By extrapolating both slopes to the point where they cross a B_{ST} of (0.73 ± 0.08) T can be extracted. At this point the Zeeman energy is equal the valley splitting energy, and assuming an electron g-factor of ≈ 2, this corresponds to a valley splitting energy $E_{\mathrm{ST}} = (85 \pm 9)$ μeV.

5.2. Spin-selective readout

In Section 4.7, the full control of the charge states of the qubit dots was established. The next step is the readout of the electron spin state in the quantum dots. For this, the spin-selective readout scheme first demonstrated by Elzerman et al. [172] can be used. By applying an external magnetic field, the degenerate spin states of the electrons are splitted by the Zeeman energy. It is important that the Zeeman energy $2\mu_0 B_{\mathrm{ext}} \gg k_{\mathrm{B}}T$, in order to have two distinct and well defined electron states. Given an electron temperature of ≈ 100 mK corresponds to a thermal energy of 8.6 μeV, so external fields above 150 mT should be aimed for as a minimum, to have at least twice the Zeeman energy splitting.

The quantum dot energies relative to the coupled reservoir level during the stages of the Elzerman pulse scheme are illustrated in Figure 5.2**a**. The pulse scheme consists of three different stages:

1. Emptying the dot by pulsing the quantum dot energies of both spin states high above the Fermi energy of the coupled electron reservoir.
2. Loading the quantum dot by pulsing the dot levels deep below the Fermi energy of the reservoir, so both spin states are addressable by

electrons from the reservoir. But only one of the two spin states can be occupied at a time, because the charging energy necessary to load a second electron prevents the occupation of both states at the same time.

3. Spin-selective read out of the quantum dot by pulsing the dot levels to a point where the Fermi energy of the reservoir lies in between the spin-up and spin-down energy states of the quantum dot. Here two different scenarios appear depending on the spin state of the loaded electron. If the electron is in the spin-up state, it will tunnel out of the quantum dot, into the reservoir, and a new electron will occupy the spin-down state of the quantum dot. And if the electron is initially in the spin-down state, nothing will happen during this period of time.

Figure 5.2**b** illustrates the voltage pulse at the quantum dot plunger gate and Figure 5.2**c** shows an exemplary response of the charge sensor during the different stages. During the empty phase of the pulse, the lowest voltage is applied at the plunger gate, and current through the charge sensor stays constant because the electron occupation does not change. In the second stage, the plunger gate is pulsed to the most positive voltage during the pulse, in order to pulse the quantum dot levels deep below the reservoir level. The change of plunger voltage is also visible in the response of the charge sensor, because of cross capacitive coupling of the plunger gate voltage to the energy level of the charge sensor. Additionally, the charge sensor shows a jump in the measured current after some waiting time, which is caused by an electron tunnelling into the quantum dot. The time scale on which this tunnelling event happens on average, can be tuned by the tunnelling rate of the quantum dot to the electron reservoir.

In the third stage, the readout stage, the plunger gate voltage is pulsed to a level where the reservoir level is in between the spin-up and spin-down energy levels of the quantum dot. The charge sensor shows here a different response depending on the spin-state of the electron in the dot. For an electron in the spin-down state, no tunnelling event happens and the tunnelling current of the charge sensor stays constant. But if the electron is in the spin-up state, it will tunnel out of the quantum dot, causing a first jump in the sensor current, and after some time a new electron will tunnel back into the quantum dot, occupy the spin-down state, and the sensor current will jump back to its previous level. The time scales of these events are again dependent on the tunnelling rate of the dot to the reservoir. The pulse scheme ends again at

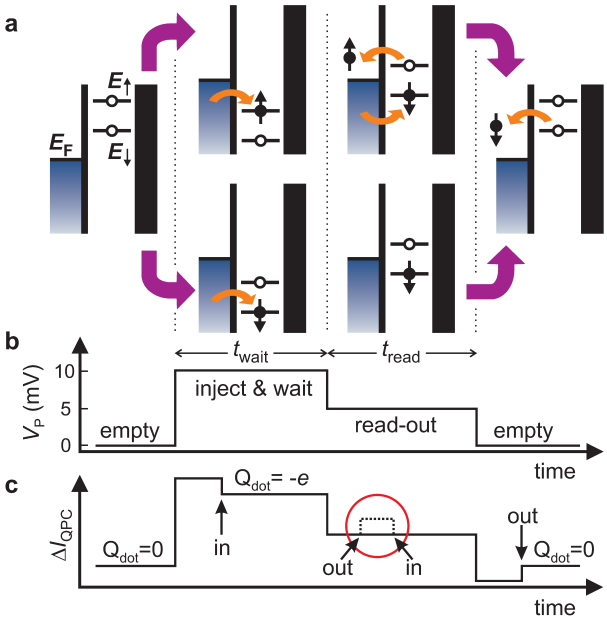

Figure 5.2.: Schematic illustration of the spin-selective readout. Adapted from [172]. **a** Illustration of the quantum dot energies relative to the reservoir level during the stages of the pulse. A constant external magnetic field is applied, which Zeeman splits the electron spin-up and spin-down states. In the first stage of the pulse, the dot is emptied, by making sure the energies of both spin states are above the Fermi energy of the reservoir. In the second stage, the quantum dot energy is pulsed deep below the reservoir level, which allows the occupation of either the spin-up or spin-down state. At the same time, if one of the spin states is occupied, the needed charging energy prevents a second electron to occupy the other spin state. In the third stage, the quantum dot energy is pulsed to a point where the Fermi energy of the reservoir is between the spin-up and spin-down energies of the electron. During this stage, spin-selective tunnelling occurs: if an electron is in the spin-up state, it tunnels out of the quantum dot, allowing a new electron to tunnel in, while if the electron is initially in the spin-down state, no change occurs. Afterwards, the quantum dot is emptied again, recreating the scenario of stage one. **b** Schematic quantum dot plunger gate voltage over time for the 3 different stages of the pulse. **c** Schematic tunnelling current response of the charge sensor. The timescales of the electron tunnelling events measured by the charge sensor strongly depend on the electron tunnelling rate to the reservoir and can be tuned over a wide range by changing the barrier gate voltage.

its start by pulsing back a voltage, which completely empties the dot, which can also be seen in the charge sensor current. The sign of the responses of the charge sensor depends on the chosen working point, or more specific which flank of the Coulomb oscillation is chosen. The responses shown in Figure 5.2**c** are typical for a working point on the left flank of the Coulomb oscillation, and responses would be inverse for a working point on the right flank.

5.3. Blip evaluation

The signature of an spin-up electron in the charge sensor signal during the spin-selective readout, is described as a "blip". Figure 5.3**a** shows two exemplary measurements of the tunnelling current for an electron in the spin-down state (blue) and an electron in the spin-up state (orange). The in case of the spin-up electron, the tunnelling current performs two sharp jumps in time, the first one when the electron tunnels out of the dot, and the second one, as soon as a new electron occupies the spin-down state of the dot. During the readout phase of the Elzerman pulse, the average lifetime, and therefore the blip length, of the spin-up state is determined by the tunnelling rate between the quantum dot and the reservoir. This tunnelling rate is tuned to $\approx 1\,\mathrm{kHz}$ which results in an average blip length of 1 ms. The tunnelling current of the sensor is converted to a voltage and amplified by an I-V converter with a used gain of 10^9 which at the same time has a 3 dB frequency cutoff at $\approx 2\,\mathrm{kHz}$, which gives a lower limit for a blip length, to be detectable at all. Therefore, much faster tunnelling rates than $\approx 1\,\mathrm{kHz}$ will result in more and more result in a signal loss. On the other hand, slower tunnelling rates, will increase the time window over which the sensor current has to be observed, and therefore increases the total measurement time of the experiments. So the chosen tunnelling rate of 1 kHz is a trade-off between good SNR and a faster measurement time.

To make efficient use of the spin-selective readout, a single shot measurement is not sufficient and a reliable statistic of the spin-up fraction generated from multiple single shot measurements is required. Figure 5.3**b** shows the raw data of an exemplary measurement, where 200 single shot measurements were performed and the response of the charge sensor was measured. In the first step, the sign of the current jump is corrected, in order to have always

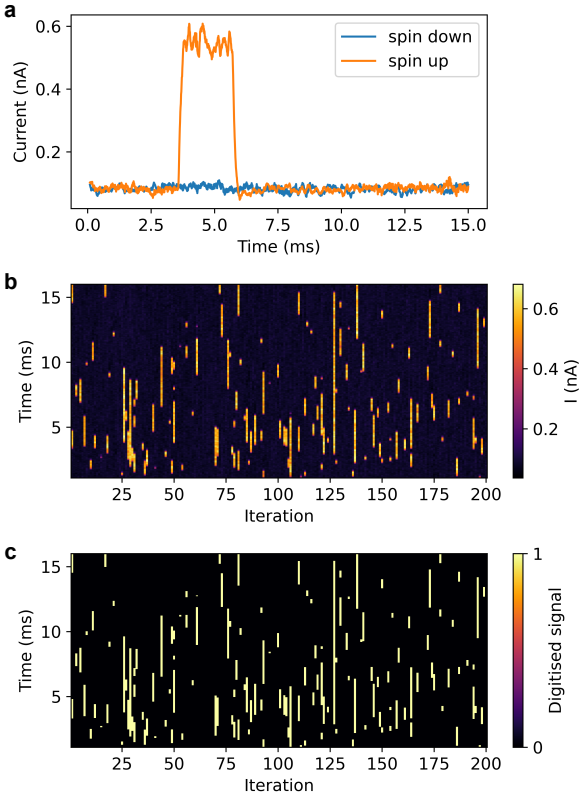

Figure 5.3.: a Exemplary measurement of the sensor current during the readout stage of the Elzerman pulse. Blue shows the response of the sensor current for an electron in the spin-down state, and orange for an electron in the spin-up state. The signature in the spin-up trace is referred to as a "blip". The tunnelling rate of the quantum dot to the electron reservoir is tuned to $\approx 1\,\mathrm{kHz}$, which determines the average length of the blips. **b** Raw measurement data of 200 single shot measurements, before data treatment. **c** Data processing, consisting of sign correction, smoothing, baseline correction and digitisation by a fixed threshold, results in the digitised signal of the raw data. This digitised signal is used to count the number of traces containing tunnelling events and dividing by the total number of traces to yield a spin-up fraction of 57 %.

positive current jumps for an electron tunnelling out of the dot. This is needed because the sign of the current jump depends on the working point of the charge sensor.

In the second step, the each trace is smoothed by a Savitzky-Golay filter in order to lower the effects of high frequency noise, but at the same time lowers the ability to resolve very short blips. So the strength of the filtering in this step strongly depends on the SNR of the jump in the charge sensor and its noise baseline. For the SNR shown in Figure 5.3**a** and **b**, only slight filtering is needed if any at all.

In the third step, the baseline of each trace is corrected by subtracting the measured current by the minimum value for in each trace, in order to unify the conditions for the final step.

In the fourth and final step, each sample of each waveform is digitised into either a 0 or a 1 by filtering through a fixed threshold, where 0 corresponds to current values where an electron occupies the quantum dot and 1 corresponds to no electron in the dot. Figure 5.3**c** shows the result of the digitising algorithm.

The spin-up fraction is now determined by counting all traces in which at least one tunnelling event occoured, i.e. all traces containing at least one digital 1, and then dividing the number of traces with tunnel event by the total number of traces. For the illustrated measurement, the resulting spin-up fraction is therefore 57 %.

In the ideal case, each trace either contains no blips, or one blip at maximum. But because of a finite temperature, the thermal energy of the electrons create additional thermal blips, where electrons which are already in the ground state, tunnel out of the dot, and a new electron tunnels into the dot. These thermal events have the exact same current signature in the charge sensor and can not be distinguished from spin-up events. The only difference is the occurrence over time between the thermal events and the spin-up events. Thermal events are equally distributed over time, while the spin-up events are more likely to happen as soon as the quantum dot is pulsed to the readout voltage. Therefore, the spin-up events are clustered at the start of the measurement and exponentially less likely to happen the longer the readout voltage is kept.

5.4. Spin relaxation time

The Elzerman pulse scheme, explained in detail in Section 5.2, can now be used to measure the spin relaxation time T_1 of a single electron in the qubit quantum dots. The first step is to find the plunger gate voltage needed where the reservoir level is between the spin-up and spin-down state of the quantum dot. This is done by performing the Elzerman pulse and varying the voltage level during the readout window. Figure 5.4**a** shows the pulse shape applied at the plunger gate PR on top of a constant DC bias. The coloured region is a 15 ms window, in which the tunnelling current through the SET is measured. The black arrow shows the voltage plateau value, which is varied over the measurement. Figure 5.4**b** shows the measured SET current during the time windows shown in Figure 5.4**a**, where the plunger readout voltage is varied from -4 to 4 mV. For the first 2.5 ms the pulse is still in the loading stage, and an electron in either the spin-up or spin-down state occupies the dot. The x-axis displays the voltage to which the plunger gate jumps in the time window between 2.5 and 12.5 ms, and the area from 12.5 ms onwards, shows the start of the empty stage of the pulse scheme. The bright regions correspond to a higher SET current through the charge sensor, corresponding to currents where the quantum dot is not occupied by an electron, and in the darker regions of lower SET current, an electron occupies the dot. So for voltages below $\Delta V_{\mathrm{PR}} \approx -1.2\,\mathrm{mV}$ the electron is always pushed out of the dot, while for voltages above $\approx -0.8\,\mathrm{mV}$ the electron will stay in the dot until the later empty stage of the pulse. The circle in Figure 5.4**b** highlights the region of interest. In the region between -1.2 and $-0.8\,\mathrm{mV}$ the SET response depends on the electron spin state and the blip events from spin-up electrons are clustered close to the point in time after jumping to the readout voltage. This clustering creates the region of higher SET current, which decays over time, which is called "spin tail", because it is caused by the electrons in the exited spin-up state. The voltage width of the spin tail is directly dependent on the Zeeman energy divided by the gate lever arm, and the length in time depends on the tunnelling rate of the electron reservoir to the quantum dot. The plunger gate voltage for which the spin tail becomes visible can now be used for all further measurements where the spin state of the electron is needed to be read out.

One important property of the electron spin is the spin relaxation time T_1, which describes the average time for the excited spin-up state to relax into the spin-down ground state, and therefore describes the average life time

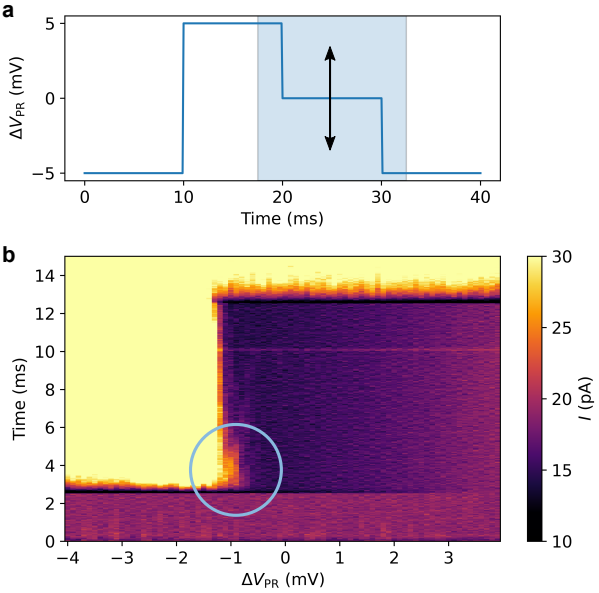

Figure 5.4.: **a** Voltage over time added to an applied DC bias at the right qubit plunger gate PR, used to perform the Elzerman pulse scheme. The blue coloured window shows the region in which the SET current is measured. The pulse scheme is performed for varying voltage levels during the readout window, as indicated by the black arrow. **b** Measured SET current for the pulse scheme in **a**, used to find the readout voltage for the spin-selective readout. A total magnetic field of 660 mT was applied. The bright regions indicate the area where no electron occupies the quantum dot, and the dark regions show the tunneling current when the dot is occupied. The region of interest is highlighted by the circle, in which the bright region extends further into the dark then elsewhere. This feature is caused by the clustering of blips caused by spin-up electrons tunneling out of the quantum dot and a new electron occupying the spin-down ground state, and indicates the region where the spin-selective readout can be performed.

of the spin. Because the qubit information is planned to be encoded into this spin-up and spin-down state, the T_1 time gives an upper limit for the calculation length, one can perform on the given qubit.

The spin relaxation time T_1 can be measured by varying the time of the second stage of the Elzerman pulse, the loading stage. When changing the duration of the loading stage, the electron has the chance to relax from its exited spin-up state into its spin-down ground state. Therefore, for longer duration of this stage of the pulse, exponentially more electrons in the ground state will be

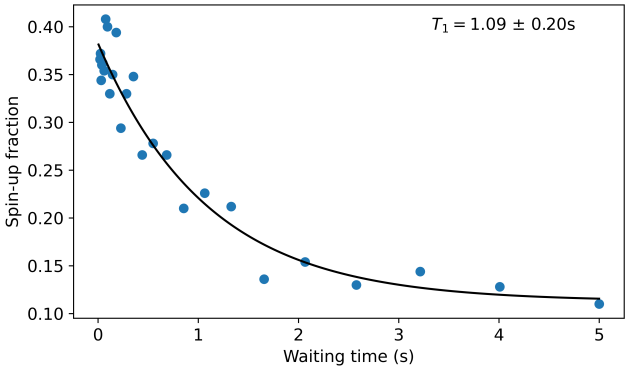

Figure 5.5.: Spin-up fraction for different waiting times during the loading pulse of the Elzerman pulse scheme. Each point corresponds to the fraction of traces, containing a blip from a total of 500 single shot measurements. An exponential decay is fitted to the data, resulting in a spin relaxation time of $T_1 = (1.09 \pm 0.20)$ s. The measurement was performed at an external field of 660 mT.

measured, with T_1 being the characteristic time of this exponential behaviour. Figure 5.5 shows the measured spin-up fraction for different durations of the loading stage. The black curve is a fit of the function $A \cdot \exp(t/T_1) + C$ and yields a spin relaxation time of $T_1 = (1.09 \pm 0.20)$ s. The offset in the spin-up fraction results from the amount of thermal events in the readout windows, and strongly depend on the exact readout voltage. The closer spin-down level of the quantum dot is to the Fermi level of the reservoir, the more thermal events will occour. However, because thermal events are evenly distributed over time, they will shift the baseline of the measurement but will not affect the exponential decay of spin-up events over the waiting time. When using the Elzerman pulse scheme, pulsing the quantum dot deep below the reservoir level will result in equal probabilities of loading the spin-up and spin-down states in an ideal scenario. This gives a maximum theoretical visibility of 50 %, defined as the difference between the highest and lowest values of the spin-up fraction.

The measurement depicted in Figure 5.5 was conducted at an external magnetic field of 660 mT. This field strength is later used for spin manipulations and qubit characterisation. However, the T_1 time is highly dependent on

the applied external magnetic field, which will be elaborated upon in the following section.

5.5. Magnetic field dependence of the spin relaxation time

Investigating the magnetic field dependence can not only give insights about the different noise contributions, leading to the spin relaxation process, but can give also a measure of the valley splitting energy. Figure 5.6 shows the measured spin relaxation rate $1/T_1$ for external magnetic fields of up to 2.5 T. The data across the entire magnetic field range is fitted using a rate equation that combines spin-valley (SV) and spin-orbit (SO) coupling, accounting for both Johnson noise (J) and phonon noise (ph) [170, 173, 174]:

$$\Gamma_{\mathrm{tot}}(B) = \Gamma_{\mathrm{SO}}^{\mathrm{ph}}(B) + \Gamma_{\mathrm{SO}}^{\mathrm{J}}(B) + \Gamma_{\mathrm{SV}}^{\mathrm{ph}}(B) + \Gamma_{\mathrm{SV}}^{\mathrm{J}}(B), \tag{5.1}$$

with the four individual terms:

$$\Gamma_{\mathrm{SO}}^{\mathrm{ph}}(B) = \Gamma_{0,\mathrm{SO}}^{\mathrm{ph}} \cdot \left(\frac{g\mu_{\mathrm{B}}B}{E_{\mathrm{VS}}}\right)^5 \cdot (1 + 2\,\langle n(E_{\mathrm{z}})\rangle), \tag{5.2}$$

$$\Gamma_{\mathrm{SO}}^{\mathrm{J}}(B) = \Gamma_{0,\mathrm{SO}}^{\mathrm{J}} \cdot \left(\frac{g\mu_{\mathrm{B}}B}{E_{\mathrm{VS}}}\right) \cdot (1 + 2\,\langle n(E_{\mathrm{z}})\rangle), \tag{5.3}$$

$$\Gamma_{\mathrm{SV}}^{\mathrm{ph}}(B) = \Gamma_{0,\mathrm{SV}}^{\mathrm{ph}} \cdot \left(\frac{g\mu_{\mathrm{B}}B}{E_{\mathrm{VS}}}\right)^5 \cdot (1 - |a(E_{\mathrm{z}})|), \tag{5.4}$$

$$\Gamma_{\mathrm{SV}}^{\mathrm{J}}(B) = \Gamma_{0,\mathrm{SV}}^{\mathrm{J}} \cdot \left(\frac{g\mu_{\mathrm{B}}B}{E_{\mathrm{VS}}}\right) \cdot (1 - |a(E_{\mathrm{z}})|), \tag{5.5}$$

$$\tag{5.6}$$

the Bose-Einstein distribution function $\langle n(E_{\mathrm{z}})\rangle = \left(\exp\left(\frac{g\mu_{\mathrm{B}}B}{k_{\mathrm{B}}T}\right) - 1\right)^{-1}$, and

$$a(E_{\mathrm{z}}) = \frac{-(E_{\mathrm{VS}} - E_{\mathrm{z}})}{\sqrt{(E_{\mathrm{VS}} - E_{\mathrm{z}})^2 + \Delta^2}}. \tag{5.7}$$

The rate equation diverges where the valley splitting energy E_{VS} is equal to the Zeeman Energy E_{z}, yielding a valley splitting energy of (87.9 ± 0.5) µeV.

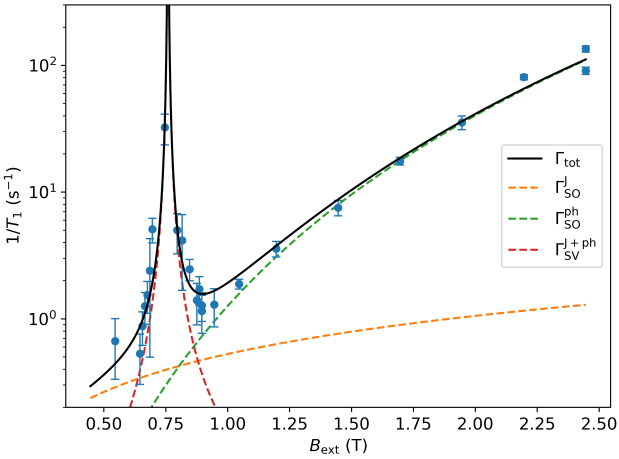

Figure 5.6.: The spin relaxation rate $1/T_1$ for external magnetic fields up to 2.5 T. The black curve represents a fit that combines spin-orbit and spin-valley coupling, incorporating both Johnson noise and spin-phonon interactions. The individual contributions to this fit are shown by the red, green, and yellow dashed lines. The fit diverges at an external field of (759 ± 4) mT resulting in a valley splitting of (87.9 ± 0.5) µeV.

For external magnetic fields above 1.5 T, the spin relaxation rate is primarily governed by phonon-mediated spin-orbit coupling, resulting in a B^5 dependence of the spin relaxation rate, although different dependencies have also been observed [175, 176].

The valley splitting extracted using this method, also known as the "hotspot" measurement, is consistent with the value obtained in Section 5.1, with both corresponding to frequencies above 20 GHz. In Chapter 6, qubit manipulations are primarily conducted at a resonance frequency of 18.5 GHz or lower, ensuring that there is no influence from the higher valley state.

However, it has been shown that the valley splitting energy can vary significantly depending on the precise spatial location of the quantum dot [82, 170], due to inhomogeneities in the Si/SiGe interface. This effect would be valuable to investigate further in the devices used in this thesis. Additionally, fluctuations in the Ge concentration near the Si quantum well can also alter the valley splitting [177, 178], and some proposals suggest that this could even be used advantageously [179, 180].

6. Coherent spin manipulation

This chapter begins by explaining the fundamentals of electric dipole spin resonance, which is used to manipulate the spin for qubit operations. It then outlines the experimental procedure required to identify the optimal qubit working points, including qubit frequency and the magnetisation of the cobalt micro-magnet. Finally, the chapter presents a comprehensive qubit characterisation, covering driving speed and power dependence, coherence times, and the gate fidelity assessed through randomised benchmarking. All measurements presented in this chapter were performed on the right qubit located below the PR gate on the same sample, with the ID "D09 Die5 SD15B". Any references to a qubit in this chapter refer to the right qubit quantum dot on this chip. Measurements involving different chips and qubits are shown in the Appendix A.1. Parts of this chapter are adapted from T. Koch et al. [139].

6.1. Electric dipole spin resonance

The most common way to control an electron's spin is through electron spin resonance (ESR), where the spin is resonantly coupled to an external alternating magnetic field, causing a spin transition. For single electrons in quantum dots, this is achieved by applying an external magnetic field that aligns the spin in the direction of the field, splitting the spin-up and spin-down states due to the Zeeman energy. By applying an alternating magnetic field perpendicular to the aligned spin direction, at a frequency matching the Larmor frequency, a spin transition can be actively induced.

This can be experimentally achieved by fabricating a microwave drive line, such as a coplanar waveguide, near the quantum dot, allowing the spin of the quantum dot to couple with the oscillating magnetic field generated by the waveguide [50, 108, 138, 181]. This is often done for quantum dots

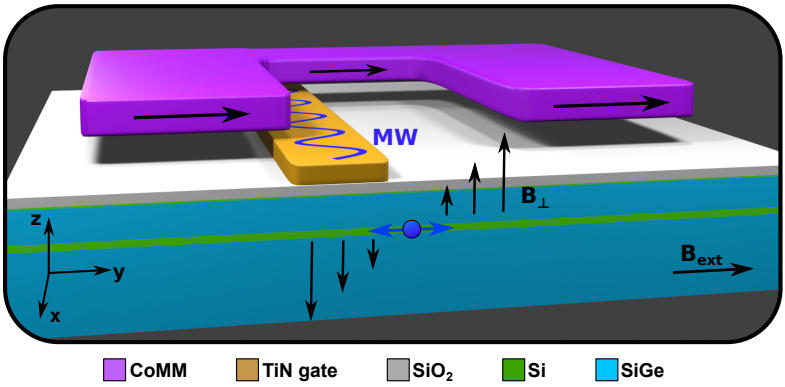

Figure 6.1.: Illustration of the electric dipole spin resonance principle of the device. An external magnetic field applied along the y-axis magnetises the Co micromagnet in the same direction. The qubit quantum dot is formed in the silicon quantum well, approximately 120 nm below the centre of the 300 nm gap in the Co micromagnet. The micromagnet generates an inhomogeneous magnetic field within the plane of the Si quantum well. The CC gate is pulsed with a microwave signal, causing spatial oscillations of the quantum dot in the inhomogeneous magnetic field. The perpendicular component of the field gradient effectively creates a driving amplitude at the same frequency as the microwave signal applied to the CC gate. When this is in resonance with the electron's Larmor frequency, a spin transition can be induced.

in Si-MOS structures, as the quantum dots are located close to the surface, allowing for strong coupling to the drive lines. For Si/SiGe heterostructures, however, the quantum dots are located in a quantum well buried several tens of nanometres below the surface. As a result, the coupling strength to the drive line is significantly reduced, since the amplitude of the magnetic field generated by the drive line is proportional to the distance r to the drive line. Here, the method of electric dipole spin resonance (EDSR) can be useful [181–183].

The principle of EDSR is illustrated in Figure 6.1. An external magnetic field applied along the y-direction aligns the electron spin in the same direction and also magnetises the C-shaped cobalt micromagnet along the y-axis. The quantum dot, which hosts the electron, is formed in the gap of the micromagnet. The stray magnetic field from the micromagnet generates an inhomogeneous magnetic field around the quantum dot. A microwave pulse is then applied to a gate near the quantum dot, causing the electron to couple with the electric field from the gate. The oscillating electric field induces movement of the

electron's position at the same frequency as the microwave pulse. As the electron oscillates around its initial position and is located in an inhomogeneous magnetic field, these spatial oscillations are directly converted into an oscillating magnetic field. The amplitude of the drive now depends on the gradient of the magnetic field's perpendicular component relative to the spin alignment, as well as the magnitude of the spatial oscillations. Simultaneously, magnetic field gradients along the y-direction will cause shifts in the Larmor frequency, leading to additional dephasing.

The Co micromagnet geometry was simulated and optimised in [142] in order to maximise the coupling strength, while minimising the spin dephasing caused by the micromagnet field gradient. There, the optimisation was done for isotopically purified Si^{28} quantum wells, where the spin coherence is usually longer and not as limited by fluctuating nuclear spins of the Si^{29} isotopes in natural Si. Therefore a 600 nm gap was predicted to perform the best in those devices. In the later sections of this chapter, the presented measurements feature a Co micromagnet with a gap size of 300 nm. CoMM gap sizes of 400 and 650 nm were also investigated regarding the qubit performance and are listed in Appendix A.1.

6.2. Finding the resonance

A non-trivial task that must be accomplished before any active spin manipulation measurements can be performed is determining the Larmor frequency of the qubit. Since the influence of the magnetised Co micromagnet can only be roughly estimated through simulations, an uncertainty of approximately 50 mT results in an uncertainty of around 1.4 GHz in the Larmor frequency. Given that the resonance width is below 1 MHz, finding the resonance by scanning the microwave frequency step by step would take several days of measurement time to cover the full range.

An elegant method that significantly simplifies the search for the spin transition frequency is rapid adiabatic passage [184–186]. Rapid adiabatic passage is a method commonly practised in nuclear magnetic resonance (NMR) experiments, and uses pulses with gradually changing frequency (chirps) instead of pulses at constant frequency. Figure 6.2**a** illustrates a schematic energy diagram in the spin-up and spin-down basis, as a function of frequency detuning from the resonance frequency. The microwave excitation produces

an oscillating (effective) magnetic field in the equatorial plane of the Bloch sphere. In the rotating frame, which is synchronised with the instantaneous excitation frequency, the driving field aligns along a fixed axis B_1 (shown in the insets of Figure 6.2**a**). When the microwave frequency is detuned from the spin's Larmor frequency by $\Delta\omega$, the electron experiences an additional effective magnetic field $\hbar\Delta\omega/g\mu_B$, perpendicular to the equatorial plane of the Bloch sphere. Figure 6.2**b** illustrates the effect of the rapid adiabatic passage chirp on the trajectory of the vector on the Bloch sphere. As the microwave frequency is swept from far below to far above the resonance frequency, the total effective field B_{eff} gets inverted. The electron spin will follow B_{eff} and will also be inverted, provided that the frequency sweep satisfies the adiabatic condition [187]

$$\frac{\mathrm{d}f}{\mathrm{d}t} \ll f_{\text{Rabi}}^2, \tag{6.1}$$

with the chirping rate $\frac{\mathrm{d}f}{\mathrm{d}t}$, and the Rabi frequency f_{Rabi}. The probability for the electron to be excited is given by the Landau-Zener formula [188]

$$P_{\text{up}}(\dot{f}) = 1 - \exp\left(-\frac{\pi^2 f_{\text{Rabi}}^2}{\dot{f}}\right). \tag{6.2}$$

In addition, the total chirp duration must be shorter than the spin relaxation time T_1, otherwise the spin-up state will decay again before readout. This condition is easily met in this case, as the spin relaxation times are on the order of seconds, as shown in Sections 5.4 and 5.5.

Before performing the rapid adiabatic passage measurement, it is necessary to first estimate the microwave power required to induce any electron excitation. In Section 3.4, the transmission of the RF lines up to the sample holder is characterised. However, the sample itself is connected via wire bonds, and the transmission starting from the wire bonds to the CC gate, and along the CC gate to the precise location of the quantum dots, is unknown and can only be estimated.

A method to get a first orientation for the power is to apply a continous microwave signal at the drive line and increase the power until a heating effect becomes visible. The inner conductor of the attenuator at the mK stage is thermally connected to the RF line on the sample PCB. As a result, any heat generated in the attenuator as a signal passes through it can have an effect on sample. Further, the dielectric losses directly on the sample chip

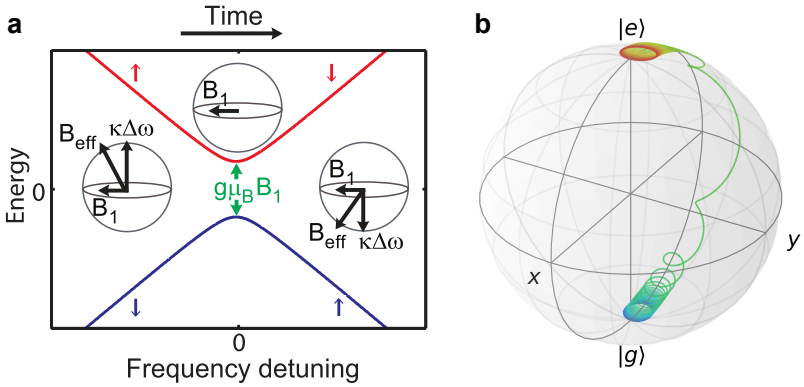

Figure 6.2.: a Schematic illustration of the rapid adiabatic passage. The blue and red solid lines represent the electron spin eigenenergies in the presence of an AC excitation, which is perpendicular to the static magnetic field, as a function of detuning from the resonance frequency. The excitation frequency is gradually varied (chirped) in the direction indicated by the time arrow. The insets depict the effective magnetic field acting on the spin at three different detuning values, with $\kappa = \hbar/(g\mu_B)$. Adapted from [184]. **b** Exemplary Bloch sphere trajectory of a rapid adiabatic passage sweep. Adapted from [185].

can also cause direct heating of the sample hosting the quantum dots. This heating can be observed by monitoring the width and height of a quantum dot Coulomb oscillation at low source-drain bias. This measurement is shown in Figure 6.3**a**, where the SET plunger gate (ST) is scanned within a voltage window around a single Coulomb oscillation at a bias voltage of 60 µV, while the CW microwave power applied at the CC gate is gradually increased. For applied powers below −5 dBm, a sharp peak is measured and no effect of the power is visible. For powers above −5 dBm, the peak thermally broadens more and more to increasing power. A first power value for the rapid adiabatic passage chirp would now be the maximum power where no or only a slight thermal broadening sets it, which would be a power somewhere between −5 and 0 dBm for the measurement shown in Figure 6.3**a**. The shown behaviour was measured for a constant microwave frequency of 17.37 GHz, but as mentioned before, can change heavily for different frequencies.

The thermal broadening for frequencies between 16.5 and 20 GHz at a constant power of 23 dBm is shown in Figure 6.3**b**. For frequencies between 18.4 and 20 GHz, the thermal broadening effect is relatively small compared to

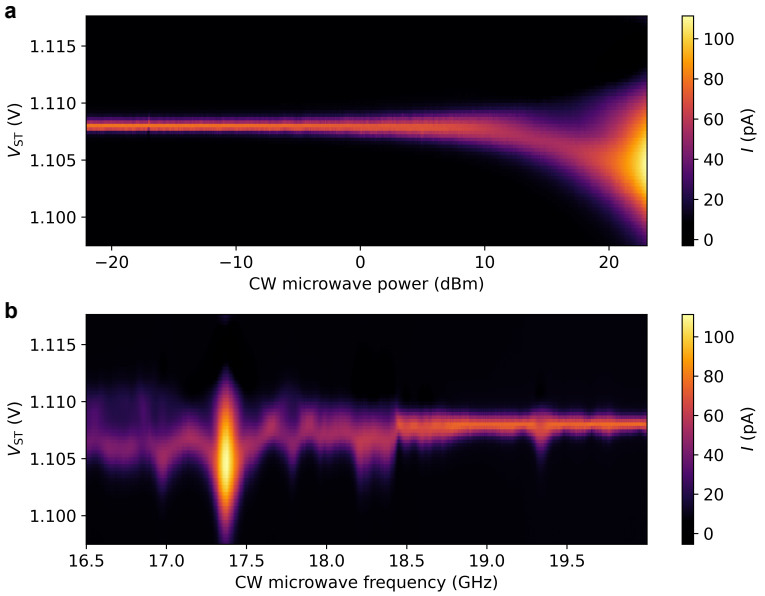

Figure 6.3.: Measured SET tunneling current while sweeping the voltage at the plunger gate (ST) within a small window around a Coulomb oscillation, with a continuous microwave signal applied to the central screening gate (CC), used for later qubit manipulation. **a** A constant frequency of 17.37 GHz is applied, and the power is increased from −22 to 23 dBm. **b** Frequency sweep of the continuous microwave signal at an applied power of 23 dBm.

frequencies below 18.4 GHz, where it is approximately 10 dB higher when compared with the power behavior shown in Figure 6.3**a**. Additionally, a strong resonance is observed at 17.37 GHz. However, the thermal broadening cannot be directly used as a measure of the power that reaches the qubit and can be used to drive it. The thermal broadening reflects the total dissipated power affecting the entire sample, which only correlates to the transmitted power if the system's losses remain constant across frequencies. This is not necessarily the case, and the actual power that reaches the qubit can only be measured directly when the qubit is manipulated, by determining the qubit drive speed for a given power at different frequencies.

With a rough estimate of the power, the search for the electron resonance frequency can begin. Figure 6.4**a** shows the voltage pulse used to load an

electron into the ground state in the quantum dot, pulse the quantum dot level deep below the reservoir level for manipulation, and then jump to a readout voltage level to perform spin-selective readout. The voltage pulse at the qubit plunger gate PR is shown in blue, and the time window in which data is collected for analysis of the blip events is highlighted by the light blue area. The orange line shows the trigger signal, which gives the start time of the microwave chirp.

The pulse shape applied to the qubit plunger is a shortened version of the Elzerman pulse, combining the readout pulse with a modified loading pulse. The loading stage of the pulse features a voltage slope designed to improve the initialisation fidelity of the electron in the spin-down state while enhancing the working point's robustness against fluctuations in the electrostatic environment. This concept is inspired by the ramped measurement technique demonstrated in [189], where the voltage during the readout window is gradually increased, allowing the spin-up and spin-down states to be distinguished by the timing of the observed blip. When operating the dot energy at the readout point, the amount of thermal events is highly sensitive to the applied plunger voltage, making it also vulnerable to electrostatic fluctuations in the environment. Additionally, the thermal events are evenly distributed over time, resulting in a finite probability that the dot may not be occupied by an electron at any given moment, as the electron could have tunnelled out due to thermal energy. When pulsing deep below the reservoir for electron manipulation and the dot is unoccupied, this creates the possibility of loading an excited-state electron into the dot. Therefore, by gradually lowering the quantum dot energy further below the reservoir until the probability of a thermal event drops to zero, the risk of an unoccupied quantum dot pulsing to the manipulation level is eliminated, preventing the parasitic loading of an electron in an excited state.

Figure 6.4**b** illustrates an exemplary waveform of a frequency chirp, which is sent from the AWG output into an I-Q mixer. This signal is then mixed with the microwave signal from the vector source, which in this case is set to a constant frequency of 17.4 GHz. The frequency is gradually increased over time which creates a frequency chirp at the frequency of the local oscillator (LO) ± the mixing frequency (explained in more detail in Section 3.5). The illustrated waveform is not the actual chirp used in the experiment, but has slower frequencies and a shorter time window for better visibility. The pulse used for the experiment shown in Figure 6.4**c**, chirps the frequency from 100 to 120 MHz over a time period of 4 ms.

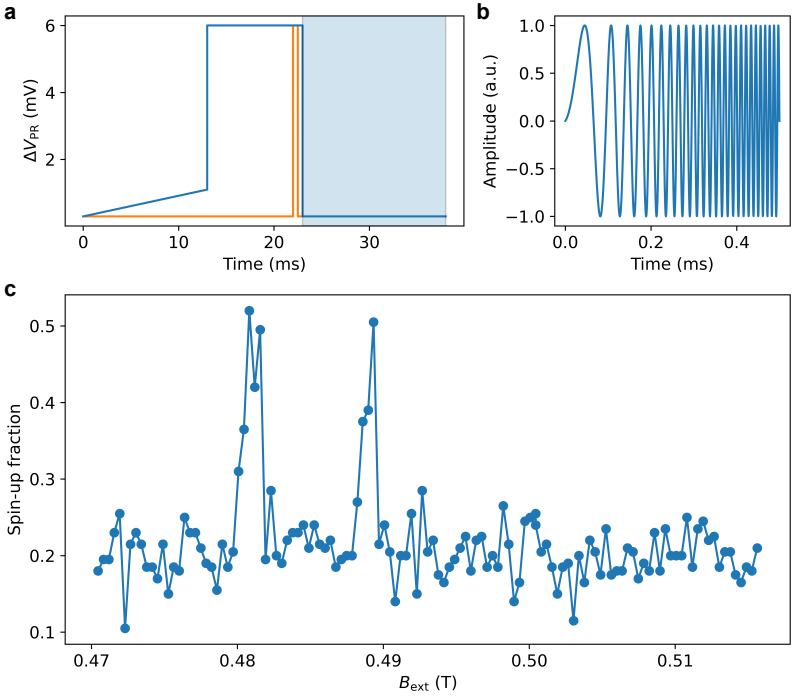

Figure 6.4.: **a** The voltage pulse applied to the qubit plunger gate PR, used to load an electron and perform spin-selective readout, is shown in blue. The trigger signal for the microwave chirp timing is shown in orange, and the blue-shaded region marks where the SET current is measured. **b** A frequency chirp is applied when the orange trigger signal in **a** rises. The length and frequencies have been adjusted for better visibility, illustrating the continuous increase in the frequency pulse over time. **c** The spin-up fraction of the qubit dot is measured during the rapid adiabatic passage experiment as the external magnetic field strength is reduced. Double sideband mixing is used, with the microwave source set to a center frequency of 17.4 GHz, mixed with a 100-120 MHz frequency chirp. As the external field is decreased, the qubit resonance frequency is lowered, and when it aligns with a sideband of the frequency chirp, an increase in the spin-up fraction is observed.

Figure 6.4**c** shows the result of the performed rapid adiabatic passage measurement. Each point represents the spin-up fraction of the electron in the quantum dot, determined from the blip events extracted from 200 single-shot measurements. The vector source is set to a frequency of 17.4 GHz with an output power of 5 dBm. The measurement is performed while gradually

reducing the external magnetic field, which lowers the Zeeman energy of the quantum dot and therefore the resonance frequency of the spin transition. Similarly, the frequency of the microwave source could be swept while applying a constant external magnetic field. However, as shown in Figure 6.3**b**, the power driving the qubit can vary significantly across different frequencies. Therefore, it is typically easier to sweep the electron resonance frequency through the frequency chirp of the microwave source by adjusting the external magnetic field.

The displayed magnetic field range of 50 mT covers a frequency window of ≈ 1.4 GHz. As soon as the electron resonance frequency enters the frequency chirp of one of the sidebands of the mixed RF signal, the spin-up fraction rises sharply. The spacing between the two peaks in the spin-up fraction is determined by the lower boundary of the chirp of 100 MHz, resulting in a gap of 200 MHz (≈ 8 mT). The width of the peaks is set by the 20 MHz chirp window, corresponding to a peak width of around 1 mT. In summary, the right peak corresponds to the external field where the electron resonance frequency lies between 17.5 and 17.52 GHz, while the left peak corresponds to the external field where the resonance frequency falls between 17.28 and 17.3 GHz. Another advantage of the frequency chirps of the rapid adiabatic passage method, is that the adiabatic inversion is independent of the exact resonance frequency. This makes it resilient to slow fluctuations in the resonance frequency, as the noise affecting the electron resonance frequency is much smaller than the available frequency chirp windows.

The result of the rapid adiabatic passage narrows the frequency window to be scanned to find the electron resonance frequency from the GHz range to 20 MHz, making it feasible to scan with a standard frequency sweep. Such a frequency scan is shown in Figure 6.5, for an externally applied field of 532 mT, later used for all coherent spin manipulations. The measurement uses the same plunger gate pulse as in Figure 6.4**a** but mixes a 0.5 ms long pulse at constant frequency. The frequency pulse should be long compared to the estimated coherence time of the qubit, so the spin is completely dephased, leading ideally to a 50 % spin-up fraction of the electron spin. The measurement is performed for different microwave output powers, and it is visible that the measurement performed at a power of 0 dBm shows a higher and broader peak compared to the measurement performed with a power of -20 dBm. While the measurement at higher power, eases the determination of the exact qubit resonance frequency, because of better SNR and a larger peak width, the peak where no power broadening occurs can be used to

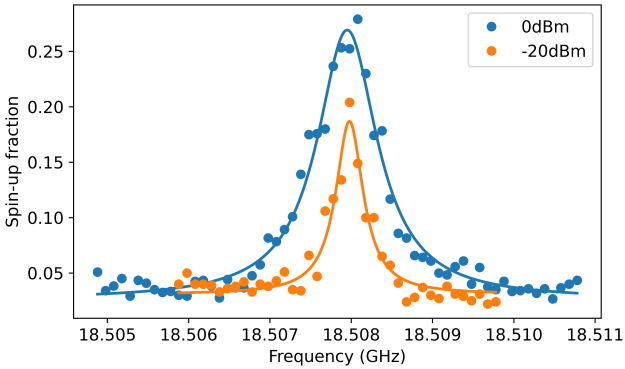

Figure 6.5.: Spin-up fraction of the electron in the qubit quantum dot over different frequencies of the applied microwave pulse, for an applied external magnetic field of 532 mT. The sweep is performed for a microwave output power of 0 dBm (blue) and −20 dBm (orange). The lines correspond to lorentian fits of the spin-up fraction. The data of the spin-up fractions are fitted by a lorentian curve

extract a first estimate of the spin coherence time T_2^*. To lower microwave powers, the peak narrows until the line width is limited by the qubit lifetime. The shape of the curve is after all a result of multiple excitation pulses and averaging, and the noise on the resonance frequency is reflected by this on the width of the resonance curve. Fitting the peak in the low power limit with a lorentian function and extracting the full width half maximum (FWHM) of the peak, an estimation for T_2^* can be obtained by following the equation [150, 190]:

$$T_2^* = \frac{2\sqrt{\ln 2}}{\pi \cdot \mathrm{FWHM}} = (1.29 \pm 0.12)\,\mu\mathrm{s}. \tag{6.3}$$

This value is very similar to other reported values for the spin coherence time T_2^* in natural silicon [109, 191–194]. Performing the frequency scans for even lower microwave powers, does not narrow the line width further, and only decreases the SNR further.

6.3. Cobalt micromagnet magnetisation

As mentioned in the previous section, the behaviour of the Co micromagnet (CoMM) on the qubits until now could only be approximated based on simulations and estimations. But with the possibility of measuring the exact resonance frequency of the qubit, the micromagnet can be characterised with higher precision. The CoMM featured on the qubit chip, used for all the coherent spin manipulation measurements demonstrated in this chapter, posesses a 300 nm gap, and the two qubit quantum dots are positioned in its centre, aproximately 120 nm below the micromagnet. Qubit measurements on chips with the same gate architecture, but different CoMM gap sizes are shown in Appendix A.1.

By applying an external magnetic field in the y-direction with the superconducting coils, the ferromagnetic CoMM becomes magnetised. The extent of this magnetisation and the external field required to fully magnetise the micromagnet can be determined by measuring the qubit resonance frequency across a wide range of frequencies. Figure 6.6**a** shows the measured resonance frequency of the qubit as a function of the applied external magnetic field in y-direction. The field is always ramped to the maximum field value first, in order to make sure the CoMM is fully saturated. The used vector source limits the maximum measurable frequency to 20 GHz. The resonance frequencies are narrowed down to a precision of 10 MHz determined by the resolution of the rapid adiabatic passage measurements used to determine the resonance frequencies. The two branches for positive and negative fields are measured independently. For the positive branch, the field was first ramped up to 1 T, then reduced to the values used to extract the resonance frequencies, down to 0 external field. The negative branch was measured similarly by ramping to an external field of −1 T, then returning to 0 field. At high external magnetic fields, the CoMM is expected to be fully saturated, providing a constant magnetic field contribution in the direction of the externally applied field. This increases the Zeeman splitting of the qubit, thereby raising its resonance frequency. A linear fit of the electron resonance frequencies between 15 and 20 GHz is used to determine the contribution of the CoMM field in saturation. This yields a field of (129.0 ± 1.8) mT for the resonance frequencies measured at positive external magnetic fields, and (129.3 ± 1.3) mT for the frequencies at negative external fields. From simulations, a magnetic field offset of approximately 120 mT was predicted, which is very close to the measured value. Further, a perpendicular magnetic field gradient of 1.2 mT/nm at the qubit

position is predicted by the simulation, which will be relevant for the later qubit manipulations.

In Figure 6.6**b**, the measured resonance frequencies for externally applied magnetic fields between 0.2 and 0.6 T are displayed for two magnetic field sweep directions. The blue data corresponds to that shown in Figure 6.6**a**, where the resonance frequencies were measured while sweeping downwards from high magnetic fields. In contrast, the orange data represents the measured resonance frequencies for the same externally applied magnetic fields, but starting from a negative external field of −1 T, sweeping down to zero, and then upwards to the positive field values. The black line represents the same fit of the resonance frequencies above 15 GHz, as shown in Figure 6.6**a**. For external fields below 0.3 T, resonance frequencies deviate from the linear behaviour observed at higher external fields. Additionally, the extracted qubit resonance frequencies vary depending on the magnetic field sweep direction. The inset provides a zoomed-in view of the lowest measured resonance frequencies, where the deviation is most pronounced.

Figure 6.6**c** shows the difference in qubit resonance frequencies between the upward and downward sweep direction of the external magnetic field for the data shown in Figure 6.6**b**. For external fields of 0.2 T, a resonance frequency difference of ≈ 200 MHz is measured, which converges to zero for externally applied magnetic fields above 0.45 T.

The deviation of the qubit resonance frequencies from the linear behaviour observed at higher fields is attributed to a decreasing magnetisation of the CoMM. Additionally, the resonance frequencies deviation for different magnetic field sweep directions further hint at a regime where the cobalt is no longer fully magnetised and follows a hysteretic magnetisation curve characteristic of a ferromagnetic material. The maximum resonance frequency difference of ≈ 200 MHz between the up and down magnetic field sweep directions corresponds to a magnetic field difference of ≈ 8 mT, which is only about 6 % of the CoMM field at full saturation. This leads to the hypothesis that the majority of the ferromagnetic hysteresis behaviour is yet to occur for externally applied magnetic fields below 0.2 T. However, it was not possible to resolve any qubit resonance frequencies below 8 GHz, and the exact reason for this remains unclear.

The coherent spin manipulation measurements presented from Section 6.4 to the end of Chapter 6 were performed using an RF line that is not galvanically connected to the driving gate CC. Instead, the RF signal is coupled capacitively

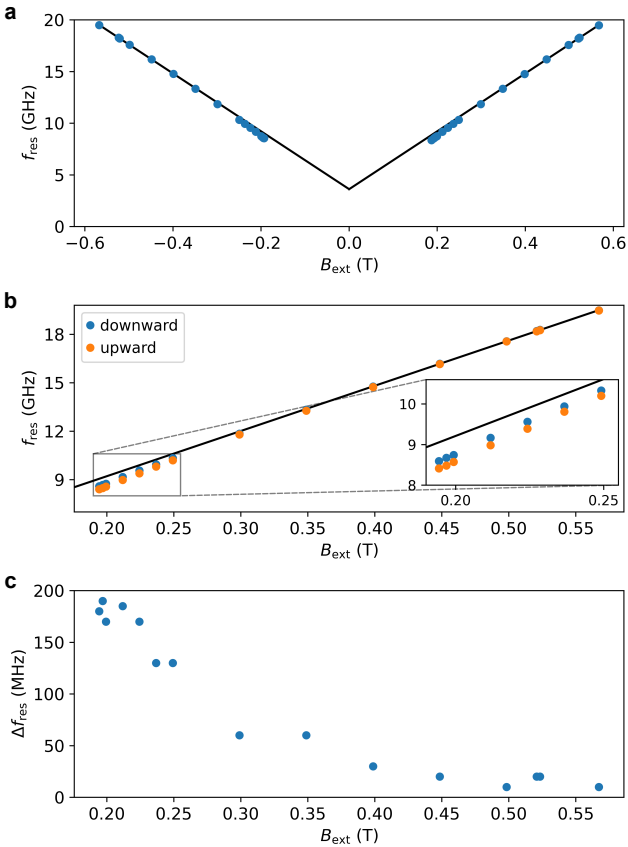

Figure 6.6.: **a** Resonance frequency the qubit as a function of the applied external magnetic field in y-direction. The frequencies are extracted starting from the maximum external field and decreasing to zero. The two branches for positive and negative fields are measured independently. The black lines correspond to a linear fit of all resonance frequencies between 15 and 20 GHz. The contribution of the CoMM field in saturation is extracted from the y-offset of the linear fit and yields a field of (129 ± 2) mT. **b** Zoom on the positive magnetic field branch shown in **a**, to which qubit resonance frequencies extracted from an upward magnetic field sweep have been added. For external magnetic field values below 0.3 T, a deviation from the linear behaviour is visible. In addition, the extracted qubit resonance frequencies deviate depending on the magnetic field sweep direction and chronology. The inset shows a zoom of the lowest measured resonance frequencies at which the deviation is the greatest. **c** Difference in qubit resonance frequencies between the upward and downward sweep direction of the external magnetic field.

to the gate, as described in Section 3.4. For such a connection, the RF input power decreases for frequencies below approximately 16 GHz. Therefore, it is possible that, for frequencies below 8 GHz, the driving power was simply too low to induce a spin transition using the rapid adiabatic passage chirp. However, all measurements used to characterise the CoMM magnetisation were performed with an RF line directly wire-bonded to the CC gate, thus creating a direct connection. This configuration leads to a behaviour where the attenuation of the RF power decreases at lower frequencies, allowing for even higher possible driving powers for the qubit. Thus, a loss in RF driving power is ruled out as the explanation for the inability to measure qubit resonance frequencies below 8 GHz.

Another possibility could be that, by lowering the external magnetic field further to measure qubit frequencies below 8 GHz, the Zeeman energy is also reduced. This leads to a smaller ratio of Zeeman energy to the thermal energy of the electron reservoir, which in turn results in a progressively worse SNR during the spin-selective readout. However, as seen in the data in Figure 6.6**c**, the magnetic field steps at which the qubit resonance frequency was determined become increasingly smaller at the lowest magnetic fields. This was due to the attempt to investigate the rather abrupt disappearance of the qubit resonance signal. If the loss of SNR were solely due to the lower Zeeman energy relative to the thermal energy, it should decrease more gradually as the external field is lowered, compared to the sudden drop observed.

Thus, the main explanation for the vanishing qubit resonance signal below 8 GHz is attributed to the decreasing magnetisation of the CoMM and the resulting changes in its field gradient at the qubit position. This gradient is crucial for the EDSR qubit drive, and variations in the gradient can lead to significant changes in the qubit drive amplitude. Moreover, the observed hysteretic behaviour already suggests that, at external magnetic fields below 0.2 T, this hysteresis becomes more pronounced, leading to increasingly significant changes in the field gradient provided by the CoMM.

6.4. Rabi oscillations

The cyclic behaviour of a two-level quantum system under an oscillating driving field is referred to as Rabi oscillations, named after the physicist Isidor

Rabi, who first observed them in atomic spectroscopy experiments during the 1930s [195]. In case of a qubit, its state can be represented by a point on the Bloch sphere, and its time evolution can be described as the trajectory of this point on the surface of the Bloch sphere, as explained in Section 2.3:

$$|\Psi\rangle = \alpha\,|0\rangle + \beta\,|1\rangle \tag{6.4}$$

$$= \cos(\theta/2)\,|0\rangle + e^{i\phi}\sin(\theta/2)\,|1\rangle\,, \tag{6.5}$$

For the Loss-DiVincenzo qubit discussed here, the ground state $|0\rangle$ and excited state $|1\rangle$ are separated by the Zeeman energy resulting from a constant external magnetic field applied along the z-axis, $\vec{B}_{\text{ext}} = B_{\text{ext}}\vec{e}_z$. The spin aligns with this external field and precesses around the axis at the Larmor frequency. This spin can be driven by applying an oscillating magnetic field, perpendicular to the spin alignment, $\vec{B}_1(t) = B_1\cos(\omega t)\vec{e}_x$. The Hamiltonian of the system is given by [196]:

$$H(t) = H_0 + H_1(t) \tag{6.6}$$

$$= \frac{1}{2}g\mu_B B_{\text{ext}}\sigma_z + \frac{1}{2}g\mu_B B_1\cos(\omega t)\sigma_x, \tag{6.7}$$

with the respective pauli matrices σ_x and σ_z. To simplify this time-dependent Hamiltonian the rotating wave approximation (RWA) can be used. The idea is to move into a frame rotating at the frequency ω of the applied AC field, which simplifies the time dependence.

In the rotating frame, the system Hamiltonian becomes:

$$H_{\text{RWA}} = \frac{\hbar}{2}\Delta\omega\sigma_z + \frac{\hbar}{2}\Omega_R\sigma_x = \frac{\hbar}{2}\begin{pmatrix}\Delta\omega & \Omega_R\\ \Omega_R & -\Delta\omega\end{pmatrix} \tag{6.8}$$

where $\Delta\omega = \omega_0 - \omega$ is the detuning, with $\omega_0 = g\mu_B B_{\text{ext}}/\hbar$ being the natural Larmor frequency of the qubit, and

$$\Omega_R = g\mu_B B_1/\hbar \tag{6.9}$$

is the Rabi frequency, which characterises the strength of the driving field.

The solution to the time-dependent Schrödinger equation for the time-independent Hamiltonian H_{RWA} is given by the unitary transformation:

$$|\psi(t)\rangle = e^{-\frac{i}{\hbar}H_{\text{RWA}}t}\,|\psi(0)\rangle\,. \tag{6.10}$$

The probability to observe the qubit in the $|1\rangle$ state at the time t, can now be determined by

$$P_{|1\rangle}(t) = |\langle 1|\psi(t)\rangle|^2. \tag{6.11}$$

If the qubit is initially in the ground state $|\psi(0)\rangle = |0\rangle$, and assuming resonant driving frequencies, for which the first term in Equation (6.8) vanishes, the probability to find the qubit in the excited state results in:

$$P_{|1\rangle}(t) = \sin^2\left(\frac{\Omega_R}{2}t\right) = \frac{1}{2}(1 - \cos(\Omega_R t) \tag{6.12}$$

So under the influence of a driving field at resonance frequency the two level quantum system transitions between its two states with the Rabi frequency Ω_R. This is visualised in Figure 6.7**a**, where the qubit state, represented as a vector on the Bloch sphere, is rotating around the x-axis. Figure 6.7**b** shows the measured spin-up fraction for different microwave pulse lengths applied at the qubit resonance frequency. The rotational frequency f_{Rabi} is extracted by fitting the oscillating data with a sine function. The measurement was performed for a qubit resonance frequency of 18.5 GHz with a microwave output power of 24 dBm and yields a Rabi frquency of $f_{\text{Rabi}} = (5.24 \pm 0.01)$ MHz which is state of the art driving speed when comparing to university grade devices [47, 55], and the highest value when comparing EDSR devices manufactured in industrial foundries [59, 62, 109].

As mentioned above, the Rabi frequency depends on the amplitude of the driving field. In case of the EDSR qubit used here, the driving field amplitude is determined by a combination of the external magnetic field gradient, which is perpendicular to the applied magnetic field that defines the spin alignment, and the amplitude of spatial oscillations in this magnetic field gradient, caused by the oscillating electrostatic field applied to the driving gate. The Rabi frequency can be calculated by:

$$f_{\text{Rabi}} = \frac{g\mu_B}{h} \cdot \frac{dB_\perp}{dy} \cdot \delta y \tag{6.13}$$

with the perpendicular magnetic field gradient $dB_\perp/dy$ along the direction of the spatials oscillations, and the amplitude of the spatial directions δy. Based on the simulations of the CoMM mentioned in Section 6.3, using a magnetic field gradient of $dB_\perp/dy \approx 1.2\,\text{mT/nm}$, results in spatial oscillations of $\delta y \approx 0.3\,\text{nm}$. While a Rabi frequency of $f_{\text{Rabi}} \approx 5\,\text{MHz}$ is already a record value for industrially fabricated devices, spatial oscillations of 1 nm and above

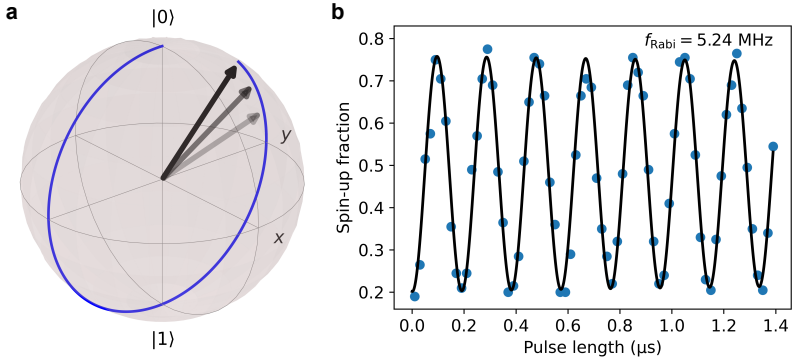

Figure 6.7.: a Representation of Rabi oscillations on the Bloch sphere. The qubit state is represented as a vector pointing towards a point on the surface of the Bloch sphere. If the driving frequency matches the Lamor frequency of the electron spin, the vector is rotated around the x-axis with the frequency f_{Rabi}. **b** Measured spin-up fraction of the qubit depending on the microwave pulse length. Every value of the spin-up fraction is the result of 200 single shot measurements. The black line corresponds to a sine fit to the data yielding a Rabi frequency $f_{\mathrm{Rabi}} = (5.24 \pm 0.01)$ MHz. The measurement is performed at a qubit resonance frequency of 18.5 GHz with a microwave output power of 24 dBm.

are reported [182, 190]. Assuming the simulated perpendicular magnetic field gradient, spatial oscillations of 1 nm would result in a Rabi frequency of ≈ 16.7 MHz, which would speed up the manipulation pulses even further. The Rabi frequency dependence on the microwave drive power is further investigated in the next section.

Now, also considering the first term in the Hamiltonian in Equation (6.8), which becomes relevant when the qubit drive is not at the exact qubit resonance frequency. For a detuned drive, the qubit state is also rotated around the z-axis on the Bloch sphere, depending on the strength of the detuning. The Rabi frequency in case of a detuned drive becomes:

$$\Omega_{\mathrm{eff}} = \sqrt{\Delta\omega^2 + \Omega_R^2} \tag{6.14}$$

The rotation speed effectively increases for higher detunings and the trajectory of the rotation on the Bloch sphere becomes tilted. This is visualized in Figure 6.8**a**, for $\Delta\omega = 0$ (blue) , $\Delta\omega = \Omega_R/2$ (red), $\Delta\omega = \Omega_R$ (green) and $\Delta\omega = 2\Omega_R$ (black). The qubit is measured by projecting the state on the z-axis. This results for a detuned Rabi frequency in a faster oscillation speed, but

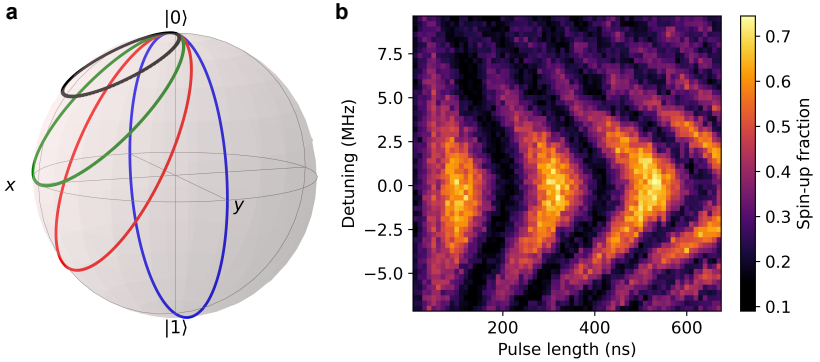

Figure 6.8.: **a** Representation of the qubit trajectory on the Bloch sphere for resonant (blue) and off-resonant microwave drive (red, green, black). **b** Measured spin-up fraction of the qubit for different microwave detunings, depending on the microwave pulse length. Because of the shape of the patter also called a Chevron pattern. Measured at a microwave output power of 23 dBm over a span of ≈ 7 h.

the probability to end up in the excited state decreases, and therefore the amplitude of the oscillations. The spin-up fraction of the qubit for different microwave pulse lengths and frequency detunings is shown in Figure 6.8**b**, which demonstrates the previously described behaviour. The maximum amplitude is measured for zero detuning. As the detuning increases, the frequency of the oscillations increases while the probability of the qubit ending up in the excited state decreases. Because of its visual shape, which resembles a chevron pattern, such a measurement is often called a Chevron Rabi measurement. It helps to identify the true qubit resonance frequency because changes in the qubit resonance frequency are clearly visible compared to a 1D measurement. The entire measurement was carried out over a period of approximately 7 h which demonstrates the long term stability of the qubit resonance frequency and readout working point.

The final parameter to consider in relation to Rabi oscillations and qubit manipulations is the phase dependence of the oscillating driving field. Adding

a phase ϕ to the oscillating magnetic field $\vec{B}_1(t) = B_1 \cos(\omega t + \phi)\vec{e}_x$, the Hamiltonian in the rotating wave approximation is modified:

$$H_{\text{RWA}} = \frac{\hbar}{2}\Delta\omega\sigma_z + \frac{\hbar}{2}\Omega_R(\cos(\phi)\sigma_x + \sin(\phi)\sigma_y) \tag{6.15}$$

$$= \frac{\hbar}{2}\begin{pmatrix} \Delta\omega & \Omega_R e^{-i\phi} \\ \Omega_R e^{i\phi} & -\Delta\omega \end{pmatrix} \tag{6.16}$$

The off-diagonal elements now carry a complex phase factor $e^{i\phi}$, reflecting the phase shift in the oscillating magnetic field. The phase ϕ effectively rotates the direction of the driving field in the xy-plane of the Bloch sphere. Physically, this means:

- When $\phi = 0$, the driving field is aligned along the x-axis.
- When $\phi = \pi/2$ (90°), the driving field is aligned along the y-axis.

In summary, Rabi oscillations describe the oscillating probability of a two-level quantum system transitioning between its two states under an external driving field. The field's frequency controls the rotation angle in the xz-plane, while its phase sets the rotation angle in the xy-plane. Additionally, the amplitude and duration of the external field determine the speed and distance traveled by the state.

For a spin qubit, applying a resonant driving field $\vec{B}_1(t)$ with control over the phase ϕ is sufficient to create arbitrary qubit rotations, allowing full control on the Bloch sphere and enabling the implementation of universal quantum gate operations.

6.5. Qubit drive power dependence

As described in the previous chapter, the Rabi frequency of the qubit determines its manipulation speed and, consequently, the speed at which calculations can be performed, making it a key metric for qubit characterisation and quality. Maximising the Rabi frequency, without disturbing the system through heating or additional dephasing noise from the microwave pulse, will result in optimal qubit performance. Figure 6.9**a** shows the measured spin-up fraction of the qubit for increasing pulse length and varying microwave output powers. As expected, to increasing power, the frequency

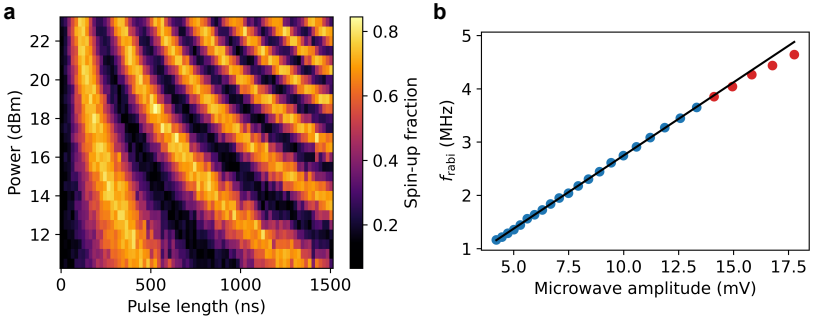

Figure 6.9.: **a** Measured spin-up fraction for increasing pulse length and varying microwave output powers. **b** Extracted Rabi frequencies for all used powers of the measurement shown in **a** converted to the corresponding microwave amplitude in mV after accounting for a total inline attenuation of 45 dB. The black line corresponds to a linear fit excluding the 5 data points of highest applied power (marked in red).

of the oscillations continuously increases, and all displayed powers show no visible change in amplitude during the displayed pulse length window. In Figure 6.9**b**, the Rabi frequency is extracted for each applied power and plotted against the respective microwave amplitude in mV, after accounting for an estimated total inline attenuation of 45 dB (26 dB attenuation from the RF transmission line at 18.5 GHz and an additional 19 dB from inline RF attenuators. See Section 3.4 for details). The Rabi frequency increases linearly over the whole amplitude range up to values of about 13 mV. Above these amplitudes, a deviation from the linear increase and a starting saturation of the Rabi frequency is measured. Saturation is a sign of a different qubit drive regime. One explanation could be a lower magnetic field gradient for higher microwave and therefore quantum dot displacement amplitudes. But the displacement is quite small and the magnetic field gradient should stay constant over $\approx \pm 40$ nm around the centre of the CoMM gap when trusting the simulations. Another possibility could be an anharmonic qubit quantum dot confinement potential, dampening larger displacements of the quantum dot position [194, 197–199]. However, the exact reason for the saturation effect remains unclear for now and needs further investigation.

Exploring the behaviour of the Rabi frequency at microwave powers beyond 24 dBm would also be of interest. However, the measurement electronics are currently limited to 24 dBm at 18.5 GHz, so removing attenuation in the RF

line would be necessary, and this has been scheduled for a later cooldown. Additionally, further investigation into the behaviour of the Rabi frequency for different quantum dot positions along the y-axis, achieved by adjusting the voltages at screening gates CC and CT, could potentially enable even faster qubit manipulation speeds in the future.

6.6. Determining the spin coherence times

Being able to induce Rabi oscillations opens the gateway to all other coherent qubit manipulation schemes. However, the effectiveness of these manipulations relies not only on the ability to control the qubit but also on how long the qubit can maintain its coherent state before decoherence sets in. This duration, known as the spin coherence time, is crucial because it defines the operational time window within which quantum information can be reliably stored and processed. The most common methods for determining qubit coherence times are Ramsey Interferometry and the Hahn Echo technique. Ramsey Interferometry, developed by Norman Ramsey [200] based on concepts from Isidor Isaac Rabi, is used to measure the dephasing time T_2^*. The Hahn Echo (or spin echo) method, introduced by Erwin Hahn, who first observed spin echoes in nuclear magnetic resonance experiments [201], is used to measure the spin coherence time T_2^{H}.

6.6.1. Ramsey and spin coherence time T_2^*

The Ramsey pulse sequence is shown in Figure 6.10**a** and consists of a $\pi/2$-pulse followed by a varying waiting time τ, and finished by a second $\pi/2$-pulse which has to be in phase with the first $\pi/2$-pulse. In Figure 6.10**c**, the Ramsey pulse sequence is illustrated on the Bloch sphere. The qubit is initialised in the ground state $|0\rangle$ and the first $\pi/2$-pulse induces a 90° rotation around the x-axis. This rotates the qubit vector on the equator of the Bloch sphere, at which the qubit is allowed to evolve for a variable waiting time τ. During this time, noise on the qubit resonance frequency will lead to a dephasing of the state, relative to the initial phase. Mathematically, this dephasing can be modeled as a rotation around the z-axis on the Bloch sphere, and represents the accumulated phase due to noise. This dephasing is visualized by the red trajectory and vectors in Figure 6.10**c**. The final in-phase $\pi/2$-pulse rotates

the qubit vector further by 90° around the x-axis. For $\tau = 0$, the Ramsey pulse sequence is equivalent to a π-pulse, rotating the qubit from the ground state into the excited state. However, for a finite time τ, the accumulated phase during this period causes the resulting state to increasingly deviate from the ideal spin-up state. The qubit state ends up in a random result, when the phase information is lost.

When executing the pulse sequence with detuning, the qubit vector is actively rotating around the z-axis during the waiting time τ at the frequency corresponding to the detuning. This is visualized by the green trajectory in Figure 6.10**d**, and the dephasing component is added to the z-rotation. The active detuning induces oscillations in the final spin projection, corresponding to the set detuning frequency. Figure 6.10**b** shows the measured spin-up fraction for a Ramsey pulse sequence, for different τ waiting times and frequency detunings. With zero detuning, the spin-up fraction decays continously to longer τ waiting times. With increasing frequency detuning, oscillations in the spin-up fraction become visible. These oscillations match the same frequency as the given detuning, and lead to the overall visible pattern known as Ramsey fringes.

The measured spin-up fraction after a Ramsey pulse sequence for increasing τ waiting times, and a constant detuning of 2 MHz is shown in Figure 6.10**e**, and the same for a constant detuning of 6 MHz is shown in Figure 6.10**f**. The experimental data is fitted using a function of the form $A\sin(Bt + \phi) \cdot \exp(-(t/T_2^*)^2) + C$, which represents a Gaussian-damped oscillation. In this expression, the frequency corresponds to the detuning from the qubit's resonance frequency, while the decay time is determined by the characteristic spin dephasing time T_2^*. For both measurements, the spin dephasing time T_2^* results in $\approx 1\,\mu s$, with the primary difference being the frequency of the oscillations. This demonstrates that, while the decay characteristics remain consistent, the oscillation frequency varies with the applied detuning. To reliably extract T_2^*, it is therefore more robust to utilize a frequency detuning which is significantly larger than the noise amplitude affecting the resonance frequency. In contrast, a Ramsey measurement performed at resonance will be highly sensitive to even small shifts in the qubit's resonance frequency, resulting in distortion of the curve.

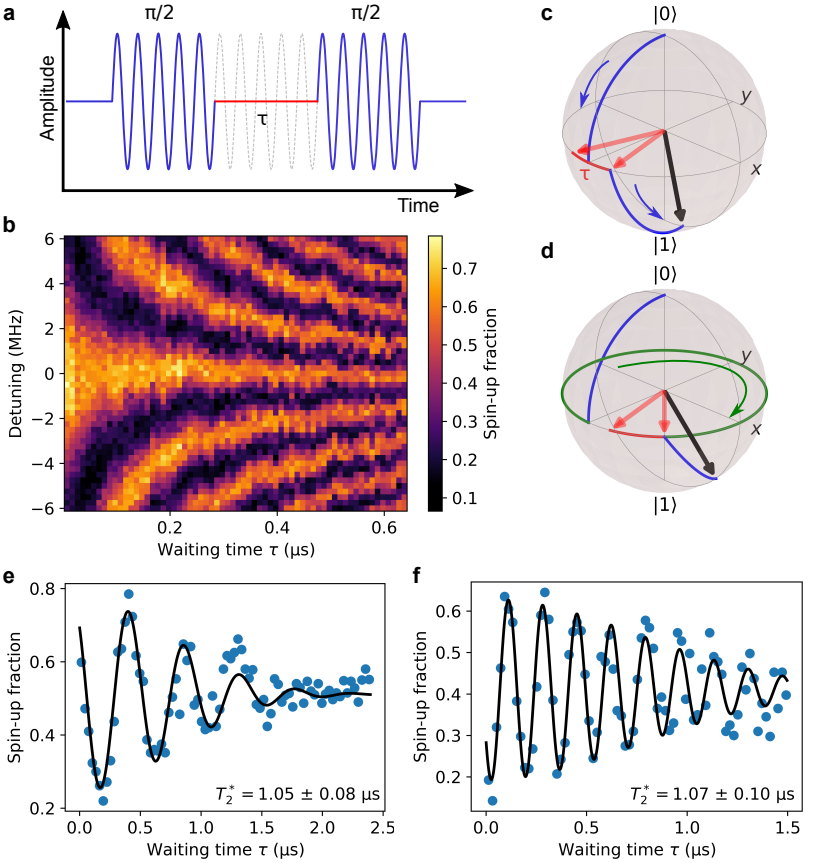

Figure 6.10.: **a** Amplitude over time of the microwave pulse to perform a Ramsey experiment. **b** Measured spin-up fraction after a Ramsey pulse sequence for varying frequency detuning and waiting time τ between the two $\pi/2$-pulses, measured over the course of ≈ 6 h. **c** Representation of the qubit vector trajectory on the Bloch sphere for a pulse on resonance and **d** for a detuned pulse. The red arrows represent dephasing of the qubit state. For a given detuning the qubit state is rotating around the z-axis with the frequency of the detuning in addition to the intrinsic dephasing. The additional z-rotation due to detuning is visualised in green. The z-rotation leads to oscillations between spin-up and spin-down of the final projection for an increasing waiting time τ, which is visible in the form of the Ramsey fringes in **b**. The resulting spin-up fraction for increasing waiting time τ for a Ramsey pulse sequence for intentional detuning of 2 MHz in **e**, and 6 MHz in **f**. The black curve corresponds to a fit of the form $A\sin(Bt+C)\cdot\exp(-(t/T_2^*)^2)$, resulting in gaussian damped oscillations with the frequency of the detuning, and the decay time corresponding to the characteristic spin dephasing time T_2^*.

6.6.2. Spin echo and spin coherence time T_2^{H}

The spin echo pulse sequence is shown in Figure 6.11**a** and consists of a $\pi/2$-pulse followed by a varying waiting time $\tau/2$, an in-phase π-pulse, a second waiting time $\tau/2$, and a final in-phase $\pi/2$-pulse. For $\tau = 0$, the qubit is rotated in total by 2π around the x-axis and the qubit state ends up in its initial state. Now introducing a finite waiting time between the pulses, the picture changes. Figure 6.11**b** visualises the effect of the pulse sequence on the qubit state vector on the Bloch sphere. The first $\pi/2$-pulse rotates the qubit vector onto the equator by a 90° x-rotation. On the equator, noise on the qubit frequency can induce a z-rotation of the qubit vector during the waiting time $\tau/2$, resulting in a change of the qubit phase. The phase accumulated during the waiting time, often referred to as the "free evolution time", will affect the outcome of the 180° rotation around the x-axis, induced by the in-phase π-pulse of the pulse sequence. The qubit state is rotated on the other side of the equator, and a phase shift ϕ is converted to a $-\phi$ phase shift. Now during the second waiting time $\tau/2$, while still being objected to the same noise amplitude, the qubit phase drifts further, but is now compensating the previous dephasing effect. The qubit refocuses, and the second π-pulse of the spin echo sequence is therefore also called the "refocusing pulse". The final in-phase $\pi/2$-pulse rotates the qubit vector again by 90° around the x-axis and the qubit state is read out by projection onto the z-axis. Because of this refocusing effect, the qubit is only affected by noise frequencies in the same order of magnitude as the total waiting time $1/\tau$. Noise frequencies much smaller/larger will average out in a spin echo sequence. The resulting spin-up fraction for a spin echo pulse sequence over the increasing total waiting time τ is shown in Figure 6.11**c**. The data is fitted by a function of the form $A \cdot \exp(-(t/T_2^{\mathrm{H}})^{\alpha} + C$ and results in a spin coherence time $T_2^{\mathrm{H}} = (51.24 \pm 1.49)\,\mu\mathrm{s}$ with an exponent $\alpha = 2.06 \pm 0.17$.

6.6.3. Discussion of the extracted spin coherence times

The measured dephasing time of $T_2^* \approx 1\,\mu\mathrm{s}$, is similar to the reported values in other natural silicon spin qubit devices [109, 191, 194] and consistent for all four measured qubit devices in this work (see Appendix A.1). The extracted T_2^{H} value of approximately 50 µs, along with an exponent $\alpha \approx 2$, indicates a Gaussian damped decay, typically observed in systems where the primary decoherence mechanism follows a $1/f$ noise spectrum [150, 167, 202].

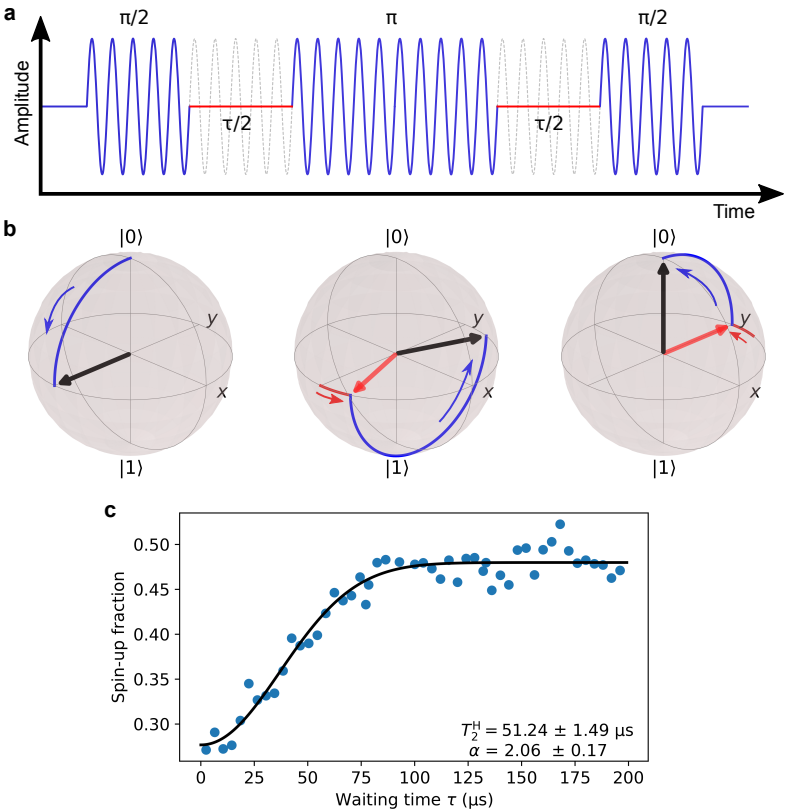

Figure 6.11.: a Amplitude over time of the microwave pulse to perform a spin echo experiment. **b** Representation of the effect of the spin echo sequence on the qubit vector on the Bloch sphere. The first $\pi/2$-pulse rotates the qubit vector on the equator of the Bloch sphere. During the $\tau/2$ waiting time, the phase is affected by noise on the qubit resonance frequency and dephases. The in-phase π-pulse brings the qubit vector on the other side of the Bloch sphere, by a 180° rotation around the x-axis, and converts a phase shift ϕ to a phase shift $-\phi$. Affected by the same noise on the qubit resonance frequency, the further dephasing in the same direction results in a refocusing effect of the qubit, by canceling out the phase shift. The final in-phase $\pi/2$-pulse rotates the again by 90° around the x-axis, bringing the qubit back to the initial state. **c** Measured spin-up fraction after performing the spin echo pulse sequence for increasing total waiting time τ. The data is fitted by a function with the form $A \cdot \exp(-(t/T_2^H)^\alpha + C$.

Comparing T_2^* and T_2^{H} highlights the frequency-dependent nature of the dominant decoherence channel, revealing that noise amplitudes increase at lower frequencies. In natural silicon, the abundance of nuclear spins of the ^{29}Si isotope near the qubit is known to be the primary source of decoherence [48, 127]. Isotopic enrichment of ^{28}Si can therefore significantly mitigate this low-frequency decoherence channel, and thereby increase the T_2^* time by orders of magnitude [55, 62, 191, 203].

6.7. Randomised benchmarking and gate fidelity

The final metric regarding qubit characterisation, is the benchmarking of the qubit gate fidelity. A first estimate can be done by performing long Rabi experiments in which a decay of the amplitude can be extracted. Figure 6.12**a** shows the measured spin-up fraction for increasing microwave pulse lengths up to 8 µs. The data is fitted with the function $A \cdot \sin(Bt+C) \cdot \exp(-t/T_{\mathrm{Rabi}})+D$ and gives a decay time of $T_{\mathrm{Rabi}} = (8.71 \pm 0.69)$ µs with a π-pulse length of (94.94 ± 0.03) ns. The ratio between both values defines the quality factor Q and gives:

$$Q = \frac{T_{\mathrm{Rabi}}}{t_\pi} \approx 92 \tag{6.17}$$

which effectively means that approximately 92 π-pulses can be performed before the amplitude of the Rabi oscillations decays to $1/e$ of its initial value. However, this value only reflects the fidelity when repeatedly applying the same gate, which is not the case when using the qubit for computations.

To obtain a more realistic measure of gate fidelity, randomised benchmarking is performed. In randomised benchmarking, the qubit is initialised in a specific state, and a sequence of randomly selected quantum gates, often from the Clifford group, is applied to the qubit(s). After applying these randomly chosen gates, a final "inversion" gate is applied to return the qubit(s) to their original state. The length of these random gate sequences varies, allowing the observation of how errors accumulate over different numbers of operations, allowing the extraction of a more accurate gate fidelity [204–206]. The Clifford group is a set of quantum gates that can be efficiently simulated on classical computers and plays a key role in fault-tolerant quantum computing [207–209]. Widely used in the quantum computing community, the Clifford group allows qubit systems to be compared across different hardware platforms.

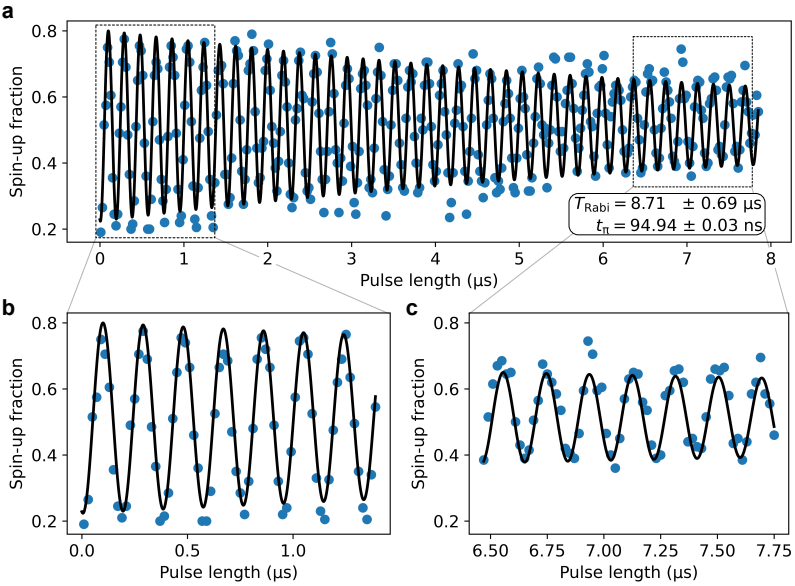

Figure 6.12.: a Measured spin-up fraction for a resonant microwave pulse with increasing duration. The measurement was performed at a microwave output power of 24 dBm at a qubit resonance frequency of 18.5 GHz. The black line represents a fit of the entire dataset using an exponentially decaying sine function. **b** and **c** provide zoomed-in views of the highlighted rectangles to demonstrate the matching phase of the fit across the entire dataset.

For a single qubit, there are 24 unique Clifford gates. However, not all of these gates can be directly executed on a physical qubit. Instead, a set of basic, primitive gates that can be performed with the physical qubit is used to construct each of the 24 Clifford gates as a sequence of operations. This primitive gate set fully represents the Clifford group on the qubit.

6.7.1. Single qubit Clifford gates and primitive gate set

The single qubit Clifford gates and the primitive gate set representation is derived by following [210]. The single qubit Clifford operators are decomposed by introducing the Pauli group P = $\{I, \sigma_x, \sigma_y, \sigma_z\}$, with

$$I = \begin{pmatrix} 1 & & & \\ & 1 & & \\ & & 1 & \\ & & & 1 \end{pmatrix}, \qquad \sigma_x = \begin{pmatrix} 1 & & & \\ & 1 & & \\ & & -1 & \\ & & & -1 \end{pmatrix},$$

$$\sigma_y = \begin{pmatrix} 1 & & & \\ & -1 & & \\ & & 1 & \\ & & & -1 \end{pmatrix}, \qquad \sigma_z = \begin{pmatrix} 1 & & & \\ & -1 & & \\ & & -1 & \\ & & & 1 \end{pmatrix},$$

where σ_x, σ_y, σ_z correspond to π rotations around the x, y and z axes. The exchange group S = $\{I, \mathcal{S}, \mathcal{S}^2\}$ with

$$\mathcal{S} = \begin{pmatrix} 1 & & & \\ & & & 1 \\ & 1 & & \\ & & 1 & \end{pmatrix}, \mathcal{S}^2 = \begin{pmatrix} 1 & & & \\ & & 1 & \\ & & & 1 \\ & 1 & & \end{pmatrix},$$

permutes (x,y,z) → (z,x,y) → (y,z,x), and the Hadamard group H = I,$\mathcal{H}$

$$\mathcal{H} = \begin{pmatrix} 1 & & & \\ & & & 1 \\ & & -1 & \\ & 1 & & \end{pmatrix}$$

which exchanges (x,y,z) → (z,-y,x). The single qubit Clifford gates are the possible combinations of the elements in P, S and H and result in 4 x 3 x 2 = 24 single qubit Clifford gates. Table 6.1 gives the complete list of all 24 single qubit Clifford gates and the physical representation using the primitive gate set $\{I, \pm X, \pm Y, X^2, Y^2\}$, where $\pm X$ corresponds to a $\pm 90^\circ$ rotation around the x-axis and X^2 a 180° rotation. Using this primitive gate set, a single qubit Clifford gate consists on average out of 1.875 primitive gates.

Table 6.1.: 24 Single qubit Clifford gates and primitive gate representation

Clifford elements	Primitive gates
I, I, I	I
σ_x, I, I	X^2
σ_y, I, I	Y^2
σ_z, I, I	X^2, Y^2
$I, I, \mathcal{S}$	Y, X
$\sigma_x, I, \mathcal{S}$	$-Y, -X$
$\sigma_y, I, \mathcal{S}$	$-Y, X$
$\sigma_z, I, \mathcal{S}$	$Y, -X$
$I, I, \mathcal{S}^2$	$-X, -Y$
$\sigma_x, I, \mathcal{S}^2$	$X, -Y$
$\sigma_y, I, \mathcal{S}^2$	X, Y
$\sigma_z, I, \mathcal{S}^2$	$-X, Y$
$I, \mathcal{H}, I$	Y, X^2
$\sigma_x, \mathcal{H}, I$	$-Y$
$\sigma_y, \mathcal{H}, I$	$-Y, X^2$
$\sigma_z, \mathcal{H}, I$	Y
$I, \mathcal{H}, \mathcal{S}$	$-X$
$\sigma_x, \mathcal{H}, \mathcal{S}$	X
$\sigma_y, \mathcal{H}, \mathcal{S}$	X, Y^2
$\sigma_z, \mathcal{H}, \mathcal{S}$	$-X, Y^2$
$I, \mathcal{H}, \mathcal{S}^2$	$X, -Y, -X$
$\sigma_x, \mathcal{H}, \mathcal{S}^2$	X, Y, X
$\sigma_y, \mathcal{H}, \mathcal{S}^2$	$X, -Y, X$
$\sigma_z, \mathcal{H}, \mathcal{S}^2$	$X, Y, -X$

6.7.2. Generation of the pulse sequence

As explained above, a randomised benchmarking experiment consists of a qubit initialisation, followed by a random sequence of length n, and concludes with a final gate that inverts the random sequence, returning the qubit to its initial state. For instance, if the initial state is the ground state $|0\rangle$, then after applying n random gates, the final inversion gate should ideally return the qubit to the ground state. Deviations from this initial and final result are due to gate errors, which accumulate progressively as n increases. When measuring the spin-up fraction, a perfectly initialised spin-down state will show an increase in the measured spin-up fraction from 0 % to 50 % as the qubit phase information is lost with increasing n. This results in a maximum signal amplitude of 50 % for changes in the spin-up fraction. By performing the same random sequence twice, and rotating the final state once to spin down and once to spin up, and then taking the difference between these results, the change in signal caused by gate errors is effectively doubled. Additionally, this differential approach is more robust to drifts in the readout working point, as both spin-up and spin-down projections will be equally affected by any drift, preserving the relative difference.

Figure 6.13 illustrates an example pulse sequence for a random gate sequence with length $n = 8$. The qubit starts in the spin-down ground state and a X-gate is chosen as an initialisation pulse, which rotates the qubit vector onto the equator of the Bloch sphere and gives a phase reference for all further pulses. This first X gate can also be omitted and the ground state of the qubit can be chosen as the initial state. Historically, initialisation with an X gate was chosen for testing of the randomised benchmarking software. Either approach does not affect the final result of gate fidelity, as fidelity is measured based on the change over increasing sequence length n. This measurement remains independent of the quality of the qubit initialisation, provided that the initialisation process is kept consistent throughout.

After initialisation, a random sequence of $n = 8$ gates, chosen from the primitive gate set, is applied. The mathematical transformation of the random sequence on the qubit state must be calculated and tracked to determine the final gate needed to invert the random gate sequence. This inversion gate is then executed, and the qubit state is read out. Figure 6.13**b** and **c** present zoomed-in views of the highlighted rectangles in Figure 6.13**a**, illustrating the relative phase shift with respect to the phase reference (shown in grey),

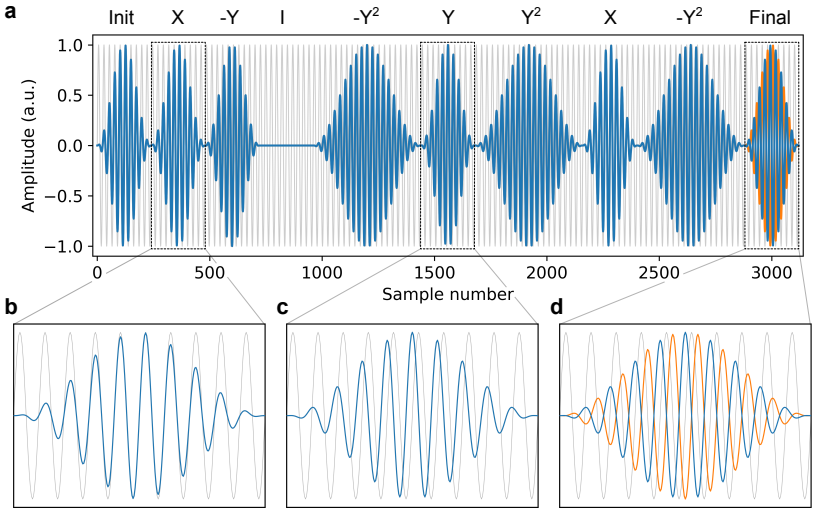

Figure 6.13.: **a** Example pulse sequence for a randomised benchmarking measurement with sequence length $n = 8$. The qubit is always initialised in the same state, followed by a random gate sequence of length n. After completing this random gate sequence, a single gate returns the qubit to a defined final state for readout. A Hann window function is applied here to visually distinguish the different gates from one another. The actual experiment was conducted using a rectangular window function. The grey sine wave in the background provides a phase reference and is in-phase with the X gates. **b** A zoomed-in view of an X gate, which rotates the qubit by 90° around the x-axis. **c** Implementation of a Y gate, which has a 90° phase shift relative to the X gate, and rotates the qubit by 90° around the y-axis. **d** A close-up of the final inversion gate. The entire random sequence is performed twice: once with a final projection onto the spin-up state (blue), and once with a final projection onto the spin-down state (orange). The difference between these two results is used to estimate the gate error, effectively doubling the signal amplitude compared to using a single final projection.

which is in-phase with the X gates. Figure 6.13**d** shows the final rotation of the qubit state, once into the excited spin-up state (blue) and once into the ground state (orange). Each randomised sequence is thus performed twice, and the difference in the final projection is used to extract the gate fidelity, as explained above.

All gates in the example were multiplied by a Hann-window function in order to distinguish the different gates better from each other visually. However, for the actual measurements, no active windowing was applied, effectively making it equivalent to a rectangular window function. The use of a Hann-

window function was tested, but the power loss introduced by the windowing led to a reduction in qubit manipulation speed. This loss in power could not be simply offset by increasing the external microwave output, as the measurement electronics were already at the maximum output power. The reduced manipulation speed consequently led to lower gate fidelities compared to using a rectangular window function combined with the higher manipulation speeds. Optimisations to the RF setup, combined with the use of windowed manipulation pulses, should result in even better qubit performance and gate fidelity [211].

6.7.3. Pulse calibration

Before performing the actual randomised benchmarking experiments, it is essential to calibrate the gate durations of the primitive gate set with maximum precision, otherwise the qubit gate fidelity may suffer due to avoidable calibration errors. For example, as indicated by the error bounds of the Rabi frequency fit in Figure 6.7, the extracted Rabi frequency, and consequently the π-pulse duration τ_π, has an imprecision of approximately 0.2 %. While this level of imprecision is negligible for the Ramsey or spin echo pulse schemes, it becomes significant when performing, for instance, 100 sequential π-pulses, as might be required in a randomised benchmarking sequence. In such a case, an error of 0.2 % would accumulate to 20 %, resulting in under- or over-rotation of the qubit state for the given sequence length.

Additionally, all measurement electronics are inherently constrained by the maximum sampling rate, limiting time increments accordingly. Consequently, pulse durations cannot be chosen arbitrarily but must be multiples of the hardware's sampling increment. Therefore, to minimise pulse calibration errors, the π-pulse duration should be calibrated as precisely as possible within a reasonable timeframe, during which drift of the qubit resonance frequency is negligible. A simple yet highly accurate method for achieving this is introduced in the following. In the initial step, a rough estimate of the Rabi frequency and π-pulse length is obtained for a given microwave output power by following the standard procedure shown in Figure 6.7. The extracted π-pulse length is then rounded to the nearest integer multiple of the hardware sampling rate. This adjusted pulse length is extrapolated with the intention of performing, for example, 51 π-pulses in succession instead of just one. The ideal result of the 51 π-pulses would bring the qubit again to the

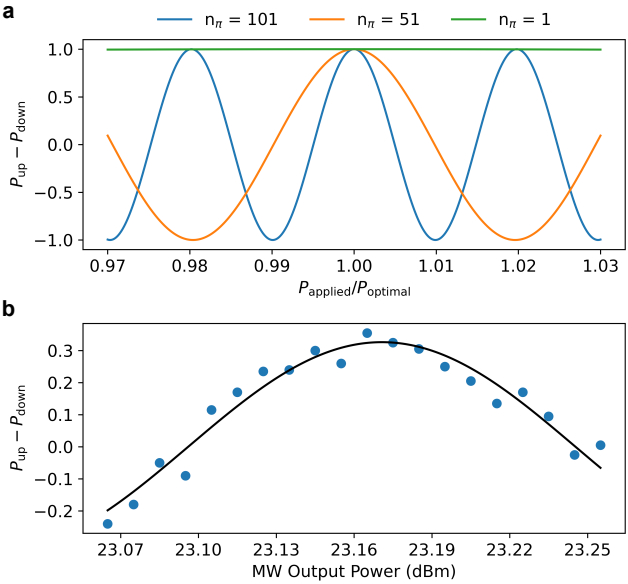

Figure 6.14.: **a** Difference of the probabilities of finding the qubit in the spin-up versus spin-down state for varying ratios of applied to optimal microwave output power, shown for 1 (green), 51 (orange), and 101 (blue) π-pulses. The difference of the probabilites doubles the maximum amplitude achievable in the measurement. The amount of π-pulses determines the sensitivity to errors in the applied power relative to the optimal power. While a 2 % error is barely noticeable in the green curve, the orange curve reaches a minimum, and the blue curve has already reached a second maximum, indicating a 2π under- or over-rotation. **b** Experimental realisation of the scenario depicted in **a** (blue curve). The data shows the measured spin-up fraction for 101 π-pulses minus the measured spin-up fraction for 100 π-pulses for varying microwave output powers. The microwave power at which the difference of the spin-up fractions reaches its maximum is then used for the subsequent randomised benchmarking measurements.

spin-up state. However, by performing the pulse 51 times instead of just once, any calibration error becomes 51 times more pronounced. The same pulse sequence is now performed for varying microwave output powers, which in turn changes the real Rabi frequency and π-pulse length. When the applied power matches the ideal power, a maximum signal is observed. However, for powers that deviate by 2 % from the ideal power, a minimum appears, as the 51 π-pulses will under- or over-rotate the qubit state by an additional π-pulse. This behaviour is illustrated by the orange curve in Figure 6.14**a**, which

shows the difference in probabilities of finding the qubit in the spin-up versus spin-down state for 51 π-pulses. By extracting this probability difference, the visibility of the result is effectively doubled, following the approach described in the previous section. By changing the amount of performed π-pulses, the sensitivity to errors can be adjusted. The blue curve in Figure 6.14**a** for example corresponds to 101 π-pulses and possesses double the sensitivity to the misscalibrated microwave output power, while the green curve shows barely any difference for the shown error margin of 3 %.

Figure 6.14**b** shows the experimental realisation of this calibration method. Each data point represents the difference between the measured spin-up fraction for 101 performed π-pulses and the measured spin-up fraction for 100 performed π-pulses. Ideally, 101 π-pulses should yield a maximum in the spin-up fraction, while 100 π-pulses should result in a minimum, making the difference a maximum once again. Slight variations in power induce under- or over-rotations, and the power level at which a maximum is observed corresponds to the ideal power for the given π-pulse duration.

6.7.4. Gate fidelity measurements

With the pulse sequences established and the pulse duration and microwave power precisely calibrated, the randomised benchmarking experiment can begin. Figure 6.15**a** shows the measured spin-up fraction following a randomised gate sequence of varying lengths. Each data point corresponds to the average spin-up fraction across 40 distinct randomised sequences, each performed and read out with 200 single-shot measurements. The blue data represents the final projection into the spin-up state, while the orange data represents the final projection into the spin-down state. As the number of gates n increases, the probability to reach the desired final state decreases due to cumulative gate errors and finite qubit lifetimes.

In Figure 6.15**b**, the difference between the final spin-up projection and the final spin-down projection is plotted for increasing n. This difference begins at a maximum for small n and converges to zero for large n, which is modelled by fitting a function of the form $A \cdot P^n$. The single qubit gate fidelity can now be calculated with

$$F = 1 - \frac{1 - P}{2} = (99.2 \pm 0.1)\,\%. \tag{6.18}$$

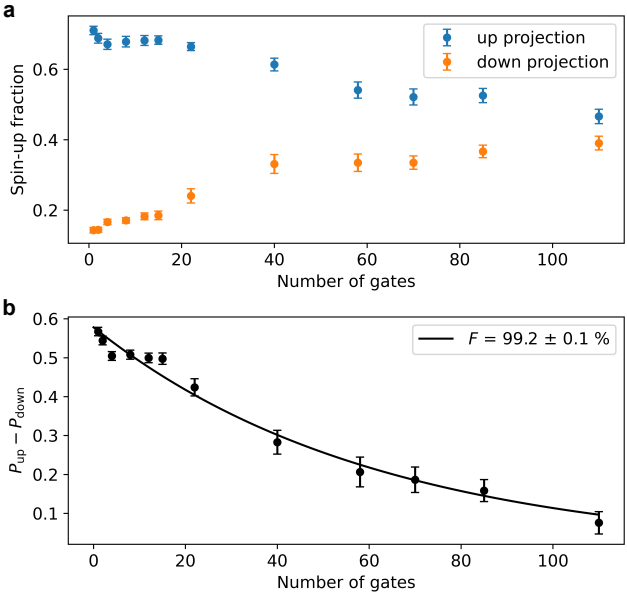

Figure 6.15.: **a** Spin-up fraction over the number of randomly applied gates with an ideal final result of spin-up (blue) and spin-down (orange). Every point corresponds to the mean spin-up fraction of 200 single shot measurements of 40 different randomised sequences. **b** Difference of the blue and orange data shown in **a**, which is used to extract the gate fidelity. The black curve corresponds to a fit of the form $A \cdot P^n$ which yields the primitive gate fidelity $F = 1 - (1 - P)/2 = (99.2 \pm 0.1)$ %.

This value corresponds to the primitive gate fidelity, as the random sequence consisted only of gates from the primitive gate set. The primitive gate fidelity can be converted to a Clifford gate fidelity by replacing the number of primitive gates n with the average number of Clifford gates n_c, as a single-qubit Clifford gate is composed, on average, of 1.875 primitive gates, as derived in Section 6.7.1. As a result, the primitive gate fidelity of (99.2 ± 0.1) % converts to a Clifford gate fidelity of (98.5 ± 0.1) %.

In Figure 6.16, the resulting primitive gate fidelity of (99.2 ± 0.1) % is shown in black and compared to the fidelity achieved when rotating around only one qubit axis: pure Y gates (blue) and pure X gates (orange). The gate fidelities

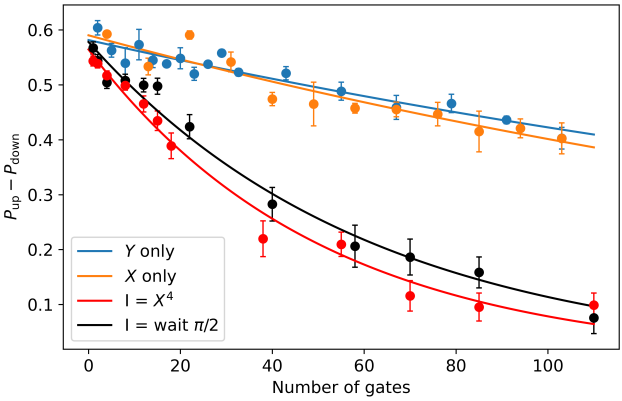

Figure 6.16.: Blue and orange correspond to rotations around one axis only, yielding gate fidelities of (99.81 ± 0.02) % for X-only rotations, and (99.82 ± 0.02) % for Y-only rotations. These fidelities are less affected by pulse calibration errors of the randomised sequences used in randomised benchmarking, and demonstrate an upper boundary set by the qubit lifetime itself. The black curve corresponds to the data shown in Figure 6.15**b** and was done by using a qubit idle time of the same duration as a $\pi/2$-pulse duration in order to implement the identity gate I and yields a gate fidelity of (99.2 ± 0.1) %. The red curve implements the identity gate I with a 2π-rotation and results in a gate fidelity of (99.0 ± 0.1) %

for single-axis rotations are (99.82 ± 0.02) % for pure y-axis rotations and (99.81 ± 0.02) % for pure x-axis rotations.

In Figure 6.16 the resulting primitive gate fidelty of (99.2 ± 0.1) % is drawn in black and is compared to a resulting gate fidelity, when only rotating around one qubit axis, in this case pure Y gates in blue and pure X gates in orange. The gate fidelities for single axis rotation results in (99.82 ± 0.02) % for pure y-axis rotations and (99.81 ± 0.02) % for pure x-axis rotations. These values are quite similar and represent an upper boundary for the achievable gate fidelity via randomised benchmarking, as single-axis rotations involve less frequency noise, consisting of a continuous sine wave, compared to the more complex randomised benchmarking pulses. Additionally, in randomised benchmarking, the qubit is more susceptible to phase errors than with pure single-axis rotations.

Further, two methods of implementing the identity gate I are compared. For the black data, the identity gate I was realised by an idle time for the

qubit equal to the duration to the time required for an X or Y gate (the time needed for a $\pi/2$-rotation). For the red data, randomised benchmarking was performed using the identity gate I implemented as a 2π-rotation instead of idling. This results in a reduced gate fidelity of (99.0 ± 0.1) %, likely explained by the four-times longer duration of the identity gate compared to a the idle time of a $\pi/2$-rotation, which accumulates more gate error.

An intermediate approach could involve implementing the identity gate I by sequentially applying an X gate followed by a $-X$ gate. This would be twice as fast as a 2π-rotation while avoiding a free idling time of the qubit state.

7. Conclusion & Outlook

During the course of this thesis, a cryogenic setup optimised with the goal of measuring semiconductor-based qubit samples was established. Measurement routines, from the initial formation of quantum dots to the universal control of a qubit, were developed and implemented

In collaboration with imec, the formation and operation of electric dipole spin resonance qubits in natural Si/SiGe heterostructures, fully fabricated and grown in a 300 mm industrial semiconductor wafer process line, have been demonstrated. Low charge noise values of $1.4\,\mu eV/\sqrt{Hz}$ and valley splitting energies above 87 µeV were achieved which allows a broad window for qubit operations. Spin relaxation times T_1 exceeding 1 s at external magnetic fields at which the qubit is operated imposes virtually no time constraints on possible qubit manipulation pulses relative to qubit gate times. With the possibility to apply an external magnetic field in all directions, different CoMM geometries were investigated, where the optimal orientation paired with an optimised cryogenic RF-setup, lead to measured qubit Rabi frequencies above 5 MHz, a record value for devices from an industrial foundry [62], and competitive with the best Si/SiGe EDSR devices from academic cleanrooms [55, 131].

Spin coherence times (T_2^* and T_2^{H}) of 1 µs and 50 µs, respectively, were achieved. These coherence times were consistent across four different spin qubit devices from two different 300 mm wafers, and similar values have been observed for spin qubits in natural silicon [109, 191–194]. Nuclear spin fluctuations of ^{29}Si isotopes in natural silicon are known to limit qubit lifetimes, particularly in the low-frequency regime. This becomes when comparing the T_2^* values, which is strongly affected by low-frequency noise, with the T_2^{H} values, where the filter function of the spin-echo scheme makes it robust against low-frequency noise and therefore more sensitive to higher frequencies. Isotopic purification of ^{28}Si in the quantum well is expected to enhance the T_2^* times by at least an order of magnitude, further improving the spin coherence times [62, 191].

Further, with the current coherence times and paired with Rabi frequencies up to 5 MHz, single-qubit gate fidelities of 99.2 % are achieved, determined by randomised benchmarking experiments, and above the surface code error correction threshold. Simulations of the micromagnet's magnetic field gradient suggest that Rabi frequencies above 15 MHz could be feasible with further refinement of the working points and slight RF setup optimisations.

Additional optimisations to further improve single-qubit gate fidelities include advanced manipulation pulse shaping [211], combined with higher microwave output powers, and further micromagnet optimisation in terms of material, geometry and position optimisation for stronger qubit drive gradients and lower dephasing contribution.

In parallel, steps towards the implementation of universal two-qubit logic by exchange coupling of the two adjacent qubits in the current devices is also feasible, when compared to similar demonstrations in laboratory devices [212, 213] and is already actively worked on.

Another advancement would be the implementation of a fast RF readout, which would further increase readout fidelity and reduce total measurement time by orders of magnitude [214–218].

Overall, these results demonstrate the successful operation of state-of-the-art spin qubit devices fabricated using advanced industrial 300 mm wafer process technologies. This progress paves the way for the large-scale optimisation of qubit metrics needed to bring the vision of complex, industrial-grade spin-qubit architectures, and ultimately a universal quantum computer, a step closer to reality. The perfect foundation for an even deeper dive into the vast realms of quantum computing.

A. Appendix

A.1. Qubit performance for other micromagnet gap sizes and field directions

Table A.1 summarises the qubit performance of the four samples presented in this work. Sample D09 Die05 SD15B, which has a 300 nm micromagnet (CoMM) gap, demonstrated behaviour closely matching predictions from simulations. In contrast, samples with micromagnet gap sizes of 400 nm or 650 nm exhibited entirely different behaviour.

Historically, sample D11 Die12 SD10B was measured first. Measurements of the CoMM magnetisation revealed a negative contribution to the externally applied field, raising many questions, as this behaviour could not be explained by the ferromagnetic properties expected for cobalt. Alongside the micromagnet's influence on the external field, qubit performance was analysed, revealing that the qubit drive speed also diverged from simulated predictions. When the external magnetic field was applied in the y-direction, the micromagnet displayed the most significant negative field contribution, yet no coherent qubit manipulations could be performed. Conversely, applying an external field in the z-direction resulted in the lowest magnetic field contribution by the micromagnet, along with the highest Rabi frequencies. This trend was also observed in sample D09 Die13 SD10B, which shares the same CoMM geometry as D11 Die12 SD10B but originates from a different wafer. For D09 Die13 SD10B, only external fields in the z-direction were tested, yielding results very similar to those of D11 Die12 SD10B.

Similarly, sample D09 Die05 SD11B, which has a 400 nm CoMM gap, showed behaviour consistent with the other samples, except a slightly higher negative field contribution and a slightly higher Rabi frequency. However, a completely different behaviour emerged when the CoMM gap was reduced to 300 nm. As previously mentioned, the 300 nm CoMM gap aligns closely with

Table A.1.: Qubit and CoMM characteristics for other samples and external magnetic field directions

Sample	$\vec{B}_{\text{ext}}$ direction	B_{CoMM} (mT)	f_{Rabi} at 23dBm MHz	T_2^* µs	T_2^H µs
D11 Die12 SD10B	x	-76	0.8	0.82	-
650 nm CoMM gap	y	-177	-	-	-
	z	-41	1.3	0.89	50
D09 Die13 SD10B 650 nm gap	z	-33	1.4	1.08	-
D09 Die05 SD11B 400 nm CoMM gap	z	-54	1.6	1.02	-
D09 Die05 SD15B	y	129	5	1.07	51
300 nm CoMM gap	z	8	-	-	-

simulation predictions: with an external magnetic field in the z-direction, the micromagnet's external field contribution was nearly negligible, and coherent manipulations were unachievable. In contrast, applying the field in the y-direction produced the best qubit performance among all samples, in line with the predictions based on micromagnet simulations.

While this behavior could be considered an outlier when reviewing the data from the four presented samples, the findings were confirmed through additional measurements by our group, as well as by independent measurements at imec on samples with the same 300 nm CoMM gap size.

Regarding the qubit coherence times, the measured T_2^* and T_2^{H} times are very consistent over all four samples.

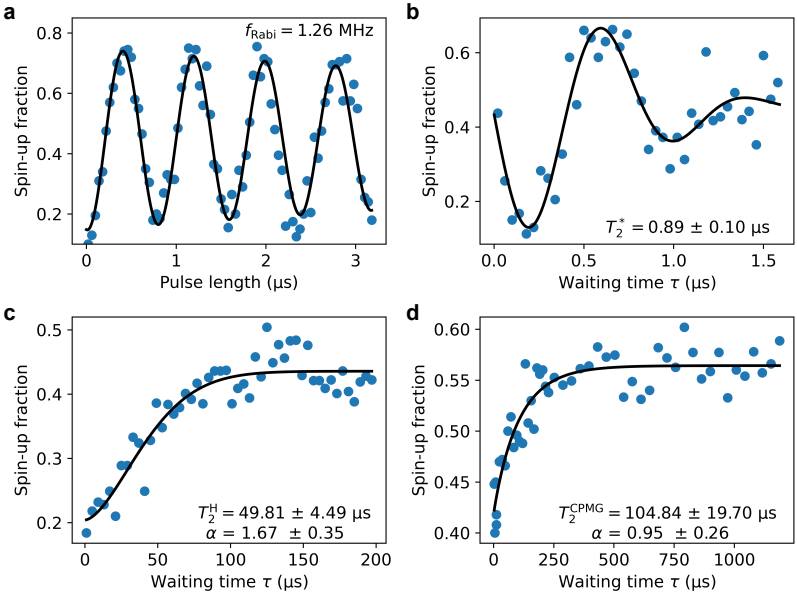

Figure A.1.: Qubit measurements of sample D11 Die12 SD10B, which features a CoMM gap size of 650 nm. All measurements are performed at a microwave output power of 23 dBm and a qubit resonance frequency of ≈ 18.5 GHz. The maximum Rabi frequency of the qubit was achived for an external magnetic field applied in z-direction. **a** Rabi measurement. **b** Ramsey measurement with 1 MHz detuning. **c** Spin echo measurement. **d** CPMG with $n = 3$ π-pulses.

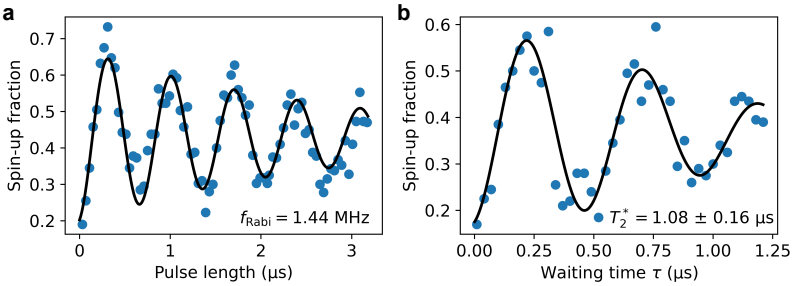

Figure A.2.: Qubit measurements of sample D09 Die13 SD10B, which features a CoMM gap size of 650 nm. All measurements are performed at a microwave output power of 23 dBm and a qubit resonance frequency of ≈ 18.5 GHz. The maximum Rabi frequency of the qubit was achived for an external magnetic field applied in z-direction. **a** Rabi measurement. **b** Ramsey measurement with 2 MHz detuning.

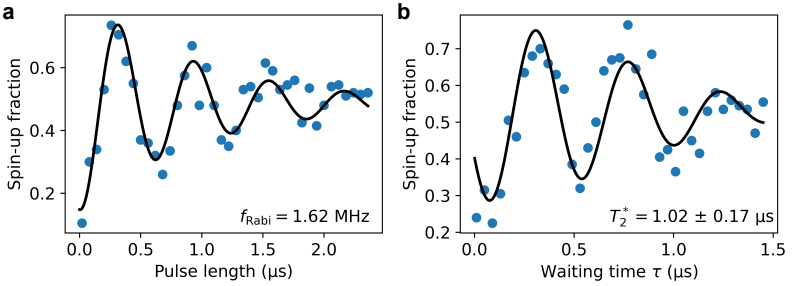

Figure A.3.: Qubit measurements of sample D09 Die05 SD11B, which features a CoMM gap size of 400 nm. All measurements are performed at a microwave output power of 23 dBm and a qubit resonance frequency of ≈ 18.5 GHz. The maximum Rabi frequency of the qubit was achived for an external magnetic field applied in z-direction. **a** Rabi measurement. **b** Ramsey measurement with 2 MHz detuning.

A.2. Superconducting coil parameter

For the work on the spin qubits in this thesis, in addition to the 3D vector magnet, designed and simulated in [145], an additional single big cylindrical coil, and two pairs of helmholtz coils, one big one smaller, were used individually to achieve higher maximum magnetic fields in the respective direction. The ampere to tesla conversion factor of each coil is listed in Table A.2.

Table A.2.: Coil conversion factors and maximum field

Coil	Conversion factor mT/A	Maximum field T
Big zylindrical	242.47	2.5
Big Helmholtz	229.70	1.6
Small Helmholtz	124.60	0.9

Bibliography

[1] Michael A. Nielsen and Isaac L. Chuang. *Quantum Computation and Quantum Information: 10th Anniversary Edition*. Cambridge University Press, 2010. DOI: 10.1017/CBO9780511976667.

[2] John Preskill. "Quantum Computing in the NISQ era and beyond". In: *Quantum* 2 (Aug. 2018), p. 79. DOI: 10.22331/q-2018-08-06-79.

[3] Austin G. Fowler et al. "Surface codes: Towards practical large-scale quantum computation". In: *Phys. Rev. A* 86 (3 Sept. 2012), p. 032324. DOI: 10.1103/PhysRevA.86.032324.

[4] Ryan Babbush et al. "Encoding Electronic Spectra in Quantum Circuits with Linear T Complexity". In: *Phys. Rev. X* 8 (4 Oct. 2018), p. 041015. DOI: 10.1103/PhysRevX.8.041015.

[5] Theodore J. Yoder and Isaac H. Kim. "The surface code with a twist". In: *Quantum* 1 (Apr. 2017), p. 2. DOI: 10.22331/q-2017-04-25-2.

[6] Craig Gidney and Martin Ekerå. "How to factor 2048 bit RSA integers in 8 hours using 20 million noisy qubits". In: *Quantum* 5 (Apr. 2021), p. 433. DOI: 10.22331/q-2021-04-15-433.

[7] Dave Wecker et al. "Gate-count estimates for performing quantum chemistry on small quantum computers". In: *Phys. Rev. A* 90 (2 Aug. 2014), p. 022305. DOI: 10.1103/PhysRevA.90.022305.

[8] Paul Benioff. "The computer as a physical system: A microscopic quantum mechanical Hamiltonian model of computers as represented by Turing machines". In: *Journal of Statistical Physics* 22.5 (May 1980), pp. 563–591. DOI: 10.1007/BF01011339.

[9] Richard P. Feynman. "Simulating physics with computers". In: *International Journal of Theoretical Physics* 21.6 (1982), pp. 467–488. DOI: 10.1007/BF02650179.

[10] Colin P. Williams. *Explorations in Quantum Computing*. Texts in Computer Science. London: Springer London, 2011. DOI: 10.1007/978-1-84628-887-6.

[11] Yudong Cao et al. “Quantum Chemistry in the Age of Quantum Computing”. In: *Chemical Reviews* 119.19 (2019), pp. 10856–10915. DOI: 10.1021/acs.chemrev.8b00803.

[12] Román Orús, Samuel Mugel, and Enrique Lizaso. “Quantum computing for finance: Overview and prospects”. In: *Reviews in Physics* 4 (2019), p. 100028. DOI: 10.1016/j.revip.2019.100028.

[13] Sam McArdle et al. “Quantum computational chemistry”. In: *Rev. Mod. Phys.* 92 (1 2020), p. 015003. DOI: 10.1103/RevModPhys.92.015003.

[14] Anargyros Papageorgiou and Joseph F. Traub. “Measures of quantum computing speedup”. In: *Phys. Rev. A* 88 (2 2013), p. 022316. DOI: 10.1103/PhysRevA.88.022316.

[15] John Preskill. “Quantum Computing in the NISQ era and beyond”. In: *Quantum* 2 (2018), p. 79. DOI: 10.22331/q-2018-08-06-79.

[16] Kishor Bharti et al. “Noisy intermediate-scale quantum algorithms”. In: *Rev. Mod. Phys.* 94 (1 2022), p. 015004. DOI: 10.1103/RevModPhys.94.015004.

[17] Frank Arute et al. “Quantum supremacy using a programmable superconducting processor”. In: *Nature* 574.7779 (Oct. 2019), pp. 505–510. DOI: 10.1038/s41586-019-1666-5.

[18] Youngseok Kim et al. “Evidence for the utility of quantum computing before fault tolerance”. In: *Nature* 618.7965 (Jan. 2023), pp. 500–505. DOI: 10.1038/s41586-023-06096-3.

[19] A. Morvan et al. “Phase transitions in random circuit sampling”. In: *Nature* 634.8033 (Oct. 2024), pp. 328–333. DOI: 10.1038/s41586-024-07998-6.

[20] David P. DiVincenzo. “The Physical Implementation of Quantum Computation”. In: *Fortschritte der Physik* 48.9-11 (2000), pp. 771–783. DOI: 10.1002/1521-3978(200009)48:9/11<771::AID-PROP771>3.0.CO;2-E.

[21] M. H. Devoret and R. J. Schoelkopf. “Superconducting Circuits for Quantum Information: An Outlook”. In: *Science* 339.6124 (2013), pp. 1169–1174. DOI: 10.1126/science.1231930.

[22] Morten Kjaergaard et al. “Superconducting Qubits: Current State of Play”. In: *Annual Review of Condensed Matter Physics* 11.Volume 11, 2020 (2020), pp. 369–395. DOI: https://doi.org/10.1146/annurev-conmatphys-031119-050605.

[23] Chenlu Wang et al. “Towards practical quantum computers: transmon qubit with a lifetime approaching 0.5 milliseconds”. In: *npj Quantum Information* 8.1 (Jan. 2022), p. 3. DOI: 10.1038/s41534-021-00510-2.

[24] Loïc Henriet et al. “Quantum computing with neutral atoms”. In: *Quantum* 4 (Sept. 2020), p. 327. ISSN: 2521-327X. DOI: 10.22331/q-2020-09-21-327.

[25] T. M. Graham et al. “Multi-qubit entanglement and algorithms on a neutral-atom quantum computer”. In: *Nature* 604.7906 (Apr. 2022), pp. 457–462. DOI: 10.1038/s41586-022-04603-6.

[26] Dolev Bluvstein et al. “A quantum processor based on coherent transport of entangled atom arrays”. In: *Nature* 604.7906 (Apr. 2022), pp. 451–456. DOI: 10.1038/s41586-022-04592-6.

[27] H. Häffner, C.F. Roos, and R. Blatt. “Quantum computing with trapped ions”. In: *Physics Reports* 469.4 (2008), pp. 155–203. DOI: https://doi.org/10.1016/j.physrep.2008.09.003.

[28] Colin D. Bruzewicz et al. “Trapped-ion quantum computing: Progress and challenges”. In: *Applied Physics Reviews* 6.2 (May 2019), p. 021314. DOI: 10.1063/1.5088164.

[29] J. M. Pino et al. “Demonstration of the trapped-ion quantum CCD computer architecture”. In: *Nature* 592.7853 (Apr. 2021), pp. 209–213. DOI: 10.1038/s41586-021-03318-4.

[30] Lilian Childress and Ronald Hanson. “Diamond NV centers for quantum computing and quantum networks”. In: *MRS Bulletin* 38.2 (Feb. 2013), pp. 134–138. DOI: 10.1557/mrs.2013.20.

[31] Carlo Bradac et al. “Quantum nanophotonics with group IV defects in diamond”. In: *Nature Communications* 10.1 (Dec. 2019), p. 5625. DOI: 10.1038/s41467-019-13332-w.

[32] Ioannis Karapatzakis et al. “Microwave Control of the Tin-Vacancy Spin Qubit in Diamond with a Superconducting Waveguide”. In: *Phys. Rev. X* 14 (3 Aug. 2024), p. 031036. DOI: 10.1103/PhysRevX.14.031036.

[33] Eufemio Moreno-Pineda et al. “Molecular spin qudits for quantum algorithms”. In: *Chem. Soc. Rev.* 47 (2 2018), pp. 501–513. DOI: 10.1039/C5CS00933B.

[34] Eufemio Moreno-Pineda and Wolfgang Wernsdorfer. "Measuring molecular magnets for quantum technologies". In: *Nature Reviews Physics* 3.9 (Sept. 2021), pp. 645–659. DOI: 10.1038/s42254-021-00340-3.

[35] C. Godfrin et al. "Operating Quantum States in Single Magnetic Molecules: Implementation of Grover's Quantum Algorithm". In: *Phys. Rev. Lett.* 119 (18 Nov. 2017), p. 187702. DOI: 10.1103/PhysRevLett.119.187702.

[36] Guido Burkard et al. "Semiconductor spin qubits". In: *Reviews of Modern Physics* 95.2 (June 2023), p. 025003. DOI: 10.1103/RevModPhys.95.025003.

[37] B. E. Kane. "A silicon-based nuclear spin quantum computer". In: *Nature* 393.6681 (May 1998), pp. 133–137. DOI: 10.1038/30156.

[38] Anasua Chatterjee et al. "Semiconductor qubits in practice". In: *Nature Reviews Physics* 3.3 (Mar. 2021), pp. 157–177. DOI: 10.1038/s42254-021-00283-9.

[39] Jay Gambetta. *The hardware and software for the era of quantum utility is here*. Accessed: 2024-10-29. 2023. URL: https://www.ibm.com/quantum/blog/quantum-roadmap-2033/.

[40] Atom Computing. *Quantum startup Atom Computing first to exceed 1,000 qubits*. Accessed: 2024-10-29. 2023. URL: https://atom-computing.com/quantum-startup-atom-computing-first-to-exceed-1000-qubits/.

[41] Bjoern Lekitsch et al. "Blueprint for a microwave trapped ion quantum computer". In: *Science Advances* 3.2 (2017), e1601540. DOI: 10.1126/sciadv.1601540.

[42] M. Malinowski, D.T.C. Allcock, and C.J. Ballance. "How to Wire a 1000-Qubit Trapped-Ion Quantum Computer". In: *PRX Quantum* 4 (4 Oct. 2023), p. 040313. DOI: 10.1103/PRXQuantum.4.040313.

[43] Petar Jurcevic et al. "Demonstration of quantum volume 64 on a superconducting quantum computing system". In: *Quantum Science and Technology* 6.2 (Mar. 2021), p. 025020. DOI: 10.1088/2058-9565/abe519.

[44] Ruoyu Li et al. "A crossbar network for silicon quantum dot qubits". In: *Science Advances* 4.7 (2018), eaar3960. DOI: 10.1126/sciadv.aar3960.

[45] Lieven M. K. Vandersypen and Mark A. Eriksson. “Quantum computing with semiconductor spins”. In: *Physics Today* 72.8 (Aug. 2019), pp. 38–45. DOI: 10.1063/PT.3.4270.

[46] M. F. Gonzalez-Zalba et al. “Scaling silicon-based quantum computing using CMOS technology”. In: *Nature Electronics* 4.12 (Dec. 2021), pp. 872–884. DOI: 10.1038/s41928-021-00681-y.

[47] Jun Yoneda et al. “A quantum-dot spin qubit with coherence limited by charge noise and fidelity higher than 99.9%”. In: *Nature Nanotechnology* 13.2 (Feb. 2018), pp. 102–106. DOI: 10.1038/s41565-017-0014-x.

[48] X. Xue et al. “Benchmarking Gate Fidelities in a Si / SiGe Two-Qubit Device”. In: *Physical Review X* 9.2 (Apr. 2019), p. 021011. ISSN: 2160-3308. DOI: 10.1103/PhysRevX.9.021011.

[49] W. Huang et al. “Fidelity benchmarks for two-qubit gates in silicon”. In: *Nature* 569.7757 (May 2019), pp. 532–536. DOI: 10.1038/s41586-019-1197-0.

[50] L. Petit et al. “Universal quantum logic in hot silicon qubits”. In: *Nature* 580.7803 (Apr. 2020), pp. 355–359. DOI: 10.1038/s41586-020-2170-7.

[51] Keiji Ono, Takahiro Mori, and Satoshi Moriyama. “High-temperature operation of a silicon qubit”. In: *Scientific Reports* 9.1 (Jan. 2019), p. 469. DOI: 10.1038/s41598-018-36476-z.

[52] Brennan Undseth et al. “Hotter is Easier: Unexpected Temperature Dependence of Spin Qubit Frequencies”. In: *Physical Review X* 13.4 (Oct. 2023), p. 041015. DOI: 10.1103/PhysRevX.13.041015.

[53] Jonathan Y. Huang et al. “High-fidelity spin qubit operation and algorithmic initialization above 1 K”. In: *Nature* 627.8005 (Mar. 2024), pp. 772–777. DOI: 10.1038/s41586-024-07160-2.

[54] Leon C. Camenzind et al. “A hole spin qubit in a fin field-effect transistor above 4 kelvin”. In: *Nature Electronics* 5.3 (Mar. 2022), pp. 178–183. DOI: 10.1038/s41928-022-00722-0.

[55] Stephan G. J. Philips et al. “Universal control of a six-qubit quantum processor in silicon”. In: *Nature* 609.7929 (Sept. 2022), pp. 919–924. DOI: 10.1038/s41586-022-05117-x.

[56] Nico W. Hendrickx et al. “A four-qubit germanium quantum processor”. In: *Nature* 591.7851 (Mar. 2021), pp. 580–585. DOI: 10.1038/s41586-021-03332-6.

[57] J. Reiner et al. “High-fidelity initialization and control of electron and nuclear spins in a four-qubit register”. In: *Nature Nanotechnology* 19.5 (May 2024), pp. 605–611. DOI: 10.1038/s41565-023-01596-9.

[58] Kamil Rocki et al. *Fast Stencil-Code Computation on a Wafer-Scale Processor*. 2020. arXiv: 2010.03660.

[59] R. Maurand et al. “A CMOS silicon spin qubit”. In: *Nature Communications* 7.1 (Nov. 2016), p. 13575. DOI: 10.1038/ncomms13575.

[60] A. M. J. Zwerver et al. “Qubits made by advanced semiconductor manufacturing”. In: *Nature Electronics* 5.3 (Mar. 2022), pp. 184–190. DOI: 10.1038/s41928-022-00727-9.

[61] Bernhard Klemt et al. “Electrical manipulation of a single electron spin in CMOS using a micromagnet and spin-valley coupling”. In: *npj Quantum Information* 9.1 (Oct. 2023), p. 107. DOI: 10.1038/s41534-023-00776-8.

[62] Samuel Neyens et al. “Probing single electrons across 300-mm spin qubit wafers”. In: *Nature* 629.8010 (May 2024), pp. 80–85. DOI: 10.1038/s41586-024-07275-6.

[63] Robert Raussendorf and Jim Harrington. “Fault-Tolerant Quantum Computation with High Threshold in Two Dimensions”. In: *Phys. Rev. Lett.* 98 (19 May 2007), p. 190504. DOI: 10.1103/PhysRevLett.98.190504.

[64] L. M. K. Vandersypen et al. “Interfacing spin qubits in quantum dots and donors—hot, dense, and coherent”. In: *npj Quantum Information* 3.1 (Sept. 2017), p. 34. DOI: 10.1038/s41534-017-0038-y.

[65] Jurgen Dijkema et al. *Two-qubit logic between distant spins in silicon*. arXiv:2310.16805 [cond-mat, physics:quant-ph]. Oct. 2023.

[66] L. Childress, A. S. Sørensen, and M. D. Lukin. “Mesoscopic cavity quantum electrodynamics with quantum dots”. In: *Phys. Rev. A* 69 (4 Apr. 2004), p. 042302. DOI: 10.1103/PhysRevA.69.042302.

[67] Guido Burkard and Atac Imamoglu. “Ultra-long-distance interaction between spin qubits”. In: *Phys. Rev. B* 74 (4 July 2006), p. 041307. DOI: 10.1103/PhysRevB.74.041307.

[68] Xuedong Hu, Yu-xi Liu, and Franco Nori. “Strong coupling of a spin qubit to a superconducting stripline cavity”. In: *Phys. Rev. B* 86 (3 July 2012), p. 035314. DOI: 10.1103/PhysRevB.86.035314. URL: https://link.aps.org/doi/10.1103/PhysRevB.86.035314.

[69] Inga Seidler et al. “Conveyor-mode single-electron shuttling in Si/SiGe for a scalable quantum computing architecture”. In: *npj Quantum Information* 8.1 (Aug. 2022), p. 100. DOI: 10.1038/s41534-022-00615-2.

[70] Veit Langrock et al. “Blueprint of a Scalable Spin Qubit Shuttle Device for Coherent Mid-Range Qubit Transfer in Disordered Si/SiGe/SiO_2”. In: *PRX Quantum* 4 (2 Apr. 2023), p. 020305. DOI: 10.1103/PRXQuantum.4.020305.

[71] Matthias Künne et al. “The SpinBus architecture for scaling spin qubits with electron shuttling”. In: *Nature Communications* 15.1 (June 2024), p. 4977. DOI: 10.1038/s41467-024-49182-4.

[72] Takafumi Fujita et al. “Coherent shuttle of electron-spin states”. In: *npj Quantum Information* 3.1 (June 2017), p. 22. DOI: 10.1038/s41534-017-0024-4.

[73] R. K. Puddy et al. “Multiplexed charge-locking device for large arrays of quantum devices”. In: *Applied Physics Letters* 107.14 (Oct. 2015), p. 143501. DOI: 10.1063/1.4932012.

[74] M. Veldhorst et al. “Silicon CMOS architecture for a spin-based quantum computer”. In: *Nature Communications* 8.1 (Dec. 2017), p. 1766. DOI: 10.1038/s41467-017-01905-6.

[75] Timothy Alexander Baart et al. “Coherent spin-exchange via a quantum mediator”. In: *Nature Nanotechnology* 12.1 (Jan. 2017), pp. 26–30. DOI: 10.1038/nnano.2016.188.

[76] Federico Fedele et al. “Simultaneous Operations in a Two-Dimensional Array of Singlet-Triplet Qubits”. In: *PRX Quantum* 2 (4 Oct. 2021), p. 040306. DOI: 10.1103/PRXQuantum.2.040306.

[77] M. D. Shulman et al. “Demonstration of Entanglement of Electrostatically Coupled Singlet-Triplet Qubits”. In: *Science* 336.6078 (2012), pp. 202–205. DOI: 10.1126/science.1217692.

[78] Ran Xue et al. “Si/SiGe QuBus for single electron information-processing devices with memory and micron-scale connectivity function”. In: *Nature Communications* 15.1 (Mar. 2024), p. 2296. DOI: 10.1038/s41467-024-46519-x.

[79] Patrick Harvey-Collard et al. “Coherent Spin-Spin Coupling Mediated by Virtual Microwave Photons”. In: *Phys. Rev. X* 12 (2 May 2022), p. 021026. DOI: 10.1103/PhysRevX.12.021026.

[80] Guido Burkard et al. “Superconductor–semiconductor hybrid-circuit quantum electrodynamics”. In: *Nature Reviews Physics* 2.3 (Mar. 2020), pp. 129–140. DOI: 10.1038/s42254-019-0135-2.

[81] Floor van Riggelen-Doelman et al. “Coherent spin qubit shuttling through germanium quantum dots”. In: *Nature Communications* 15.1 (July 2024), p. 5716. DOI: 10.1038/s41467-024-49358-y.

[82] Mats Volmer et al. “Mapping of valley splitting by conveyor-mode spin-coherent electron shuttling”. In: *npj Quantum Information* 10.1 (June 2024), p. 61. DOI: 10.1038/s41534-024-00852-7.

[83] Akito Noiri et al. “A shuttling-based two-qubit logic gate for linking distant silicon quantum processors”. In: *Nature Communications* 13.1 (Sept. 2022), p. 5740. DOI: 10.1038/s41467-022-33453-z.

[84] Maxim De Smet et al. *High-fidelity single-spin shuttling in silicon*. arXiv:2406.07267 [cond-mat, physics:quant-ph]. June 2024.

[85] Francesco Borsoi et al. “Shared control of a 16 semiconductor quantum dot crossbar array”. In: *Nature Nanotechnology* 19.1 (Jan. 2024), pp. 21–27. DOI: 10.1038/s41565-023-01491-3.

[86] Xin Zhang et al. “Universal control of four singlet–triplet qubits”. In: *Nature Nanotechnology* (Oct. 2024). DOI: 10.1038/s41565-024-01817-9.

[87] Daniel Loss and David P. DiVincenzo. “Quantum computation with quantum dots”. In: *Phys. Rev. A* 57 (1 Jan. 1998), pp. 120–126. DOI: 10.1103/PhysRevA.57.120.

[88] J. M. Taylor et al. “Fault-tolerant architecture for quantum computation using electrically controlled semiconductor spins”. In: *Nature Physics* 1.3 (Dec. 2005), pp. 177–183. DOI: 10.1038/nphys174.

[89] L. C. L. Hollenberg et al. “Two-dimensional architectures for donor-based quantum computing”. In: *Phys. Rev. B* 74 (4 July 2006), p. 045311. DOI: 10.1103/PhysRevB.74.045311.

[90] Mark Friesen et al. “Efficient Multiqubit Entanglement via a Spin Bus”. In: *Phys. Rev. Lett.* 98 (23 June 2007), p. 230503. DOI: 10.1103/PhysRevLett.98.230503.

[91] Björn Trauzettel et al. “Spin qubits in graphene quantum dots”. In: *Nature Physics* 3.3 (Mar. 2007), pp. 192–196. DOI: 10.1038/nphys544.

[92] R. P. G. McNeil et al. “On-demand single-electron transfer between distant quantum dots”. In: *Nature* 477.7365 (Sept. 2011), pp. 439–442. DOI: 10.1038/nature10444.

[93] Sylvain Hermelin et al. “Electrons surfing on a sound wave as a platform for quantum optics with flying electrons”. In: *Nature* 477.7365 (Sept. 2011), pp. 435–438. DOI: 10.1038/nature10416.

[94] Luka Trifunovic et al. “Long-Distance Spin-Spin Coupling via Floating Gates”. In: *Phys. Rev. X* 2 (1 Jan. 2012), p. 011006. DOI: 10.1103/PhysRevX.2.011006.

[95] K. D. Petersson et al. “Circuit quantum electrodynamics with a spin qubit”. In: *Nature* 490.7420 (Oct. 2012), pp. 380–383. DOI: 10.1038/nature11559.

[96] Martin Leijnse and Karsten Flensberg. “Coupling Spin Qubits via Superconductors”. In: *Phys. Rev. Lett.* 111 (6 Aug. 2013), p. 060501. DOI: 10.1103/PhysRevLett.111.060501.

[97] Luka Trifunovic, Fabio L. Pedrocchi, and Daniel Loss. “Long-Distance Entanglement of Spin Qubits via Ferromagnet”. In: *Phys. Rev. X* 3 (4 Dec. 2013), p. 041023. DOI: 10.1103/PhysRevX.3.041023.

[98] J. J. Viennot et al. “Coherent coupling of a single spin to microwave cavity photons”. In: *Science* 349.6246 (2015), pp. 408–411. DOI: 10.1126/science.aaa3786.

[99] M. J. A. Schuetz et al. “Universal Quantum Transducers Based on Surface Acoustic Waves”. In: *Phys. Rev. X* 5 (3 Sept. 2015), p. 031031. DOI: 10.1103/PhysRevX.5.031031.

[100] Fabian Hassler, Gianluigi Catelani, and Hendrik Bluhm. “Exchange interaction of two spin qubits mediated by a superconductor”. In: *Phys. Rev. B* 92 (23 Dec. 2015), p. 235401. DOI: 10.1103/PhysRevB.92.235401.

[101] Charles D. Hill et al. “A surface code quantum computer in silicon”. In: *Science Advances* 1.9 (2015), e1500707. DOI: 10.1126/sciadv.1500707.

[102] Peter Stano et al. “Fast long-distance control of spin qubits by photon-assisted cotunneling”. In: *Phys. Rev. B* 92 (7 Aug. 2015), p. 075302. DOI: 10.1103/PhysRevB.92.075302.

[103] V. Srinivasa, H. Xu, and J. M. Taylor. “Tunable Spin-Qubit Coupling Mediated by a Multielectron Quantum Dot”. In: *Phys. Rev. Lett.* 114 (22 June 2015), p. 226803. DOI: 10.1103/PhysRevLett.114.226803.

[104] T. A. Baart et al. “Single-spin CCD”. In: *Nature Nanotechnology* 11.4 (Apr. 2016), pp. 330–334. DOI: 10.1038/nnano.2015.291.

[105] Guilherme Tosi et al. “Silicon quantum processor with robust long-distance qubit couplings”. In: *Nature Communications* 8.1 (Sept. 2017), p. 450. DOI: 10.1038/s41467-017-00378-x.

[106] G. Pica et al. “Surface code architecture for donors and dots in silicon with imprecise and nonuniform qubit couplings”. In: *Phys. Rev. B* 93 (3 Jan. 2016), p. 035306. DOI: 10.1103/PhysRevB.93.035306.

[107] Joe O’Gorman et al. “A silicon-based surface code quantum computer”. In: *npj Quantum Information* 2.1 (Feb. 2016), p. 15019. DOI: 10.1038/npjqi.2015.19.

[108] Paul Steinacker et al. *A 300 mm foundry silicon spin qubit unit cell exceeding 99% fidelity in all operations*. 2024. arXiv: 2410.15590.

[109] Hubert C. George et al. *12-spin-qubit arrays fabricated on a 300 mm semiconductor manufacturing line*. 2024. arXiv: 2410.16583.

[110] Chiao-Ti Huang et al. “Screening of remote charge scattering sites from the oxide/silicon interface of strained Si two-dimensional electron gases by an intermediate tunable shielding electron layer”. In: *Applied Physics Letters* 104.24 (June 2014), p. 243510. DOI: 10.1063/1.4884650.

[111] D. M. Fleetwood et al. “Effects of oxide traps, interface traps, and “border traps” on metal-oxide-semiconductor devices”. In: *Journal of Applied Physics* 73.10 (May 1993), pp. 5058–5074. DOI: 10.1063/1.353777.

[112] Friedrich Schäffler. “High-mobility Si and Ge structures”. In: *Semiconductor Science and Technology* 12.12 (Dec. 1997), p. 1515. DOI: 10.1088/0268-1242/12/12/001.

[113] P. Dutta and P. M. Horn. “Low-frequency fluctuations in solids: 1 f noise”. In: *Reviews of Modern Physics* 53.3 (July 1981), pp. 497–516. DOI: 10.1103/RevModPhys.53.497.

[114] Jiun-Yun Li et al. “Extremely high electron mobility in isotopically-enriched 28Si two-dimensional electron gases grown by chemical vapor deposition”. In: *Applied Physics Letters* 103.16 (Oct. 2013), p. 162105. DOI: 10.1063/1.4824729.

[115] T N Camenzind et al. “High mobility SiMOSFETs fabricated in a full 300 mm CMOS process”. In: *Materials for Quantum Technology* 1.4 (Dec. 2021), p. 041001. DOI: 10.1088/2633-4356/ac40f4.

[116] M. Mohamed El Kordy Shehata et al. “Modeling semiconductor spin qubits and their charge noise environment for quantum gate fidelity estimation”. In: *Phys. Rev. B* 108 (4 July 2023), p. 045305. DOI: 10.1103/PhysRevB.108.045305.

[117] Elliot J. Connors et al. “Low-frequency charge noise in Si/SiGe quantum dots”. In: *Phys. Rev. B* 100 (16 Oct. 2019), p. 165305. DOI: 10.1103/PhysRevB.100.165305.

[118] Elliot J. Connors et al. “Charge-noise spectroscopy of Si/SiGe quantum dots via dynamically-decoupled exchange oscillations”. In: *Nature Communications* 13.1 (Feb. 2022), p. 940. DOI: 10.1038/s41467-022-28519-x.

[119] Julian Ferrero et al. “Noise reduction by bias cooling in gated Si/SiGe quantum dots”. In: *Applied Physics Letters* 124.20 (May 2024), p. 204002. DOI: 10.1063/5.0206632.

[120] Hendrik Bluhm et al. “Dephasing time of GaAs electron-spin qubits coupled to a nuclear bath exceeding 200 μs”. In: *Nature Physics* 7.2 (Feb. 2011), pp. 109–113. DOI: 10.1038/nphys1856.

[121] Benjamin Joecker et al. “Transfer of a quantum state from a photonic qubit to a gate-defined quantum dot”. In: *Phys. Rev. B* 99 (20 May 2019), p. 205415. DOI: 10.1103/PhysRevB.99.205415.

[122] Pascal Cerfontaine et al. “High-Fidelity Single-Qubit Gates for Two-Electron Spin Qubits in GaAs”. In: *Phys. Rev. Lett.* 113 (15 Oct. 2014), p. 150501. DOI: 10.1103/PhysRevLett.113.150501.

[123] Pascal Cerfontaine et al. “Closed-loop control of a GaAs-based singlet-triplet spin qubit with 99.5% gate fidelity and low leakage”. In: *Nature Communications* 11.1 (Aug. 2020), p. 4144. DOI: 10.1038/s41467-020-17865-3.

[124] Kevin J. R. Rosman and P. D. P. Taylor. “Isotopic compositions of the elements 1997 (Technical Report)”. In: *Pure and Applied Chemistry* 70.1 (1998), pp. 217–235. DOI: 10.1351/pac199870010217.

[125] S.M. Sze and K.K Ng. “Physics and Properties of Semiconductors—A Review”. In: *Physics of Semiconductor Devices*. John Wiley & Sons, Ltd, 2006, pp. 5–75. DOI: 10.1002/9780470068328.ch1.

[126] Martin A. Green. "Intrinsic concentration, effective densities of states, and effective mass in silicon". In: *Journal of Applied Physics* 67.6 (Mar. 1990), pp. 2944–2954. DOI: 10.1063/1.345414.

[127] Floris A. Zwanenburg et al. "Silicon quantum electronics". In: *Reviews of Modern Physics* 85.3 (July 2013), pp. 961–1019. DOI: 10.1103/RevModPhys.85.961.

[128] Amin Hosseinkhani and Guido Burkard. "Electromagnetic control of valley splitting in ideal and disordered Si quantum dots". In: *Physical Review Research* 2.4 (Nov. 2020), p. 043180. DOI: 10.1103/PhysRevResearch.2.043180.

[129] Jonas R. F. Lima and Guido Burkard. "Valley splitting depending on the size and location of a silicon quantum dot". In: *Phys. Rev. Mater.* 8 (3 Mar. 2024), p. 036202. DOI: 10.1103/PhysRevMaterials.8.036202.

[130] F. K. Unseld et al. "A 2D quantum dot array in planar 28Si/SiGe". In: *Applied Physics Letters* 123.8 (Aug. 2023), p. 084002. DOI: 10.1063/5.0160847.

[131] Akito Noiri et al. "Fast universal quantum gate above the fault-tolerance threshold in silicon". In: *Nature* 601.7893 (Jan. 2022), pp. 338–342. DOI: 10.1038/s41586-021-04182-y.

[132] Richard P. Feynman, Jr. Vernon Frank L., and Robert W. Hellwarth. "Geometrical Representation of the Schrödinger Equation for Solving Maser Problems". In: *Journal of Applied Physics* 28.1 (Jan. 1957), pp. 49–52. DOI: 10.1063/1.1722572.

[133] F. Bloch. "Nuclear Induction". In: *Phys. Rev.* 70 (7-8 Oct. 1946), pp. 460–474. DOI: 10.1103/PhysRev.70.460.

[134] W. Pauli. "Über den Zusammenhang des Abschlusses der Elektronengruppen im Atom mit der Komplexstruktur der Spektren". In: *Zeitschrift für Physik* 31.1 (Feb. 1925), pp. 765–783. DOI: 10.1007/BF02980631.

[135] R. Shankar. *Principles of Quantum Mechanics*. 2nd. New York: Springer, 1994. ISBN: 978-0306447907.

[136] J. R. Petta et al. "Coherent Manipulation of Coupled Electron Spins in Semiconductor Quantum Dots". In: *Science* 309.5744 (2005), pp. 2180–2184. DOI: 10.1126/science.1116955.

[137] K. C. Nowack et al. “Single-Shot Correlations and Two-Qubit Gate of Solid-State Spins”. In: *Science* 333.6047 (2011), pp. 1269–1272. DOI: 10.1126/science.1209524.

[138] M. Veldhorst et al. “A two-qubit logic gate in silicon”. In: *Nature* 526.7573 (Oct. 2015), pp. 410–414. DOI: 10.1038/nature15263.

[139] Thomas Koch et al. *Industrial 300 mm wafer processed spin qubits in natural silicon/silicon-germanium*. 2024. arXiv: 2409.12731.

[140] M. Pioro-Ladrière et al. “Electrically driven single-electron spin resonance in a slanting Zeeman field”. In: *Nature Physics* 4.10 (Oct. 2008), pp. 776–779. DOI: 10.1038/nphys1053.

[141] E. I. Rashba. “Properties of semiconductors with an extremum loop: I. Cyclotron and combinational resonance in a magnetic field perpendicular to the plane of the loop”. In: *Sov. Phys.-Solid State* 2 (1960), pp. 1109–1122.

[142] N. I. Dumoulin Stuyck et al. “Low dephasing and robust micromagnet designs for silicon spin qubits”. In: *Applied Physics Letters* 119.9 (Aug. 2021), p. 094001. DOI: 10.1063/5.0059939.

[143] Alexander Zilz. *Investigation of the Rarefied Gas Flow in the Pumping Tube of a 3He/4He Dilution Refrigerator*. Master’s thesis. 2022.

[144] Aljoscha Auer. “Interfacing nanomechanics with multi-gated suspended carbon nanotube quantum circuits”. PhD thesis. Karlsruhe Institute of Technology, 2024.

[145] Julian Ferrero. “Development of a cryogenic platform with fast turnaround in-situ characterization of semiconductor circuits for qubit applications”. PhD thesis. Karlsruhe Institute of Technology, 2024.

[146] Marki Microwave. *IQ, Image Reject, and Single-Sideband Mixers*. https://markimicrowave.com/technical-resources/application-notes/iq-image-reject-and-single-sideband-mixers/. Accessed: 2024-10-22. 2013.

[147] Marki Microwave. *How to think about IQ mixers*. https://markimicrowave.com/technical-resources/application-notes/how-to-think-about-iq-mixers/. Accessed: 2024-10-23. 2015.

[148] C Rössler et al. “Gating of high-mobility two-dimensional electron gases in GaAs/AlGaAs heterostructures”. In: *New Journal of Physics* 12.4 (2010), p. 043007. DOI: 10.1088/1367-2630/12/4/043007.

[149] Chiao-Ti Huang, Jiun-Yun Li, and James C. Sturm. "Very Low Electron Density in Undoped Enhancement-Mode Si/SiGe Two-Dimensional Electron Gases with Thin SiGe Cap Layers". In: *ECS Transactions* 53.3 (2013), p. 45. DOI: 10.1149/05303.0045ecst.

[150] R. Hanson et al. "Spins in few-electron quantum dots". In: *Rev. Mod. Phys.* 79 (4 2007), pp. 1217–1265. DOI: 10.1103/RevModPhys.79.1217.

[151] H. Van Houten, C. W. J. Beenakker, and A. A. M. Staring. "Coulomb-Blockade Oscillations in Semiconductor Nanostructures". In: *Single Charge Tunneling: Coulomb Blockade Phenomena In Nanostructures*. Ed. by Hermann Grabert and Michel H. Devoret. Boston, MA: Springer US, 1992, pp. 167–216. DOI: 10.1007/978-1-4757-2166-9_5.

[152] Leo P. Kouwenhoven et al. "Electron Transport in Quantum Dots". In: *Mesoscopic Electron Transport*. Ed. by Lydia L. Sohn, Leo P. Kouwenhoven, and Gerd Schön. Dordrecht: Springer Netherlands, 1997, pp. 105–214. DOI: 10.1007/978-94-015-8839-3_4.

[153] L P Kouwenhoven, D G Austing, and S Tarucha. "Few-electron quantum dots". In: *Reports on Progress in Physics* 64.6 (2001), p. 701. DOI: 10.1088/0034-4885/64/6/201.

[154] D. Maradan et al. "GaAs Quantum Dot Thermometry Using Direct Transport and Charge Sensing". In: *Journal of Low Temperature Physics* 175.5 (2014), pp. 784–798.

[155] Peihao Huang, Neil M. Zimmerman, and Garnett W. Bryant. "Spin decoherence in a two-qubit CPHASE gate: the critical role of tunneling noise". In: *npj Quantum Information* 4.1 (Nov. 2018), p. 62. DOI: 10.1038/s41534-018-0112-0.

[156] Tom Struck et al. "Low-frequency spin qubit energy splitting noise in highly purified 28Si/SiGe". In: *npj Quantum Information* 6.1 (May 2020), p. 40. DOI: 10.1038/s41534-020-0276-2.

[157] Brian Paquelet Wuetz et al. "Reducing charge noise in quantum dots by using thin silicon quantum wells". In: *Nature Communications* 14.1 (Mar. 2023), p. 1385. DOI: 10.1038/s41467-023-36951-w.

[158] A. Elsayed et al. "Low charge noise quantum dots with industrial CMOS manufacturing". In: *npj Quantum Information* 10 (July 2024), p. 70. DOI: 10.1038/s41534-024-00864-3.

[159] Cameron Spence et al. “Probing Low-Frequency Charge Noise in Few-Electron CMOS Quantum Dots”. In: *Phys. Rev. Appl.* 19 (4 Apr. 2023), p. 044010. DOI: 10.1103/PhysRevApplied.19.044010.

[160] H. Nyquist. “Certain Topics in Telegraph Transmission Theory”. In: *Transactions of the American Institute of Electrical Engineers* 47.2 (1928), pp. 617–644. DOI: 10.1109/T-AIEE.1928.5055024.

[161] C.E. Shannon. “Communication in the Presence of Noise”. In: *Proceedings of the IRE* 37.1 (1949), pp. 10–21. DOI: 10.1109/JRPROC.1949.232969.

[162] P. Welch. “The use of fast Fourier transform for the estimation of power spectra: A method based on time averaging over short, modified periodograms”. In: *IEEE Transactions on Audio and Electroacoustics* 15.2 (June 1967), pp. 70–73. DOI: 10.1109/TAU.1967.1161901.

[163] Clemens Müller, Jared H Cole, and Jürgen Lisenfeld. “Towards understanding two-level-systems in amorphous solids: insights from quantum circuits”. In: *Reports on Progress in Physics* 82.12 (Oct. 2019), p. 124501. DOI: 10.1088/1361-6633/ab3a7e.

[164] Dimitrie Culcer, Xuedong Hu, and S. Das Sarma. “Dephasing of Si spin qubits due to charge noise”. In: *Applied Physics Letters* 95.7 (Aug. 2009), p. 073102. DOI: 10.1063/1.3194778.

[165] Adam Bermeister, Daniel Keith, and Dimitrie Culcer. “Charge noise, spin-orbit coupling, and dephasing of single-spin qubits”. In: *Applied Physics Letters* 105.19 (Nov. 2014), p. 192102. DOI: 10.1063/1.4901162.

[166] Dimitrie Culcer and Neil M. Zimmerman. “Dephasing of Si singlet-triplet qubits due to charge and spin defects”. In: *Applied Physics Letters* 102.23 (June 2013), p. 232108. DOI: 10.1063/1.4810911.

[167] E. Paladino et al. “1 / f noise: Implications for solid-state quantum information”. In: *Reviews of Modern Physics* 86.2 (Apr. 2014), pp. 361–418. DOI: 10.1103/RevModPhys.86.361.

[168] Stefan Machlup. “Noise in Semiconductors: Spectrum of a Two-Parameter Random Signal”. In: *Journal of Applied Physics* 25.3 (Mar. 1954), pp. 341–343. DOI: 10.1063/1.1721637.

[169] W. G. van der Wiel et al. “Electron transport through double quantum dots”. In: *Rev. Mod. Phys.* 75 (1 Dec. 2002), pp. 1–22. DOI: 10.1103/RevModPhys.75.1.

[170] Arne Hollmann et al. “Large, Tunable Valley Splitting and Single-Spin Relaxation Mechanisms in a Si / Si Ge Quantum Dot”. In: *Physical Review Applied* 13.3 (Mar. 2020), p. 034068. DOI: 10.1103/PhysRevApplied.13.034068.

[171] Brian Paquelet Wuetz et al. “Atomic fluctuations lifting the energy degeneracy in Si/SiGe quantum dots”. In: *Nature Communications* 13.1 (Dec. 2022), p. 7730. DOI: 10.1038/s41467-022-35458-0.

[172] J. M. Elzerman et al. “Single-shot read-out of an individual electron spin in a quantum dot”. In: *Nature* 430.6998 (July 2004), pp. 431–435. DOI: 10.1038/nature02693.

[173] C. H. Yang et al. “Spin-valley lifetimes in a silicon quantum dot with tunable valley splitting”. In: *Nature Communications* 4.1 (June 2013), p. 2069. DOI: 10.1038/ncomms3069.

[174] L. Petit et al. “Spin Lifetime and Charge Noise in Hot Silicon Quantum Dot Qubits”. In: *Physical Review Letters* 121.7 (Aug. 2018), p. 076801. DOI: 10.1103/PhysRevLett.121.076801.

[175] F. Borjans et al. “Single-Spin Relaxation in a Synthetic Spin-Orbit Field”. In: *Physical Review Applied* 11.4 (Apr. 2019), p. 044063. DOI: 10.1103/PhysRevApplied.11.044063.

[176] Peihao Huang and Xuedong Hu. “Spin relaxation in a Si quantum dot due to spin-valley mixing”. In: *Phys. Rev. B* 90 (Dec. 2014), p. 235315. DOI: 10.1103/PhysRevB.90.235315.

[177] Thomas McJunkin et al. “Valley splittings in Si/SiGe quantum dots with a germanium spike in the silicon well”. In: *Phys. Rev. B* 104 (8 Aug. 2021), p. 085406. DOI: 10.1103/PhysRevB.104.085406.

[178] Yi Feng and Robert Joynt. “Enhanced valley splitting in Si layers with oscillatory Ge concentration”. In: *Phys. Rev. B* 106 (8 Aug. 2022), p. 085304. DOI: 10.1103/PhysRevB.106.085304.

[179] Merritt P. Losert et al. “Practical strategies for enhancing the valley splitting in Si/SiGe quantum wells”. In: *Phys. Rev. B* 108 (12 Sept. 2023), p. 125405. DOI: 10.1103/PhysRevB.108.125405.

[180] Benjamin D. Woods et al. “Coupling conduction-band valleys in SiGe heterostructures via shear strain and Ge concentration oscillations”. In: *npj Quantum Information* 10.1 (May 2024), p. 54. DOI: 10.1038/s41534-024-00853-6.

[181] T. Takakura et al. “Triple quantum dot device designed for three spin qubits”. In: *Applied Physics Letters* 97.21 (Nov. 2010), p. 212104. DOI: 10.1063/1.3518919.

[182] R. Neumann and L. R. Schreiber. “Simulation of micro-magnet stray-field dynamics for spin qubit manipulation”. In: *Journal of Applied Physics* 117.19 (May 2015), p. 193903. DOI: 10.1063/1.4921291.

[183] D. M. Zajac et al. “Resonantly driven CNOT gate for electron spins”. In: *Science* 359.6374 (2018), pp. 439–442. DOI: 10.1126/science.aao5965.

[184] M. Shafiei et al. “Resolving Spin-Orbit- and Hyperfine-Mediated Electric Dipole Spin Resonance in a Quantum Dot”. In: *Phys. Rev. Lett.* 110 (10 Mar. 2013), p. 107601. DOI: 10.1103/PhysRevLett.110.107601.

[185] Kehui Li, David C. Spierings, and Aephraim M. Steinberg. “Efficient adiabatic rapid passage in the presence of noise”. In: *Phys. Rev. A* 108 (1 July 2023), p. 012615. DOI: 10.1103/PhysRevA.108.012615.

[186] A. Abragam. *The Principles of Nuclear Magnetism*. International series of monographs on physics. Clarendon Press, 1961. ISBN: 9780198520146.

[187] S.N. Shevchenko, S. Ashhab, and Franco Nori. “Landau–Zener–Stückelberg interferometry”. In: *Physics Reports* 492.1 (2010), pp. 1–30. DOI: 10.1016/j.physrep.2010.03.002.

[188] Clarence Zener and Ralph Howard Fowler. “Non-adiabatic crossing of energy levels”. In: *Proceedings of the Royal Society of London. Series A, Containing Papers of a Mathematical and Physical Character* 137.833 (1932), pp. 696–702. DOI: 10.1098/rspa.1932.0165.

[189] Daniel Keith et al. “Ramped measurement technique for robust high-fidelity spin qubit readout”. In: *Science Advances* 8.36 (2022), eabq0455. DOI: 10.1126/sciadv.abq0455.

[190] E. Kawakami et al. “Electrical control of a long-lived spin qubit in a Si/SiGe quantum dot”. In: *Nature Nanotechnology* 9.9 (Sept. 2014), pp. 666–670. DOI: 10.1038/nnano.2014.153.

[191] Peter Stano and Daniel Loss. “Review of performance metrics of spin qubits in gated semiconducting nanostructures”. In: *Nature Reviews Physics* 4.10 (Aug. 2022), pp. 672–688. DOI: 10.1038/s42254-022-00484-w.

[192] Lucy V. C. Assali et al. “Hyperfine interactions in silicon quantum dots”. In: *Phys. Rev. B* 83 (16 Apr. 2011), p. 165301. DOI: 10.1103/PhysRevB.83.165301.

[193] T. F. Watson et al. "A programmable two-qubit quantum processor in silicon". In: *Nature* 555.7698 (Mar. 2018), pp. 633–637. DOI: 10.1038/nature25766.

[194] Kenta Takeda et al. "A fault-tolerant addressable spin qubit in a natural silicon quantum dot". In: *Science Advances* 2.8 (2016), e1600694. DOI: 10.1126/sciadv.1600694.

[195] I. I. Rabi et al. "The Molecular Beam Resonance Method for Measuring Nuclear Magnetic Moments. The Magnetic Moments of $_3Li^6$, $_3Li^7$ and $_9F^{19}$". In: *Phys. Rev.* 55 (6 Mar. 1939), pp. 526–535. DOI: 10.1103/PhysRev.55.526.

[196] Michel Le Bellac. *A Short Introduction to Quantum Information and Quantum Computation*. Cambridge University Press, 2006. ISBN: 9780511755361.

[197] Brennan Undseth et al. "Nonlinear Response and Crosstalk of Electrically Driven Silicon Spin Qubits". In: *Phys. Rev. Appl.* 19 (Apr. 2023), p. 044078. DOI: 10.1103/PhysRevApplied.19.044078.

[198] J. Yoneda et al. "Fast Electrical Control of Single Electron Spins in Quantum Dots with Vanishing Influence from Nuclear Spins". In: *Phys. Rev. Lett.* 113 (26 Dec. 2014), p. 267601. DOI: 10.1103/PhysRevLett.113.267601.

[199] Takashi Nakajima et al. "Coherence of a Driven Electron Spin Qubit Actively Decoupled from Quasistatic Noise". In: *Phys. Rev. X* 10 (1 Mar. 2020), p. 011060. DOI: 10.1103/PhysRevX.10.011060.

[200] Norman F. Ramsey. "A Molecular Beam Resonance Method with Separated Oscillating Fields". In: *Phys. Rev.* 78 (6 June 1950), pp. 695–699. DOI: 10.1103/PhysRev.78.695.

[201] E. L. Hahn. "Spin Echoes". In: *Phys. Rev.* 80 (4 Nov. 1950), pp. 580–594. DOI: 10.1103/PhysRev.80.580.

[202] Trevor McCourt et al. "Learning noise via dynamical decoupling of entangled qubits". In: *Physical Review A* 107.5 (May 2023), p. 052610. DOI: 10.1103/PhysRevA.107.052610.

[203] Juha T. Muhonen et al. "Storing quantum information for 30 seconds in a nanoelectronic device". In: *Nature Nanotechnology* 9.12 (Dec. 2014), pp. 986–991. ISSN: 1748-3387, 1748-3395. DOI: 10.1038/nnano.2014.211.

[204] E. Knill et al. “Randomized benchmarking of quantum gates”. In: *Phys. Rev. A* 77 (1 Jan. 2008), p. 012307. DOI: 10.1103/PhysRevA.77.012307.

[205] Joseph Emerson, Robert Alicki, and Karol Życzkowski. “Scalable noise estimation with random unitary operators”. In: *Journal of Optics B: Quantum and Semiclassical Optics* 7.10 (Sept. 2005), S347. DOI: 10.1088/1464-4266/7/10/021.

[206] Easwar Magesan, Jay M. Gambetta, and Joseph Emerson. “Characterizing quantum gates via randomized benchmarking”. In: *Phys. Rev. A* 85 (4 Apr. 2012), p. 042311. DOI: 10.1103/PhysRevA.85.042311.

[207] J. Helsen et al. “General Framework for Randomized Benchmarking”. In: *PRX Quantum* 3 (2 June 2022), p. 020357. DOI: 10.1103/PRXQuantum.3.020357.

[208] Daniel Gottesman. “Theory of fault-tolerant quantum computation”. In: *Phys. Rev. A* 57 (1 Jan. 1998), pp. 127–137. DOI: 10.1103/PhysRevA.57.127.

[209] Earl T. Campbell, Barbara M. Terhal, and Christophe Vuillot. “Roads towards fault-tolerant universal quantum computation”. In: *Nature* 549.7671 (Sept. 2017), pp. 172–179. DOI: 10.1038/nature23460.

[210] Jeffrey M. Epstein et al. “Investigating the limits of randomized benchmarking protocols”. In: *Physical Review A* 89.6 (June 2014), p. 062321. DOI: 10.1103/PhysRevA.89.062321.

[211] Maximilian Rimbach-Russ et al. “Simple framework for systematic high-fidelity gate operations”. In: *Quantum Science and Technology* 8.4 (Sept. 2023), p. 045025. DOI: 10.1088/2058-9565/acf786.

[212] X. Xue et al. “Benchmarking Gate Fidelities in a Si/SiGe Two-Qubit Device”. In: *Phys. Rev. X* 9 (2 Apr. 2019), p. 021011. DOI: 10.1103/PhysRevX.9.021011.

[213] Ning Wang et al. *Pursuing high-fidelity control of spin qubits in natural Si/SiGe quantum dot*. 2024. arXiv: 2409.09747.

[214] R. J. Schoelkopf et al. “The Radio-Frequency Single-Electron Transistor (RF-SET): A Fast and Ultrasensitive Electrometer”. In: *Science* 280.5367 (1998), pp. 1238–1242. DOI: 10.1126/science.280.5367.1238.

[215] Wei Lu et al. “Real-time detection of electron tunnelling in a quantum dot”. In: *Nature* 423.6938 (May 2003), pp. 422–425. ISSN: 1476-4687. DOI: 10.1038/nature01642.

[216] T. Fujisawa et al. “Electron counting of single-electron tunneling current”. In: *Applied Physics Letters* 84.13 (Mar. 2004), pp. 2343–2345. DOI: 10.1063/1.1691491.

[217] Emmanuel Chanrion et al. “Charge Detection in an Array of CMOS Quantum Dots”. In: *Phys. Rev. Appl.* 14 (2 Aug. 2020), p. 024066. DOI: 10.1103/PhysRevApplied.14.024066.

[218] Elliot J. Connors, JJ Nelson, and John M. Nichol. “Rapid High-Fidelity Spin-State Readout in Si/Si-Ge Quantum Dots via rf Reflectometry”. In: *Phys. Rev. Appl.* 13 (2 Feb. 2020), p. 024019. DOI: 10.1103/PhysRevApplied.13.024019.

List of publications

1. **Thomas Koch**, Clement Godfrin, Viktor Adam, Julian Ferrero, Daniel Schroller, Noah Glaeser, Stefan Kubicek, Ruoyu Li, Roger Loo, Shana Massar, George Simion, Danny Wan, Kristiaan De Greve and Wolfgang Wernsdorfer. *Industrial 300 mm wafer processed spin qubits in natural silicon/silicon-germanium.* arXiv preprint, Sept. 2024, arXiv:2409.12731.

2. Julian Ferrero, **Thomas Koch**, Sonja Vogel, Daniel Schroller, Viktor Adam, Ran Xue, Inga Seidler, Lars R. Schreiber, Hendrik Bluhm and Wolfgang Wernsdorfer. *Noise reduction by bias cooling in gated* Si/Si_xGe_{1-x} *quantum dots.* Appl. Phys. Lett. 13 May 2024; 124 (20): 204002. `https://doi.org/10.1063/5.0206632`

Acknowledgments

The journey of completing this PhD thesis has been a profound and transformative experience, one that I could not have accomplished alone. I am deeply grateful to all those who supported, encouraged, and guided me throughout these years, making this work possible.

First and foremost, I wish to express my sincerest gratitude to my Doktorvater, Wolfgang Wernsdorfer. I have never met such an impressive character in my life. Your intuition for physics is unmatched, and combined with your resilience and enthusiasm for everything you do (except vacation), your success was a natural outcome, regardless of the field you pursued. As our mentor, you created an environment that allowed us to explore our ideas freely, while providing us with an absolutely luxurious amount of cryogenic equipment and expertise. I feel blessed to have had the opportunity to learn from you, and thank you again for always taking the time out of your busy schedule to lend us your ear.

I am deeply grateful to my second advisor, Kristiaan De Greve. Without you, this close and fruitful collaboration would not have been possible. Thank you also for your constant kindness, attention to detail, humour and interest in my work. It has been a great pleasure!

Then of course I have to thank the Dream Team with whom I had the pleasure to form the core of the semiconductor qubit subgroup: Julian, Daniel, and Viktor. Together, we were four very different and unique personalities who developed a wonderful synergy. Julian with his head-on approach, organised by Daniel's calm and down to earth fascination for the tiniest details, while Viktor pulled another one of his multiverse of punchlines out of his sleeve. It was an amazing ride, I love you guys.

Clement, who became part of our family after his first visit, which escalated into a hardcore measurement marathon week. Thank you for all your help, guidance, ideas and endless positivity.

Sonja, like Julian always said, you were our sunshine in the office. Your positivity and enthusiasm was contagious. Also, it always brings a smile on my face when watering Schwester. Thank you!

I would also like to thank all our students, Sven, Ara, Noah, Niklas, Daniel, Moritz, who shared and supported us on our journey. I hope you enjoyed it as much as I did, even if you had to put up with some far too long group meetings.

Kiril, who introduced me to the addictive pleasure of seeing all the hours of work you put into solving a problem finally pay off. I was so lucky to have you as my Master's thesis supervisor. Thank you for your patience and always good mood (maybe the bonding machine will tell a different story), you always had the right joke at the right time. I wish you all the best for your future and look forward to seeing you again, wherever that may be.

Further, I would like to thank all my fantastic colleagues and ex-colleagues, Luca, Ioannis, Luis, Svenja, Alex, Dennis, Simon, Markus, Janick, Christoph, Tino, Tim, Aljoscha, Sophie, Michi, Richard, Stichi, Safa, Sagar, Appu, Tajamul, Marcel, Peter, and all the others I forgot to mention by name, thank you for creating so many wonderful memories with me, be it at one of the many barbecues or parties, or some brainstorming, or just some meaningless chitchat during one of the too many coffee breaks. You have been my second family. It has been a wonderful adventure and I hope to see as many of you as possible at some point.

And of course I would like to thank my other family, especially my dad. I am sorry for all the problems I caused after Mom died and I am grateful for your endless support over all these years. At some point you just trusted me with my decisions, which was a great feeling. It makes me very happy to see how active and energetic you still are and I hope you will be for many more years to come. And, of course, thanks to my brother, who pushed me to study physics in the first place. Without you I would not have even started this journey.

And last, but certainly not least, thank you, Anne. You are my best friend. You supported me through every low and celebrated each high with me. Words cannot fully express how grateful I am to have you by my side. Without you, I would never have found the strength for this journey, and I look forward to sharing many more moments with you, no matter where in the world.